



# Hybrid Quantum Systems With Nitrogen Vacancy Centers and Mechanical Resonators

## Citation

Kabcenell, Aaron Noah. 2020. Hybrid Quantum Systems With Nitrogen Vacancy Centers and Mechanical Resonators. Doctoral dissertation, Harvard University, Graduate School of Arts & Sciences.

## Permanent link

<https://nrs.harvard.edu/URN-3:HUL.INSTREPOS:37365840>

## Terms of Use

This article was downloaded from Harvard University's DASH repository, and is made available under the terms and conditions applicable to Other Posted Material, as set forth at <http://nrs.harvard.edu/urn-3:HUL.InstRepos:dash.current.terms-of-use#LAA>

## Share Your Story

The Harvard community has made this article openly available.  
Please share how this access benefits you. [Submit a story](#).

[Accessibility](#)

©2020 – AARON NOAH KABCENELL  
ALL RIGHTS RESERVED.

# Hybrid Quantum Systems with Nitrogen Vacancy Centers and Mechanical Resonators

## ABSTRACT

Hybrid quantum systems involving coupled mechanical and spin degrees of freedom are promising candidates for applications in quantum metrology and quantum information processing. Specific examples range from sensitive magnetic field measurements to preparation of non-classical states of macroscopic objects and quantum transducers for mediating long range interactions between quantum bits. Nitrogen-vacancy (NV) centers in diamond represent a particularly promising spin system for these application. They feature long coherence times, well developed control methods, and a possibility of magnetic coupling to mechanical systems. However, achieving strong coupling between spin and mechanical degrees of freedom is challenging, as it requires a combination of large resonator zero point motion, magnetic field gradient, and mechanical quality factor within the same setting.

This thesis presents two approaches for magnetic coupling between individual NV centers and mechanical oscillators. In the first approach, we demonstrate progress towards a high-cooperativity system with magnetically functionalized, doubly clamped silicon nitride resonators. We engineer high quality factor ( $Q > 10^5$ ) resonators with large magnetic field gradients, and show how NVs can be integrated with this platform. Prospects for ground state cooling and quantum gate operations mediated by a mechanical bus are discussed.

In the second approach, single micromagnets are trapped using a type-II superconductor nearby to spin qubits, enabling direct magnetic coupling between the two systems. Controlling the distance between the magnet and the superconductor during cooldown, we demonstrate three-dimensional trapping with quality factors above  $1 \times 10^6$  and kHz trapping frequencies. The large magnetic moment to mass ratio of this mechanical oscillator is further exploited to couple its motion to the spin degrees of freedom of an individual NV center, and the resulting coupling is measured. This represents a new platform for ultrasensitive metrology, testing quantum mechanics with mesoscopic objects, and realizing quantum networks.

# Contents

<b>1</b>	<b>INTRODUCTION</b>	<b>1</b>
1.1	Background . . . . .	1
1.2	Overview of the Thesis . . . . .	5
1.3	Chapter 2: Theory of Nitrogen Vacancy Center-Mechanics Hybrid Systems	5
1.4	Chapter 3: Magnetically Functionalized Resonators for Strong NV-Mechanics Interactions . . . . .	6
1.5	Chapter 4: Single-Spin Magnetomechanics with Levitated Micromagnets	6
<b>2</b>	<b>THEORY OF NITROGEN VACANCY CENTER - MECHANICS HYBRID SYSTEMS</b>	<b>8</b>
2.1	Nitrogen Vacancy Centers in Diamond . . . . .	8
2.2	Magnetometry with NV Centers . . . . .	10
2.3	NV-Mechanics Hybrid Systems . . . . .	13
<b>3</b>	<b>MAGNETICALLY FUNCTIONALIZED RESONATORS FOR STRONG NV-MECHANICS INTERACTIONS</b>	<b>16</b>
3.1	Introduction . . . . .	16
3.2	Fabrication and Characterization of Resonators with Cobalt Stencil Magnets . . . . .	17
3.3	Improving Magnetic Response: Magnetic Particles . . . . .	23
3.4	Fabrication and Characterization of Resonators with Iron Magnets . . . . .	25
3.5	Outlook . . . . .	30
<b>4</b>	<b>SINGLE-SPIN MAGNETOMECHANICS WITH LEVITATED MICROMAGNETS</b>	<b>35</b>
4.1	Introduction . . . . .	35
4.2	Theory of Magnetic Levitation . . . . .	37
4.3	Experimental Levitation of Micromagnets . . . . .	45
<b>5</b>	<b>CONCLUSION AND OUTLOOK</b>	<b>63</b>
5.1	Magnetically Functionalized Resonators for Strong NV-Mechanics Interactions . . . . .	64

5.2	Single-Spin Magnetomechanics with Levitated Micromagnets . . . . .	65
<b>APPENDIX A FABRICATION PROCEDURES</b>		<b>66</b>
A.1	Doubly Clamped Resonator Device Fabrication . . . . .	67
A.2	Magnetic Levitation Device Fabrication . . . . .	75
<b>APPENDIX B ADDITIONAL DETAILS OF LEVITATION EXPERIMENT</b>		<b>80</b>
B.1	Experimental Details . . . . .	80
B.2	Material Properties . . . . .	86
<b>APPENDIX C PYLABCONTROL: A PLATFORM FOR SCIENTIFIC EXPERIMENT CONTROL</b>		<b>89</b>
C.1	Introduction . . . . .	89
C.2	Modern Quantum Optics Laboratory Control Software . . . . .	91
C.3	pylabcontrol Core . . . . .	92
C.4	Toolkits . . . . .	100
C.5	Future Work . . . . .	101
<b>REFERENCES</b>		<b>113</b>

DEDICATED TO MY FIANCÉE SAM  
AND MY PARENTS BRIAN, ALISA, JOANNE, AND KEN

# Acknowledgments

There are a number of people without whom the work in this thesis would not be possible. I would first like to acknowledge my advisor Misha. His incredible intuition and new ideas always kept the experiments pushing forward, and his teaching and mentorship were critical to learning how to solve challenging research problems. I would also like to thank my committee members Marco Lončar and Philip Kim. Marco's experience with NVs, mechanics, and hybrid systems has been invaluable to the project. Philip's fabrication insights have been critical, and thanks as well for sharing his superconducting magnet which was necessary to the project's completion. In addition, Professor Jack Harris has been an amazing source of mechanics knowledge for the projects. I would also like to thank Professor Oriol Romero-Isart for his many discussions and his theory contributions on our levitation work.

This work was done in collaboration with a number of excellent students and post-docs. I would first like to thank the B26 experimental team of Jan Gieseler, Arthur Safira, Emma Rosenfeld, DaLi Schaefer, Frankie Fung, Maya Miklos, and Léa Bresque. Arthur was instrumental in teaching me everything I know about NV centers, and

spent many long hours in the cleanroom imparting his wisdom on nanofabrication. Jan deserves much credit for bringing his wealth of technical skills and excellent ideas to the projects, and for his mentorship and teaching over the years. Emma has been an excellent partner for the last three years, and her hard work and many insights were critical to the projects' success. DaLi and Frankie have hit the ground running, providing significant contributions and taking ownership of the experiments, and I'm incredibly excited to see what they can accomplish during the rest of their PhDs. I also want to thank our theory collaborators Martin Schuetz, Cosimo Rusconi, and Carlos Gonzalez-Ballesterro.

I benefited tremendously from the knowledge and skills of the Lukin group, as well as the wonderful community they provided over the last six years. Discussions with them over the years helped us overcome numerous technical and physics challenges. I would in particular like to thank the other researchers working on diamond defects for their insights over the years: Elana Urbach, Tamara Sumaric, Bo Dwyer, David Levonian, Kristiaan de Greve, Javier Sanchez-Yamagishi, Andrey Sushko, Trond Andersen, Nabeel Aslam, Christian Nguyen, Alexei Bylinskii, Michael Goldman, Igor Lovchinsky, Alp Sipahigil, Ruffin Evans, Denis Sukachev, Ralf Riedinger, Nathalie de Leon, Kristine Rezai, Joonhee Choi, Harry Zhou, Mihir Bhaskar, Daniel Kim, Erik Knall, and Can Knaut.

I would additionally like to thank Bart Machielse for sharing his fabrication expertise (and his resist) over the years. Srujan Meesala, Young-Ik Sohn, and Jeffrey Holzgrafe have been invaluable for this project by providing us early test samples and providing their experience with nanomechanical system fabrication and characterization. I also want to thank Frank Zhao for teaching us how to use a cryogenically cooled magnet to magnetize our samples, and his endless patience helping us to fix

every possible nitrogen and helium flow issue as it happened.

I further want to thank all of the staff who make these experiments possible. Many of these experiments were carried out at the Harvard Center for Nanoscale Systems (CNS), and I want to thank JD Deng, Yuan Lu, Steve Paolini, Philippe de Rouffignac, Jason Tresback, David Lafleur, Tim Cavanaugh, and the rest of the staff for their help carrying out experiments, fixing issues, and keeping all of the equipment going with very impressive uptimes. Electronics guru Jim MacArthur has taught me a lot over the years, and has always had a joke at the ready. I am also grateful to all of the department staff, including Sam, Clare, Karl, Adam, Lisa, and Jacob, for their help and advice.

I was incredibly fortunate to also be able to conduct computer science research in parallel to the work presented in this thesis with the Harvard Data Systems Lab, which let me explore another one of my passions. I want to thank Stratos Idreos for believing in me and allowing me to dive into this work. I also want to thank Niv Dayan for sharing his wisdom on LSM trees and how to approach these fascinating problems, the Cosine team of Subarna Chatterjee, Wilson Qin, and Meena Jagadeesan, and the rest of the lab.

I would like to thank my friends for their support over the years: Amogha, Ian, Alex, Drew, Ben, Shelby, Mireille, Regina, Valya, Ross, Emily, Carolyn, Olivia, Lauren, Jessica, and Emily. I additionally want to thank my tabletop group of Christian, Kimee, Dan, Tim, Evelyn, Chris, Elana, Melissa, and Alex for providing many evenings of fun and an excellent respite from research.

Finally, I am extremely grateful to my family for all of their support during my PhD. Thanks especially to my fiancée Sam, who made many trips from New York, was there for me when I came home at 4am from the cleanroom after my sample ex-

ploded, and has provided endless happiness over the past six years.

I want to acknowledge the Department of Defense (DOD) for their funding through the National Defense Science and Engineering Graduate Fellowship (NDSEG) Program and Harvard for their funding through the William E. Keller Graduate Student Research Fellowship. This work was supported by the NSF, the Center for Ultracold Atoms (CUA), the ONR MURI Quantum OptoMechanics with Atoms and Nanostructured Diamond (QOMAND), the Vannever Bush Faculty Fellowship, and the Moore Foundation. This work was performed in part at the Center for Nanoscale Systems (CNS), a member of the National Nanotechnology Coordinated Infrastructure Network (NNCI), which is supported by the National Science Foundation under NSF Grant No. 1541959. CNS is part of Harvard University. Collaborators were supported by the European Union (SEQOO, H2020-MSCA-IF-2014, No. 655369 and (PWAQUTEC, H2020-MSCA-IF-2017 No. 796725) and the National Science Foundation Graduate Research Fellowship Program under Grants No. DGE1144152 and No. DGE1745303, . Any opinions, findings, and conclusions or recommendations expressed in this material are those of the author(s) and do not necessarily reflect the views of the National Science Foundation.

# Citations to previously published work

Nearly the entirety of chapter 4 and appendix B have been published as:

J Gieseler, A Kabcenell, E Rosenfeld, J D Schaefer, A Safira, M J A Schuetz, C Gonzalez-Ballester, C C Rusconi, O Romero-Isart, and M D Lukin. Single-Spin Magnetomechanics with Levitated Micromagnets. *Physical Review Letters*, 124(16):163604, April 2020. ©2020 American Physical Society

# 1

## Introduction

### 1.1 BACKGROUND

The past few decades have seen remarkable growth in quantum technologies, which use quantum mechanics to enable devices that would be impossible based on classical physics. These technologies have the potential to revolutionize fields such as sensing, communications, and computing. However, significant technical challenges remain to

be tackled, and practical devices will likely combine multiple systems together to best leverage the advantages of each<sup>1</sup>.

Recently, interest has grown in spin-mechanics hybrid systems<sup>2</sup>, which combine a spin quantum bit with a macroscopic mechanical resonator. Spins are inherently quantum systems that can have extremely well developed control and readout. Mechanical resonators can couple to spin systems, be scaled up easily using modern fabrication techniques, and be engineered to have extremely high quality factors, making them good candidates for storage and coherent transfer of quantum states. Systems combining these properties have exciting applications in metrology and quantum information, where they could open the door to exploring new parameter regimes and provide the foundation for new technologies. In particular, this thesis will focus on hybrid systems using nitrogen-vacancy (NV) centers in diamond as the spin component. We will first discuss these two exciting avenues for research, then give an overview of the subsequent chapters of the thesis.

### 1.1.1 METROLOGY

Mechanical oscillators have grown as a key technology for ultrasensitive measurements. The atomic force microscope<sup>3</sup>, invented in 1986, utilizes cantilevers to take detailed topographical measurements and has become a standard scientific tool. Mechanical resonators are similarly the key technology in spin<sup>4</sup>, mass<sup>5,6</sup>, and magnetic field<sup>7,8</sup> measurements. These applications require state of the art high quality factor, low mass resonators, which continue to be developed and improved.

Recently, levitated ferromagnetic particles have emerged as a promising new technology for sensing. Proposals have shown the potential for these systems to be used as extremely sensitive force and inertial sensors, with both commercial applications

to gravimetry and avionics, and research applications such as studies of magnetic Casimir forces<sup>9</sup>. There is also the potential to use a levitated, precessing ferromagnetic needle to measure magnetic fields for long times<sup>10</sup>. This could have a sensitivity many orders of magnitude better than existing systems for precise tests of fundamental physics. There have been early steps towards realizing this potential<sup>11,12</sup>, but significant technological development remains to be done.

All of these applications require extremely accurate readout of the mechanical system. One approach is to use a coupled spin system. NV centers can be used as high-sensitivity magnetometers, taking advantage of magnetic field dependent phase accumulation with well established AC magnetometry techniques. They have already been demonstrated to be excellent displacement sensors for nano-mechanical resonators, detecting Brownian motion of a magnetic force microscopy magnetically functionalized cantilever with 5 pm resolution<sup>13</sup>. Such a system could also be used for sensitive spin detection using the mechanical motion<sup>4</sup>. The key outstanding challenge is engineering strong coupling between the oscillator and spin systems.

Additionally, by coupling a mechanical oscillator to a spin system, a non-linearity is introduced to the oscillator. This permits cooling of the resonator and can allow the otherwise classical object to be put into a quantum state<sup>14,15</sup>. Such a system opens the door to studying the limits of quantum mechanics with macroscopic objects<sup>16,17</sup>.

### 1.1.2 QUANTUM INFORMATION

Quantum computers, in which computations are performed using quantum bits (qubits), can drastically outperform classical computers for certain key problems. For example, Shor's algorithm<sup>18</sup> allows integers to be factored in a time scaling polynomially with the length of the integer, rather than exponentially as with the best

classical algorithm. Given that public key cryptography relies on the computational intractability of large number factorization, this could render existing encryption protocols obsolete. Grover’s algorithm<sup>19</sup> allows an unstructured database to be searched in a time that scales with the square root of the data size, rather than the linear scaling of classical algorithms, which could have significant impact as stored data volumes continue to grow. Realization of these and similar algorithms at scale is predicted to have transformative effects over the next few decades across industries as diverse as material design, pharmaceuticals, and finance, with a potential impact of over \$450 billion annually<sup>20</sup>. Recent progress towards this goal has been made with claims that a 53 qubit processor achieved quantum supremacy<sup>21</sup>, or the ability to perform a calculation that would be impossible with classical computers. However, significant technical challenges must still be overcome before commercially applicable results, and eventually universal quantum computation, can be achieved.

NV centers have shown significant promise as qubits for these applications due to their long lifetimes and well developed single bit control. However, engineering scalable two qubit interactions remains an outstanding challenge. Entanglement via direct spin-spin interactions between NVs has been demonstrated<sup>22</sup>, which takes advantage of the natural interactions. However, due to the  $d^{-3}$  distance scaling of the dipolar interactions, this can only couple adjacent NVs with tens of nanometer separations and will be challenging to scale. Long range entanglement of NVs over more than a kilometer was demonstrated using photon heralded methods<sup>23,24</sup>. These methods have continued to improve with results such as entanglement distillation for these systems<sup>25</sup>, but are inherently probabilistic and it will be challenging to achieve the high entanglement rates necessary for entangling many qubits.

Mechanical systems offer an exciting path forward for mediating interactions, func-

tioning as a quantum bus to allow coherent spin-spin interactions between defects separated by tens of microns. This has been proposed for NV centers, with each defect coupled to a magnetically functionalized cantilever, which are themselves charged and capacitively coupled<sup>26</sup>. Others posit similar architectures, such as coupling the spins to a magnonic crystal or levitated magnetic particles coupled via superconducting loops<sup>27</sup>. These systems offer potential opportunities to create a scalable, many-qubit system, but successful implementation of a high quality resonator that can be strongly magnetically coupled to an NV center remains an outstanding challenge.

## 1.2 OVERVIEW OF THE THESIS

The remainder of the thesis consists of four chapters. Chapter 2 gives the necessary background on NV centers and spin-mechanics hybrid systems. Chapters 3 and 4 detail progress on and experiments with two hybrid systems with different mechanical systems. Finally, chapter 5 summarizes these results and discusses future prospects.

## 1.3 CHAPTER 2: THEORY OF NITROGEN VACANCY CENTER-MECHANICS HYBRID SYSTEMS

In this chapter, there is an introduction to the basic properties of NV centers and discussion of the associated experimental techniques that will be relevant for the rest of the thesis. There is also an introduction to the physics of NV centers coupled to mechanical modes via a magnetic field, with both intuitive and quantitative treatments as well as a discussion of which figures of merit are critical to optimize in such a system.

## 1.4 CHAPTER 3: MAGNETICALLY FUNCTIONALIZED RESONATORS FOR STRONG NV-MECHANICS INTERACTIONS

In this chapter, we demonstrate progress towards a high-cooperativity system with an NV center coupled to a doubly clamped, magnetically functionalized silicon nitride resonator. We discuss three different methods for fabrication of these systems: evaporation of cobalt magnets through silicon nitride stencils, manual placement of magnetic microparticles, and liftoff of iron magnets with a  $\text{XeF}_2$  gas mechanics release. For each of these methods, we characterize the resulting mechanical properties using an interferometer, and the resulting magnetic properties using magnetic force microscopy and NV metrology. We demonstrate that the last of these methods is the most promising for realizing strong NV-mechanics interactions. We discuss integration of NVs with these resonators, and how to measure the resulting coupling. We further consider technical improvements to continue to push the figures of merit for the devices into the high cooperativity regime, and viability of near-term application such as cooling the resonator to near the ground state and longer term applications such as quantum information experiments.

## 1.5 CHAPTER 4: SINGLE-SPIN MAGNETOMECHANICS WITH LEVITATED MICRO-MAGNETS

In this chapter, we demonstrate a new platform for strong spin-mechanics coupling using magnetically levitated microscopic magnets coupled to NV centers. We discuss the theoretical underpinnings of the levitation of magnetic particles above a superconductor. We then lay out our scheme, which has achieved low dissipation levitation

of Nd-Pr-Fe-Co-Ti-Zr-B microscopic particles above a yttrium barium copper oxide (YBCO) thin film, and characterize the resulting motional modes. We show that the frequencies are tunable by varying the magnet-superconductor separation as the superconductor is cooled past its transition temperature, by scaling the particle size, and by applying external magnetic fields. We then integrate a diamond and demonstrate coupling between the magnetic oscillator and the spin by measuring the motion of the particle via the NV. We finally discuss how, with future improvements, this platform could be used to achieve a cooperativity greater than 1, or even achieve the strong coupling regime, and realize quantum effects. The resulting system could allow exciting applications such as high sensitivity magnetometers, preparation of non-Gaussian quantum states, and mechanically mediated quantum networks.

# 2

## Theory of Nitrogen Vacancy Center - Mechanics Hybrid Systems

### 2.1 NITROGEN VACANCY CENTERS IN DIAMOND

Nitrogen vacancy (NV) centers are substitutional defects in diamond that are created when two adjacent carbon atoms are removed, one is replaced with a nitrogen

atom, and the other location is left vacant. In this work we consider only the  $\text{NV}^-$  charge state. The level structure is shown in figure 2.1<sup>28</sup>.

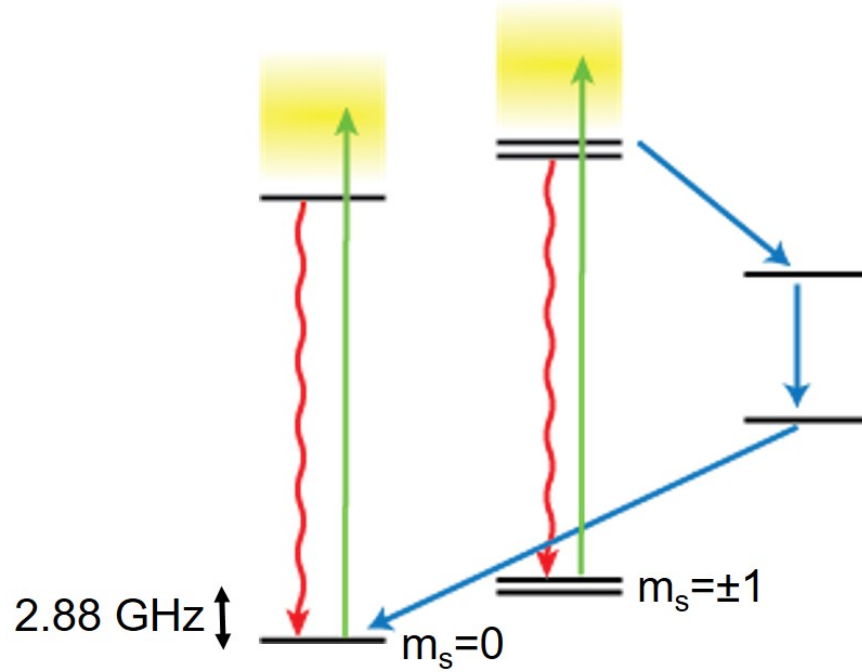


Figure 2.1: Simplified level structure of the NV center. Illumination with 532nm light can be used to both initialize into the  $m_s = 0$  state via the intersystem crossing and to perform readout due to state-dependent fluorescence.

There are multiple properties of NV centers that make them extremely promising for metrology and quantum information applications. The ground state is an electronic spin triplet with a zero field splitting of 2.88 GHz between the  $|m_s = 0\rangle$  and  $|m_s = \pm 1\rangle$  levels that possesses extremely long coherence times (up to one second<sup>29</sup>). External magnetic fields can break the  $|\pm 1\rangle$  degeneracy with a Zeeman shift of  $2\pi \times 2.8 \text{ MHz/Gauss}$ . This allows the  $|0\rangle$  and  $|-1\rangle$  states to be used as a qubit by addressing only this transition. The system can be initialized to the  $|0\rangle$  state by shin-

ing 532nm light on the defect. This occurs because an intersystem crossing causes some population from  $|\pm 1\rangle$  state to go to the metastable shelving singlet, which then non-radiatively decays down to the  $|0\rangle$  state. The same mechanism leads to spin-state dependent fluorescence, so that the NV state can be read out by using the same illumination and detecting the resulting fluorescence rate. The spin state of a single NV can be addressed by applying microwaves using a coplanar waveguide (CPW) fabricated on chip.

## 2.2 MAGNETOMETRY WITH NV CENTERS

### 2.2.1 ELECTRON SPIN RESONANCE

As noted above, magnetic fields at the location of the NV lead to shifts in the  $|\pm 1\rangle$  levels. This allows the NV to be as a magnetometer to measure the local magnetic field environment. The simplest such experiment, which allows the measurement of DC magnetic fields, is electron spin resonance (ESR). In this experiment, a microwave tone is swept across the  $|0\rangle$  to  $|\pm 1\rangle$  transitions, while the NV is continuously interrogated with a 532nm laser. The fluorescence is then read out as a function of the microwave frequency. An example result is shown in figure 2.2. When the microwave tone is off-resonant from the NV transitions, the green laser continuously re-initializes the NV to  $|0\rangle$ , so the continuous readout measures a high fluorescence rate. When the tone becomes on-resonant with one of the transitions, it transfers some of the population out of the  $|0\rangle$  state. This decreases the fluorescence rate, leading to the two dips observed, one for each of the  $|0\rangle \rightarrow |-1\rangle$  and  $|0\rangle \rightarrow |+1\rangle$  transitions. This technique allows the NV spectrum, and thus the magnetic field, to be directly determined.

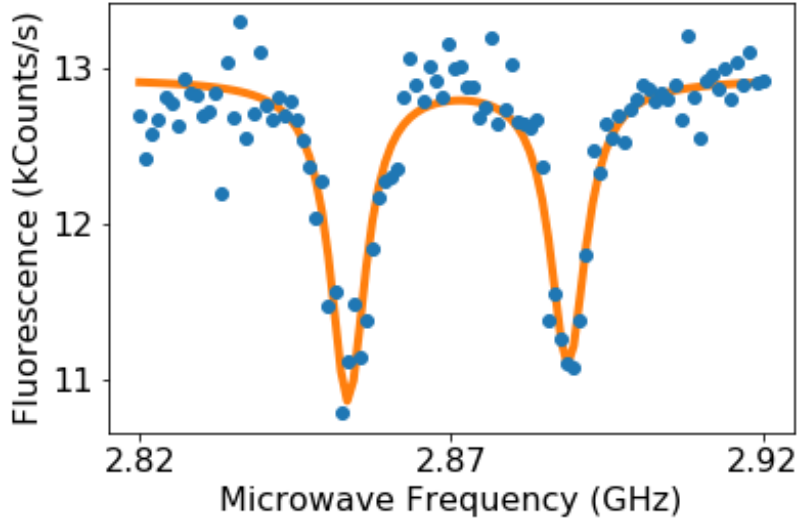


Figure 2.2: Example ESR spectrum. The two dips correspond to the  $|0\rangle \leftrightarrow |-1\rangle$  and  $|0\rangle \leftrightarrow |1\rangle$  transitions. These two dips in the data (blue) are fit to a doubly-peaked Lorentzian (orange).

### 2.2.2 AC MAGNETOMETRY

While ESR can be used for DC magnetic field measurements, we can use a series of pulsed experiments to measure high frequency signals. We first need a way to effectively manipulate the state of the NV. By performing ESR, we can identify the transition frequencies for the defect. We can then initialize the NV and drive on resonance, leading to Rabi oscillations between the two states. By applying a drive for a half period of the oscillation, we can perform a pi pulse, while a quarter period corresponds to a pi-half pulse.

These pulses can be used as the building blocks of AC sensing sequences, the simplest of which is spin echo. In this sequence, the NV is initialized to  $|0\rangle$ , then a pi-half pulse is applied. The state undergoes free precession for a time  $\tau$ , a pi pulse is ap-

plied, there is a second free precession time  $\tau$ , then a final pi-half pulse. During the first free precession time, the superposition acquires a relative phase  $\phi_1$  proportional to the local magnetic field, which is reversed to  $-\phi_1$  by the pi pulse. The second free precession time then leads to an additional phase accumulation  $\phi_2$ , so the total accumulated phase is  $\phi_{total} = \phi_2 - \phi_1$ . If there is a DC field or a field varying very slowly over  $\tau$ , then the same phase will be accumulated over each precession time,  $\phi_1 = \phi_2$ , and  $\phi_{total} = 0$ . At the other extreme, if a field undergoes many oscillations during  $\tau$ , then it will average out and have minimal impact on the accumulated phase. However, a signal with a period  $2\tau$  will switch the direction of the magnetic field, and thus the phase accumulation, at the same time as the pi pulse occurs. If there would be an accumulation  $\phi$  in the first period and  $-\phi$  in the second period, the total accumulation will be  $-2\phi \neq 0$ . The sequence is thus sensitive to AC signals at and near this period.

We can narrow the sensitive range of frequencies, or the filter function, by adding additional pi pulses with the same time separation. However, doing numerous identical pulses will cause pulse errors to compound, potentially scrambling the state. This can be prevented by carefully selecting the axes around which the pi pulses are performed, such as in CPMG or XY8-k sequences<sup>30</sup>.

### 2.2.3 USING ESR TO MEASURE LOW FREQUENCY FIELDS

In order to use the AC techniques discussed in the previous section, the period of the oscillation to be detected must be smaller than the NV lifetime. Otherwise, the pulse spacing will exceed the lifetime and the NV will decohere during the sequence. This limits the application of these techniques to sensing signals with frequencies above approximately 10 kHz. But what if we want to detect slower signals? We can

instead modify a standard ESR experiment. Consider the effect of a slow oscillation on the ESR signal. As the field changes, the transition frequency changes, so the dip will oscillate. This oscillation can be detected by setting the frequency of the microwave tone to the point of highest slope on that dip and measuring continuously. The resulting photoluminescence signal will oscillate with the magnetic field, and it can be Fourier transformed to determine the exact frequency and magnitude of the signal. Further details of this technique are discussed in 4.3.1.

### 2.3 NV-MECHANICS HYBRID SYSTEMS

Consider a system with an NV center coupled to a mechanical mode via a magnetic field. The Hamiltonian is given by:

$$H = \hbar\omega_s S_z + \hbar\omega_r \left(a^\dagger a + \frac{1}{2}\right) + \hbar\lambda(a + a^\dagger)S_z \quad (2.1)$$

where

$$\lambda = \mu_B g_s G_m a_0 / \hbar \quad (2.2)$$

In this Hamiltonian, the first term corresponds to the spin, the second term to the resonator mode, and the third term to the coupling between the two. The coupling strength  $\lambda$  depends on two terms:

1. The magnetic field gradient  $G_m = \frac{\delta B}{\delta z}$ . This is the change in magnetic field at the spin site due to the movement of the resonator.
2. The zero point motion  $a_0 = \sqrt{\hbar/2m\omega_r}$ . This depends on the resonator mass  $m$  and frequency  $\omega_r$ .

Furthermore, in order to use the system for quantum applications, we want to maximize the cooperativity:

$$C = \frac{\lambda^2}{\Gamma_m \gamma_s} \quad (2.3)$$

which is the ratio of the coupling squared to the product of the decoherence rates of the resonator (of quality factor  $Q$ )  $\Gamma_m = \frac{k_B T}{\hbar Q}$  and the spin  $\gamma_s$ . In general, we want to achieve  $C > 1$ , where the information transfer occurs faster than the decoherence. However, some applications will require higher cooperativity, and exciting results can be achieved with lower cooperativity using methods such as postselection.

### 2.3.1 DISCUSSION: CHOOSING A SPIN-MECHANICS SYSTEM

We can use this to inform our choice of systems for spin-mechanics hybrids. For the spin system, we want to maximize the spin lifetime. The long lifetimes of NV centers are thus highly desirable. In addition, their ease of use, magnetic sensitivity, ability to be positioned near to mechanical systems without traps or other overhead, optical accessibility, and the well developed control methods described earlier in this chapter make them well suited to this application.

When choosing mechanical systems, we want to maximize the gradient and quality factor while minimizing the mass and using lower frequencies to maximize the zero point motion. The two systems explored in this thesis, silicon nitride resonators and levitated micromagnets, fit these criteria well. Silicon nitride is a well developed platform for resonators, with established fabrication techniques. The material is light and very thin (150 nm), high stress films can be used, allowing the fabrication of MHz frequency nano-scale resonators with extremely low mass. Quality factors of  $Q > 10^5$

can be regularly achieved<sup>31</sup>, and band-structure engineering has allowed  $Q = 3 \times 10^8$  to be achieved<sup>32</sup>. The challenge then becomes magnetic functionalization of a resonator with a magnetic material to maximize the magnetic field gradient while not sacrificing these desirable properties, which will be explored in chapter 3.

Magnetic levitation has the potential to outperform even silicon nitride systems. The entire resonator consists of magnetic material, so it can maximize the gradient for a given mass. In addition, the lack of any support structure yields an automatic phononic shield, eliminating clamping losses and potentially allowing a resonator quality factor that is limited only by losses within the magnetic material itself with theoretical quality factors of  $Q > 10^9$ . However, magnetic levitation of microparticles has not been well explored, so technical challenges remain. Chapter 4 will demonstrate our first successful steps towards development of these systems.

# 3

## Magnetically Functionalized Resonators for Strong NV-Mechanics Interactions

### 3.1 INTRODUCTION

As noted in section 2.3.1, silicon nitride resonators represent a well developed platform for nanomechanical devices. They can leverage powerful fabrication techniques

to create extremely high quality factor, low mass structures. However, integrating them with spin defects in a high-coupling system remains an outstanding technical challenge. In this chapter, we demonstrate progress towards fabricating a magnetically functionalized, high quality factor silicon nitride resonator and integrating it with an NV center.

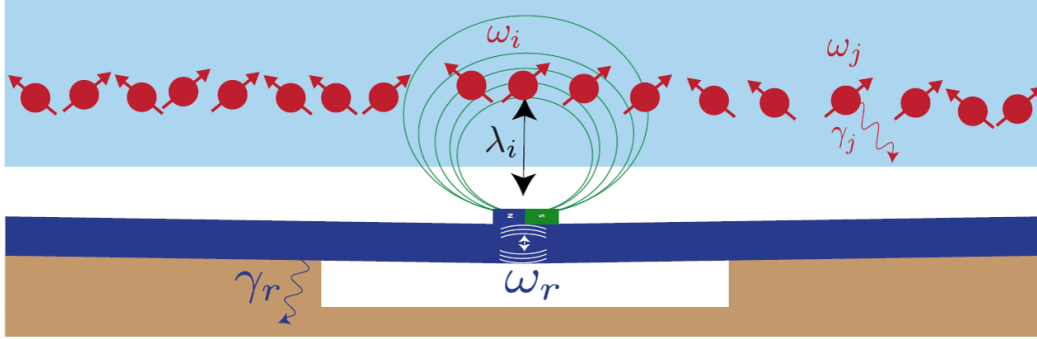


Figure 3.1: Schematic of the system. A diamond with implanted NVs is brought near to a doubly-clamped beam with a magnet in the center. Each NV  $i$  with frequency  $\omega_i$  is then coupled to the resonator mode through the magnetic field gradient with a coupling  $\lambda_i$ .

## 3.2 FABRICATION AND CHARACTERIZATION OF RESONATORS WITH COBALT STENCIL MAGNETS

In this section, we discuss first attempts at fabricating these devices.

### 3.2.1 DEVICE FABRICATION

Fabrication begins with a silicon wafer, with a 150nm layer of LPCVD, high stress SiN. Fabrication then requires four steps:

1. A gold coplanar waveguide is fabricated on top of the nitride using optical lithography and liftoff to enable microwave manipulation of the NVs
2.  $145\ \mu\text{m}$  long by  $1\ \mu\text{m}$  wide and  $145\ \mu\text{m}$  long by  $300\ \text{nm}$  wide doubly clamped resonators are fabricated in the silicon nitride using e-beam lithography and reactive ion etching. The beams are then released using a KOH anisotropic etch.
3. A low stress silicon nitride hardmask with a thin ( $2\ \mu\text{m}$ ) slit is aligned to the resonator sample, then a Ti-Co-Pt trilayer is evaporated through the mask. Most of the metal falls to the bottom of the release trench, but a small amount falls on the resonator and forms the magnet.
4. A diamond is placed on top of the sample, with the NV implanted side adjacent to the resonator. The fabricated chip is secured to a carrier using vacuum grease and wirebonded to it to allow electrical connection and easy handling.

Full details are provided in appendix A.

### 3.2.2 MECHANICS CHARACTERIZATION

In keeping with our goal of maximizing cooperativity, we want to maximize the mechanical quality factor of the resonators. We thus characterize the Q factors for resonators fabricated using the method described in the previous section. To do this, we built a Mach-Zehnder interferometer in fiber, a schematic of which is shown in figure 3.3, and integrated it with our confocal microscope system. The system uses a separate long coherence length  $1064\ \text{nm}$  laser for these experiments, as silicon nitride has an order of magnitude higher absorption of the  $532\ \text{nm}$  laser used for NV imaging. The absorption leads to heating effects, causing frequency shifts and in the worst case

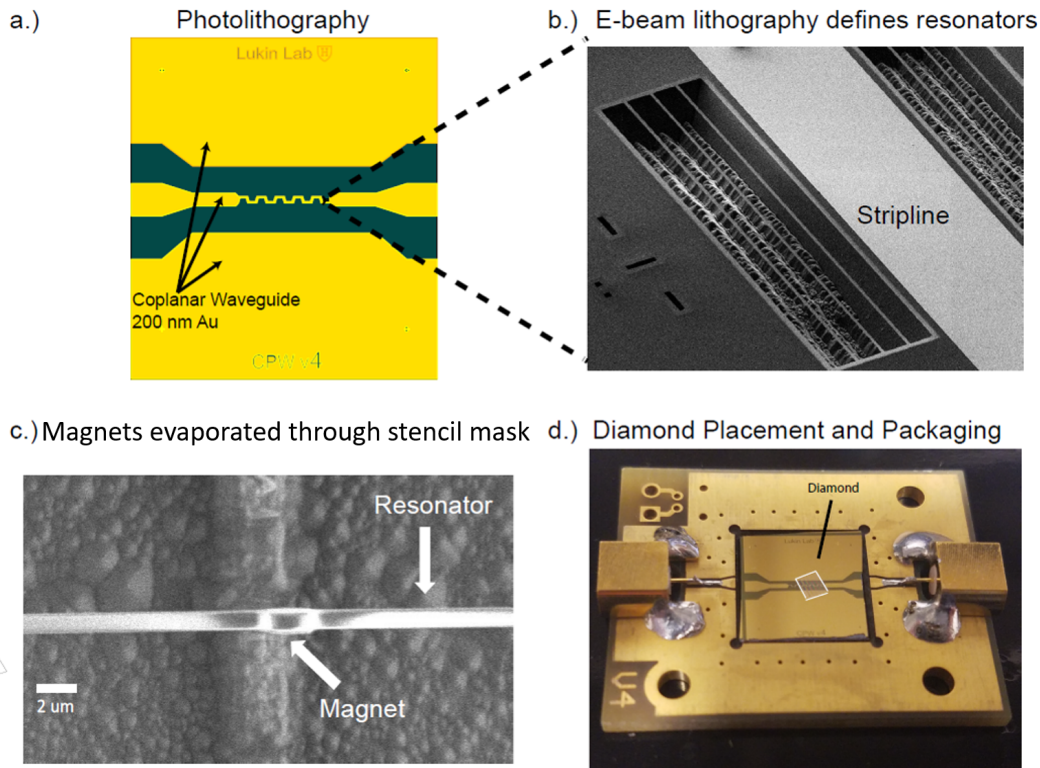


Figure 3.2: An overview of the fabrication process. a) First, starting with a silicon nitride on silicon wafer, a co-planar waveguide is fabricated. b) E-beam lithography, a reactive ion etch, and a KOH etch are used to define and release the resonators. c) A stencil hardmask is used to define the magnets on the resonators. d) A diamond is placed on top of the resonators, and the full chip is placed into a carrier to allow external electrical connections.

melting through the resonators. The beam is split into a sample and a reference arm. The beam in the sample arm is launched from fiber into the confocal setup right before the galvanometer, reflected off of the resonator, then collected back into fiber. The reference arm is phase stabilized and recombined with the sample arm, before the combined signal is split and sent to a two port detector. The resulting difference signal is sent to a lock-in amplifier (Zurich Instruments HF2) for analysis, as well as

being used to lock the interferometer against slow drifts.

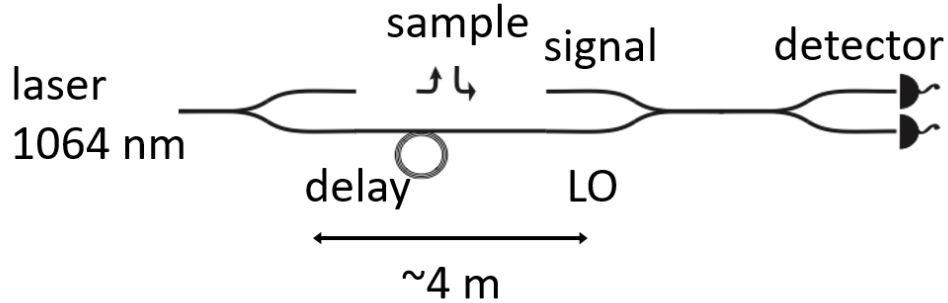


Figure 3.3: Schematic of the Mach-Zehnder interferometer setup used for mechanics characterization. A long coherence length 1064 nm laser is split into sample and reference arms. The sample arm beam is reflected off of the resonator, then recombined with the stabilized reference arm. The beam is then split again and read out on a two port detector, with the resulting difference signal sent to a lock-in amplifier.

Resonator characterization data are displayed in figure 3.4. For these experiments, the lock-in amplifier is used in 'sweep' mode, so it sequentially reads out the amplitude component at each frequency near the resonance. Figure 3.4a demonstrates the resonance for a representative resonator without a magnet at high vacuum ( $< 10^{-3}$  Torr) and cryogenic temperatures ( $< 10$  K). The resulting quality factor,  $Q = 1.25 \times 10^6$ , was competitive with leading silicon nitride resonators at the time the experiment was conducted<sup>31</sup>.

Now consider the effect of the magnet on the resonator quality factor. Figure 3.4b shows the same experiment with a representative magnetically functionalized resonator where the quality factor has decreased by less than a factor of three, to  $Q = 4.40 \times 10^5$ . Thus, though the magnet does slightly decrease  $Q$ , it remains high enough to be able to achieve high cooperativity results with reasonable other parameters.

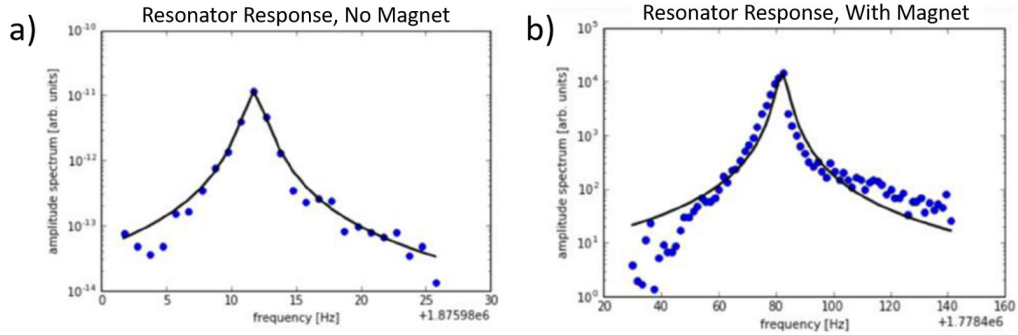


Figure 3.4: The interferometer data for KOH-released resonators. a) For an unloaded resonator, we measure a quality factor of  $Q = 1.25 \times 10^6$ . b) Even with a magnet, the quality factor remains high with  $Q = 4.40 \times 10^5$ .

### 3.2.3 MAGNETIZATION CHARACTERIZATION

Now that we have determined that the mechanical properties are good, we need to test the magnetic properties of the samples. To do this, we use NVs, as the magnetic field due to the magnet causes a level shift that we can read out in ESR experiments (see 2.2.1). Since we're interested in measuring gradients, not just static fields, one approach we can take is to move the diamond relative to the magnet during our experiments. To do this, we mount the sample on a piezo stack. We then surround the diamond by a silicon frame, and place this frame inside a fixed metal one. When we move the piezo stack and the attached sample, the diamond stays in place, allowing us to 'scan' the NVs across the magnet.

The results of one such scan are displayed in figure 3.5. From the data, we extract a gradient of 500 T/m. Note that this is an estimate of the gradient in the horizontal direction, rather than the vertical one we would use for an experiment, but it serves as an initial step. Unfortunately, this value is extremely low. From basic dipole models and more complex magnet simulations using oommf<sup>33</sup>, we expect gradients at

least in excess of  $10^5$  T/m, and potentially above  $10^6$  T/m. These results persisted even when the material was magnetized in a 1T field along the easy (geometrically longest) axis. There are two potential issues: 1) our fabricated magnets have substantially lower magnetic moments than expected, or 2) the sample does not remain clean enough during the fabrication process to keep dust or other particles off of the surface and keep the NV-magnet distance below  $2 \mu\text{m}$ .

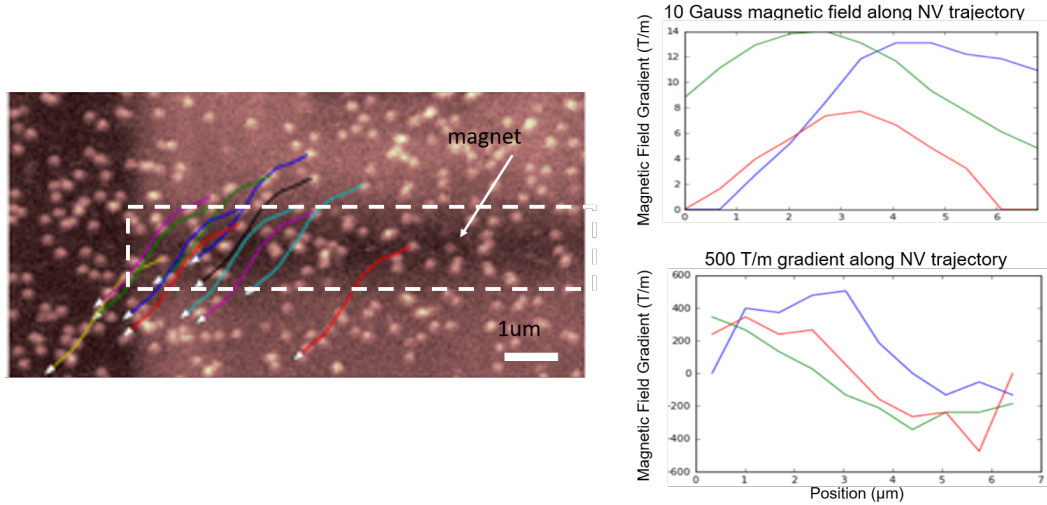


Figure 3.5: Magnetic properties of the stencil deposited magnets. At left is the path the NVs are pushed across the magnet (white dashed box), with ESRs being taken along this path. At right is the derived DC magnetic field and gradient for three of the NV paths. The maximum gradient is only 500 T/m, significantly lower than expected.

We can test the first of these hypothesis using magnetic force microscopy (Asylum Research Cypher). We deposit a magnet on a sample of silicon nitride using the same procedure, and scan across the magnet. The results are shown in figure 3.6. Though the magnets look qualitatively intact and don't suffer from obvious damage or delamination, the MFM results show that areas on the magnet have the same response as

the silicon nitride background, or equivalently that the magnets do not display a significant magnetic response. The mechanism for failure in the process remains unknown.

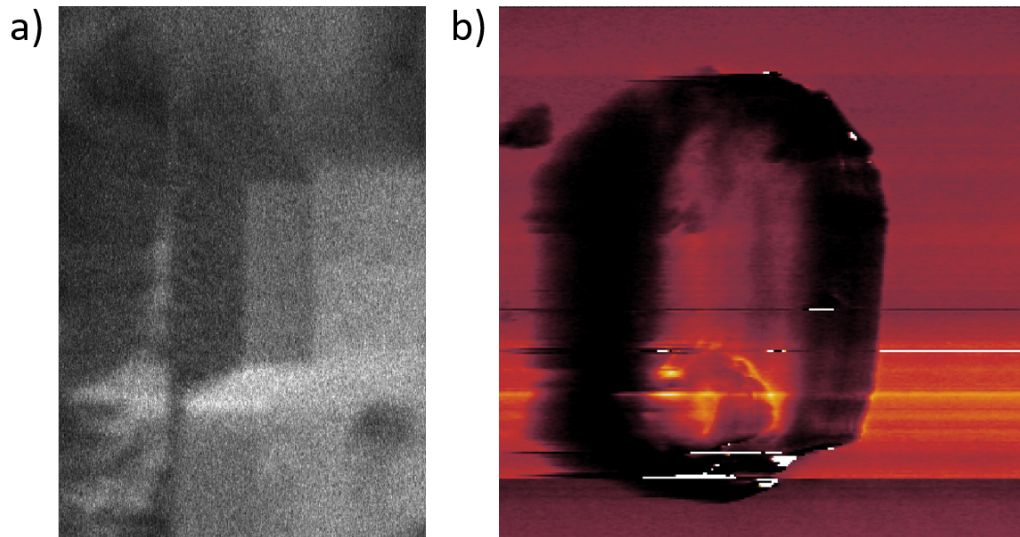


Figure 3.6: a) An SEM image of a stencil deposited magnet on a resonator. The magnet qualitatively looks intact. b) MFM of a magnet. The response on the magnet is the same as the non-magnetic background, demonstrating that there is no significant magnetic response.

### 3.3 IMPROVING MAGNETIC RESPONSE: MAGNETIC PARTICLES

In parallel to this work, characterization of Nd-Pr-Fe-Co-Ti-Zr-B alloy microparticles had been performed for use in superconducting levitation experiments (see chapter 4), and they were found to have high magnetic moments. This inspired the use of these microparticles as the magnetic material for these experiments, as described in this section.

### 3.3.1 DEVICE FABRICATION

Device fabrication is similar to the method described in 3.2.1 above. However, in step 3, there is no longer a hardmask or evaporation step. Instead, the sample is placed into a Focused Ion Beam and Scanning Electron Microscope with a tungsten manipulator tip (FEI Helios 660). This allows imaging and selection of single 1-2  $\mu\text{m}$  particles from a powder. The selected particle is picked up with the manipulator tip and placed onto the center of a beam (figure 3.7), then optionally secured by using the FIB to deposit 30 nm of platinum.

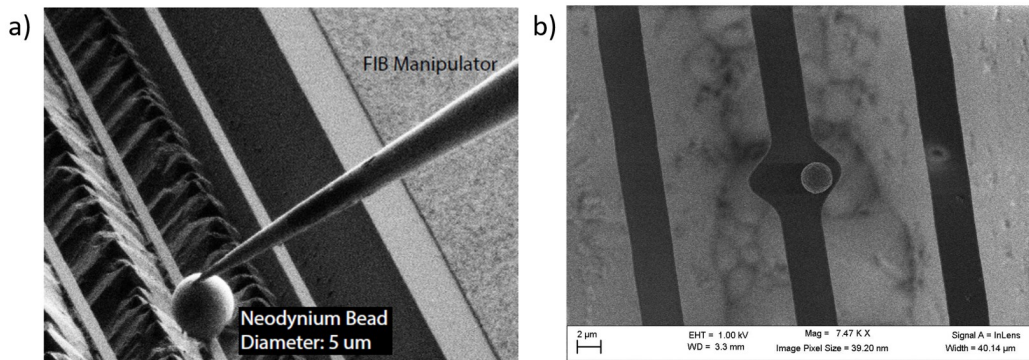


Figure 3.7: a) An SEM of using a tungsten tip to place a magnetic bead onto a released resonator. b) AN SEM showing the final device. These devices have a small pad in the center to simplify particle placement.

### 3.3.2 MAGNETIZATION CHARACTERIZATION

To characterize these devices, we use an ensemble diamond placed on top of the sample. We can then use ESR to determine the magnetic field at each point in the diamond plane. The data are shown in figure 3.8. In 3.8c, we image in a circle around the magnetic particle. For each angle, up to 8 peaks are observed, with each pair corresponding to one of the four NV orientations at each location. The data show an

angular dependence of the splitting, as we would expect only if we were seeing a real magnetic signal. To estimate the gradient, a scan is taken in a line away from the particle as shown in figure 3.8b. The resulting measured gradient is  $> 2 \times 10^4$  T/m, nearly two orders of magnitude improved over the previous design and matching expectations for spherical magnetic particles of this size. The gradients could potentially be improved further by using smaller particles or shaping the particles to be non-spherical. Furthermore, single peaks, corresponding to single transitions, could be isolated for further experiments (figure 3.8d).

This design solved the magnetization challenges seen in the previous iterations. However, it was insufficiently robust. In particular, the particles would detach from the beams during experiments, destroying the sample and preventing couplings from being measured.

### 3.4 FABRICATION AND CHARACTERIZATION OF RESONATORS WITH IRON MAGNETS

In order to increase magnet robustness, an alternate fabrication method was needed. In particular, we want to use an evaporation technique so there will be an adhesion layer between the magnetic material and the silicon nitride. Since a hardmask technique was unsuccessful, this suggests that we instead use a liftoff technique to define the magnets. However, performing lithography on top of released resonators is extremely challenging due to their fragility, so the magnets must be defined before release. And since KOH etches most magnetic materials, we need an alternate release etch so that the magnets will survive the process.

During release, the silicon sacrificial layer underneath the silicon nitride resonator

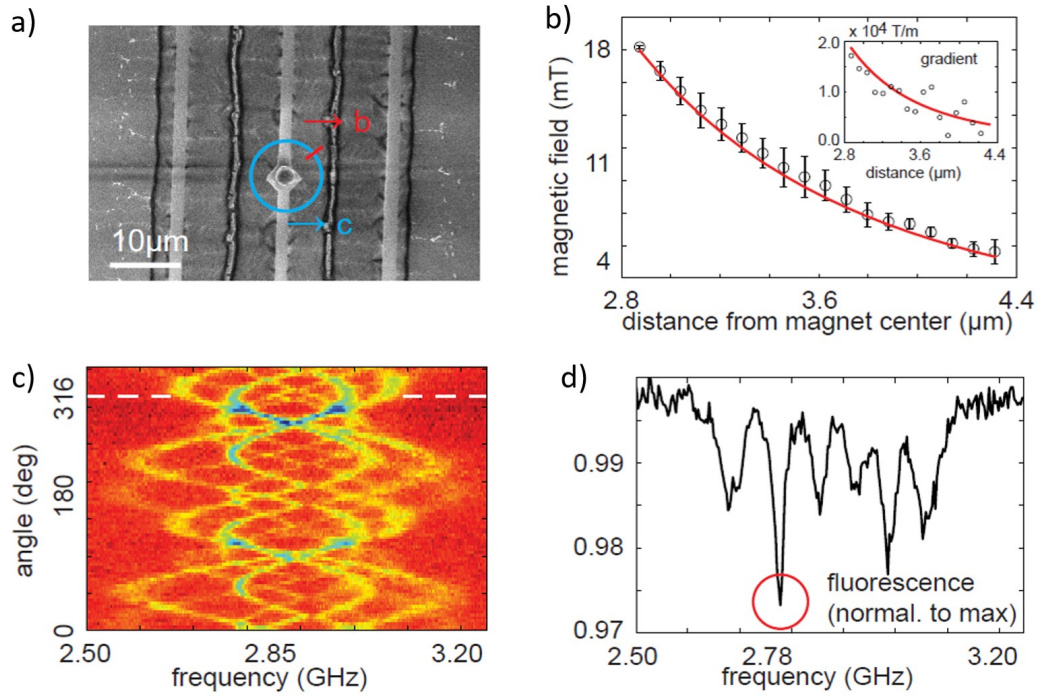


Figure 3.8: Characterization of magnetic particle samples using NVs. a) SEM image of the sample. The blue ring and red line show the scan paths for (b) and (c) respectively. b) Line scan away from the magnet showing the magnetic field at each point. The inset shows the derived gradient of up to  $2 \times 10^4$  T/m. c) Ring scan around the magnet showing an angular dependence of the NV ESR splitting. d) The line corresponding to the dashed white line in (c). Note that we can resolve multiple NV families, and can use an isolated peak for further experiments.

is removed. Thus, in order to underetch the resonators without destroying them, an isotropic etch with an extremely high selectivity of silicon to silicon nitride and magnetic material is required. One such etching chemistry is  $\text{XeF}_2$ , which in our home-made etcher was measured to have a Si:SiN selectivity of  $>2000:1$ , and which does attack only a small set of metals. It had also been used successfully before to release high quality factor silicon nitride resonators with a 30nm layer of Al<sup>34</sup>, which is a

similar case to the one here and thus looked to be a promising direction.

### 3.4.1 DEVICE FABRICATION

Device fabrication is similar to the method described in 3.2.1 above. However, the resonators are not released at the end of step 2. Instead, the magnets are defined with a liftoff technique using e-beam lithography, then a Cr-Fe-Cr trilayer is evaporated. The liftoff is completed, leaving a magnet at the center of each resonator, and then the release occurs using a  $\text{XeF}_2$  etch.

Full details of the process are presented in appendix A.

### 3.4.2 MECHANICS CHARACTERIZATION

The mechanics of these released resonators are characterized using the same method as in 3.2.2. Figure 3.9 shows the results for unloaded resonators. Clear peaks can be measured corresponding to the motional modes of the resonators with quality factors  $Q > 10^5$ . Though these room temperature results are slightly lower than the values demonstrated at cryogenic temperatures for the KOH released resonators in section 3.2.2, it matches the results for those resonators taken at room temperature. Thus, this fabrication method is a viable alternate way of releasing resonators while maintaining the high quality factors required for quantum experiments.

### 3.4.3 MAGNETIZATION CHARACTERIZATION

Now that the behavior of the mechanics meets the requirements, we need to evaluate the magnetic properties. First, we can perform an MFM experiment as in section 3.2.3 to do an initial check of magnet quality. The results are shown in figure

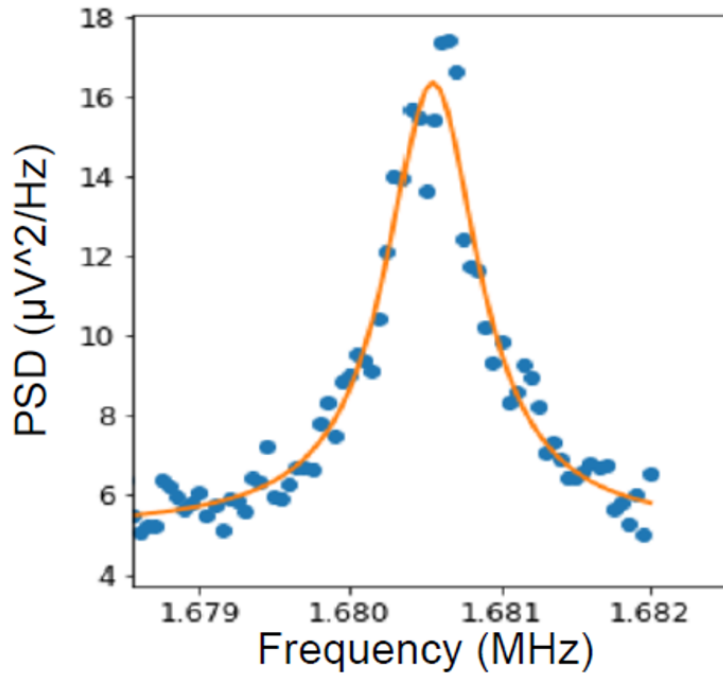


Figure 3.9: The interferometer data for  $\text{XeF}_2$ -released resonators. The quality factor of  $Q > 10^5$  at high vacuum and room temperature is in line with the results for KOH released resonators.

3.10. The signal gradient on the magnet has the opposite direction of the background, rather than matching it, and there are strong signals at the poles of the magnet. The result thus demonstrates that the magnets appear to be bar magnets, as would be expected.

To confirm this result, we use an ensemble diamond to characterize the magnetic fields from magnetized resonators. A scan is taken in a line away from the magnet, as shown in figure 3.11. Points near the magnet register a significantly larger NV splitting (figure 3.11b), which corresponds to a larger magnetic field. These data (figure 3.11c) can be used to approximate a magnetic field gradient of  $1.2 \times 10^3$  T/m. How-

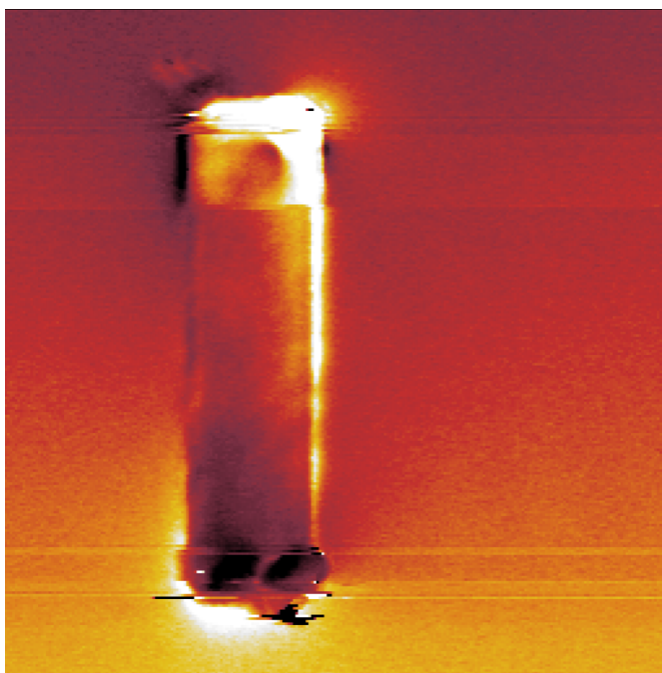


Figure 3.10: MFM of a Cr-Fe-Cr liftoff magnet. The response on the magnet is much different than the non-magnetic background and there are strong signals at the poles, demonstrating magnetization and matching what we would expect for a bar magnet.

ever, this magnets use Iron, which is a soft magnet, as the magnetic layer. This means that we can further increase the gradient by applying a field along the easy axis of the magnet (along the resonator) to bring the magnetic moment above the remnant magnetization. The result is shown in the orange curve in figure 3.11c. Even applying only a 40G external field, the gradient is boosted by more than a factor of four to  $5 \times 10^3$  T/m. Applying increasingly large fields should further increase the measured gradient, with the caveat that all fields must be aligned to the NV axis to maintain NV functionality.

An additional concern is that magnetic noise could potentially affect NV lifetimes. To test this, we ran a Hahn echo experiment on the current configuration, with the

results shown in figure 3.11d. This demonstrated a  $T_2 > 100\mu\text{s}$ , which matches expectations for these samples without a nearby noise source.

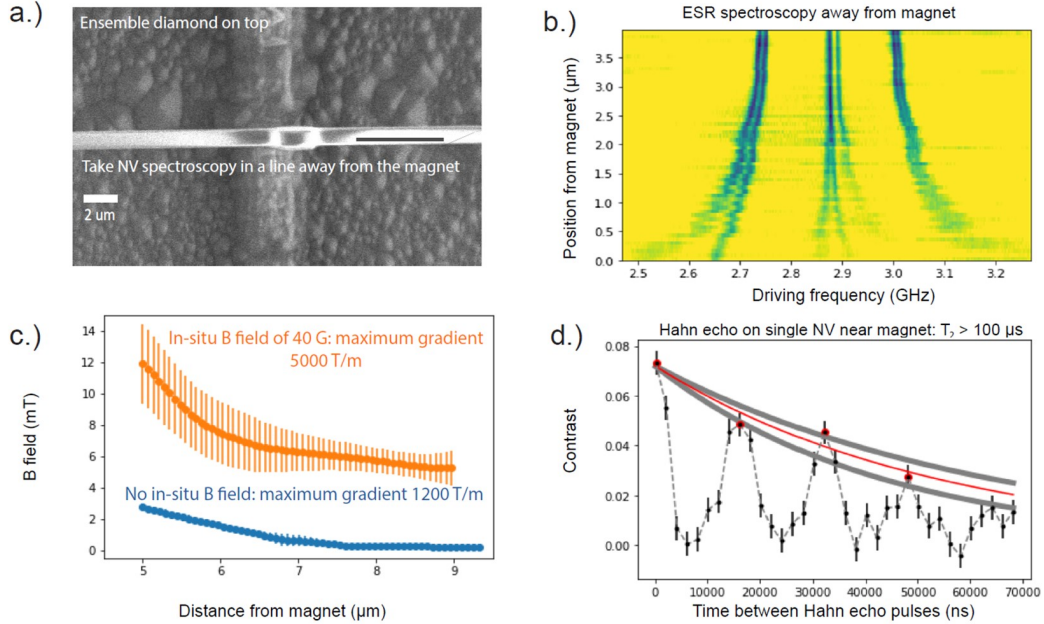


Figure 3.11: Characterization of liftoff magnet samples using an ensemble NV diamond. a) SEM image of the sample. The black line shows the line scan shown in (b). b) Line scan away from the magnet showing the magnetic field at each point. Note that points closer to the magnet have a larger splittings, indicating that the magnets have significant magnetic moments c) Derived magnetic field, showing the remnant field from the magnet (blue) and the boosted field when a 40G field is applied along the NV axis. d) Hahn echo  $T_2$  experiments on an NV near the magnet. Even with the magnet nearby, the NV lifetime remains long

### 3.5 OUTLOOK

In this work, we've demonstrated progress towards a high cooperativity hybrid quantum system with NV centers and silicon nitride mechanical resonators. We now

discuss the improvements that still need to be made to make the system viable, as well as exciting future directions for the work.

### 3.5.1 CURRENT CHALLENGES AND NEXT STEPS

We have independently demonstrated that the samples have good mechanical and magnetic properties. We now want to measure the coupling directly to determine the viability for quantum applications. To do so, we can use an XY8-k dynamical decoupling experiment sequence, as seen in figure 3.12. In such a sequence, a series of pi pulses is applied to the NV with a time separation  $\tau$ . When  $\tau$  is matched to the resonator frequency, the spin flips of the NV are matched with the displacement directional flips of the resonator, leading to phase accumulation that doesn't occur when  $\tau$  is mismatched. This leads to a contrast dip in the signal at this key  $\tau$  value. The resulting curve can be fit to a theoretical model to extract the coupling parameters.

However, there is a technical challenge that has arisen with current samples. In order to take these measurements in a reasonable amount of time, we need to be able to measure the mechanical resonance frequency in order to be able to choose the tau range to sweep over. Unfortunately, current resonators occasionally break during interferometer measurements. The likely cause is residual resist on the beams from the liftoff step, which strongly absorbs the incident light, heating and melting the beam. Beam damage was reduced by using an O<sub>2</sub> plasma etch on the samples, but this also decreased the measured magnetic moment, implying oxidation of the magnetic material. Similarly, the strongest resist removal etches such as piranha cause severe damage to the magnets. However, initial experiments with using heated Remover PG rather than acetone for liftoff shows initial promising results for removing this residue and allowing these exciting experiments to continue.

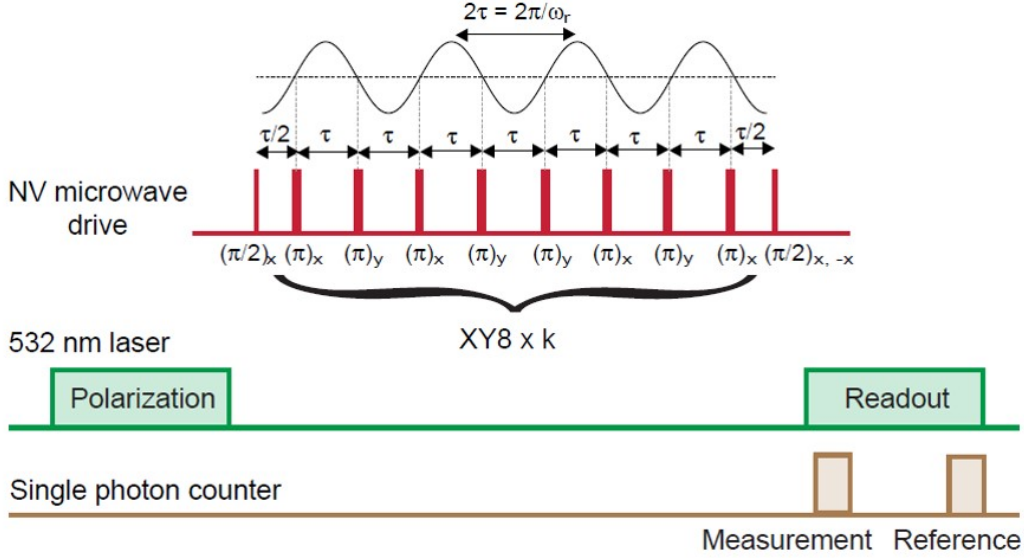


Figure 3.12: Schematic of an XY8-k sequence that could be used to derive the resonator-NV coupling. The signal resulting from this experiment can be fit to theoretical models to extract the coupling.

### 3.5.2 FUTURE WORK

There are myriad exciting next steps that are possible, both in terms of technical improvements and physics explorations. For technical improvements, we want to continue to push the figures of merit for our devices. We’ve mechanical demonstrated quality factors of  $Q > 10^6$ , but recent work with phononic engineering of silicon nitride resonators has pushed this to  $Q > 8 \times 10^8$ <sup>32</sup>. By performing similar optimizations for our geometries, we could hope to gain multiple orders of magnitude improvement in our own devices. Similarly, by optimizing the shape and composition of our magnets, we hope to increase the magnetic field gradients at nearby NVs and thus open the door to new types of quantum experiments.

What sort of experiments are possible with parameters we can realize currently

or in the near future? One exciting opportunity is to cool the resonator through the NV. The intuition is that the coupling between the NV and the mechanical mode can allow us to transfer phonons from that mode to an NV in the  $|0\rangle$  state, cooling the resonator but causing the NV to undergo a  $|0\rangle$  to  $|1\rangle$  transition. The NV can then be optically pumped back to the  $|0\rangle$  state, recooling it. If the resonator is coupled to a large number of NVs, for example in a high density (black) ensemble diamond, then the resulting cooling rate can be quite high with an even modest coupling. The resulting steady state phonon occupation depends on the equilibrium reached between this cooling and the reheating from the environment, related to the resonator quality factor. For a 1 MHz resonator starting at 4K with a quality factor of  $Q = 10^6$ , coupled to  $10^6$  NVs with a  $T_1$  of 18  $\mu$ s, the cooling dynamics are shown in figure 3.13. With even this modest coupling, the resonator is able to be cooled to just above the ground state.

Additional experiments become possible as the coupling improves. For example, we could measure the backaction of a single NV on the resonator, or implement quantum metrology schemes such as spin squeezing. These provide interesting short and medium term goals as we progress towards improved sample engineering that will hopefully enable strong coupling to be achieved, allowing the realization of two-qubit gates mediated by a mechanical bus and opening this system up to be used as a platform for quantum information experiments.

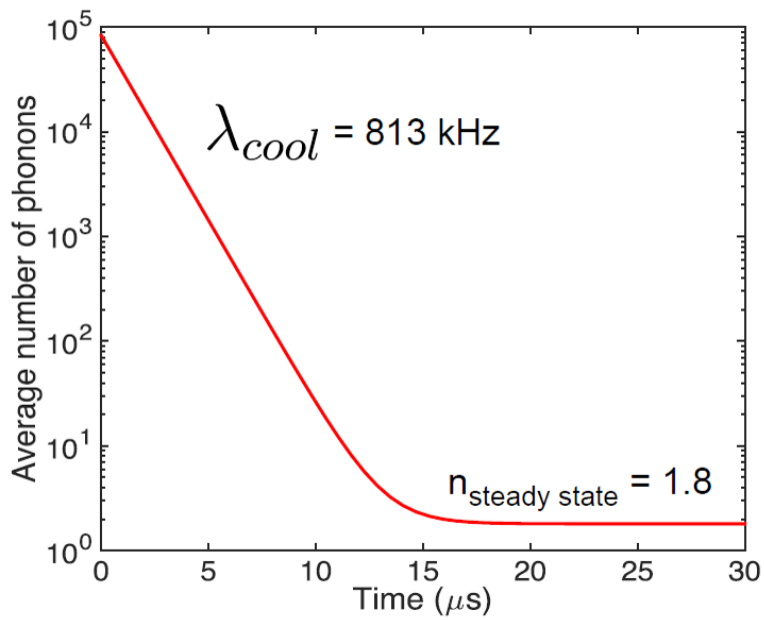


Figure 3.13: Cooling dynamics for a 1 MHz resonator starting at 4K with a quality factor of  $Q = 10^6$ , coupled to  $10^6$  NVs with a  $T_1$  of 18  $\mu\text{s}$ . Note that with these parameters, the resonator can be cooled to nearly the ground state.

# 4

## Single-Spin Magnetomechanics with Levitated Micromagnets

### 4.1 INTRODUCTION

Realizing coherent coupling between individual spin degrees-of-freedom and massive mechanical modes is an outstanding challenge in quantum science and engineering.

The spin's strong quantum non-linearity facilitates preparation of macroscopic quantum states of motion<sup>15</sup>, while the mechanical mode can mediate effective spin-spin interactions between distant spin-qubits<sup>35</sup>. This enables applications in quantum information processing<sup>26</sup>, sensing<sup>13,36,37</sup>, and fundamental physics<sup>38,39</sup>. One particularly promising approach is to engineer a strong spin-mechanical coupling via magnetic field gradients<sup>14,40,41,42,43</sup>. Achieving strong spin-resonator coupling requires a combination of high quality mechanical resonators, strong magnetic field gradients, and spin qubits with very long spin coherence times, such that the coupling exceeds the decoherence rates of the two subsystems.

In this chapter, we propose and demonstrate a new platform for strong spin-mechanical coupling based on levitated microscopic magnets coupled to the electronic ground state of a single nitrogen vacancy (NV) center in diamond (Fig.4.10). The key idea is to utilize a levitated magnet that is localized in free space by electromagnetic fields. In such a system, dissipation is minimized since there is no direct contact with the environment. Specifically, we make use of a levitating mechanical resonator based on magnetostatic fields. This approach not only avoids clamping losses, but also circumvents photon recoil and heating associated with optical levitation<sup>44,45,46,47,48</sup> and is therefore predicted to yield large mechanical quality factors<sup>49,50</sup>. In addition, the levitated magnet naturally generates the strong magnetic field gradient that is required for spin-mechanical coupling. We specifically demonstrate the coupling to an individual NV-center, one of the most studied color centers in diamond<sup>28</sup>. Besides optical initialization and readout, the NV-center features long coherence times, which makes it an attractive candidate for scalable quantum networks in the solid state<sup>26</sup>, quantum sensing<sup>51,52,53</sup> and quantum communication<sup>24</sup>.

So far, experiments with superconducting levitation have been limited to millimeter-

scale magnets<sup>54,55,56,57</sup>. A recent experiment<sup>11</sup> demonstrated superconducting levitation of micro-magnets, but without spin-mechanical coupling and with much lower frequencies and Q-factors than shown here. A concurrent experiment<sup>12</sup> demonstrated a high quality factor, but similarly with lower frequencies and without spin-mechanical coupling. Levitated spin-mechanical systems in which the spin is hosted inside the resonator have been implemented with nano-diamonds containing NV-center defects trapped in optical tweezers<sup>58,59</sup>, Paul traps<sup>60,61,62</sup> and magneto-gravitational traps<sup>63,64</sup>. Nonetheless, the challenge remains to integrate these systems with strong magnetic field gradients, long coherence NV-centers and operation under ultra-high vacuum conditions. Our approach fulfills all these criteria simultaneously (Fig.4.10).

## 4.2 THEORY OF MAGNETIC LEVITATION

The simplest model for magnetic levitation above a superconductor considers levitation of the magnet above a type-I superconductor, with trapping only in the vertical direction. This can be modeled using the method of images, and extended to a three dimensional trap by introducing a defect into the superconductor. Furthermore, the trapping frequencies can be drastically increased by instead using a type-II superconductor in the field-cooled regime, where there is a magnetic field applied to the superconductor from the magnetic particle as it passes the critical temperature. In this section, we will give both intuitive pictures and quantitative descriptions of the trapping dynamics for these two cases.

### 4.2.1 LEVITATION ABOVE A SUPERCONDUCTOR: FROZEN DIPOLE METHOD

To compute the trap behavior for the case of a magnetic particle levitated over a superconductor, we use the frozen dipole method<sup>65</sup>. Assume that the magnetic particle is a dipole, and that it is levitated above an infinitely thin superconductor \* in its complete shielding state.

The total potential energy of the levitated magnet is given by

$$U(\mathbf{r}, \boldsymbol{\theta}) = -\hat{\boldsymbol{\mu}} \cdot \mathbf{B}_{\text{tot}} + mg_0 z \quad (4.1)$$

where  $m$  is the mass of the magnet, and  $g_0 = 9.81 \text{ m/s}^2$ .

To determine the effective total magnetic field, note that we can model the response of the superconductor as two dipoles. First consider the case where the magnetic particle starts infinitely far away from the superconductor (the type-I or Meissner effect case). The superconductor cannot be penetrated by any magnetic flux, so the currents in the superconductor must create a magnetic field distribution to cancel the magnetic field at the surface. However, for a magnet at a height  $z$ , we can also achieve this by having a 'image' dipole, reflected from the real dipole around the horizontal axis, at  $-z$ . By the uniqueness theorem, this must be equivalent to the superconductor field.

Now consider the case where instead the magnetic particle is held at a height  $h$  above the superconductor during cooldown as the critical temperature is passed. Now, in the 'field-cooled regime', the superconductor has flux trapped inside, so that rather than expelling the magnetic field the superconductor instead maintains the initial

---

\*In our experiment, the magnetic particles have diameters in the tens of microns, and they are centered on a millimeter scale superconductor, so we expect edge effects to be minimal.

magnetic field impinging on it. This initial condition is modeled with a 'frozen' dipole at  $-h$  with the same magnitude as the real dipole but reflected about the vertical axis. As the particle moves, the image dipole moves with the particle, but the frozen dipole stays at this initial position. Equivalently, we can think of this as the superconductor trying to maintain the particle at its initial position during cooldown to maintain the initial field on it (for a perfectly hard superconductor in the absence of gravity), which leads to that position intuitively being the center of the trap. Note that in the frozen dipole model, the image and frozen dipoles overlap and cancel each other at this position, leading to no response from the particle as one would expect. In addition, any deviation away from that center results in a restoring force from this combination of dipoles.

Let us now quantify this effect. The effective total magnetic field on the particle is given by

$$\mathbf{B}_{\text{tot}} = \left[ \mathbf{B}(\hat{\boldsymbol{\mu}}_f, \mathbf{r} - \mathbf{r}_f) + \frac{1}{2} \mathbf{B}(\hat{\boldsymbol{\mu}}_i, \mathbf{r} - \mathbf{r}_i) \right] \quad (4.2)$$

the sum of the field from the frozen dipole and the image dipole <sup>†</sup>. Here,

$$\mathbf{r} - \mathbf{r}_f = \begin{pmatrix} x \\ y \\ z + h_{\text{cool}} \end{pmatrix}, \quad \hat{\boldsymbol{\mu}}_f = \mu_m \begin{pmatrix} -\sin(\theta_{\text{cool}}) \\ 0 \\ \cos(\theta_{\text{cool}}) \end{pmatrix} \quad (4.3)$$

---

<sup>†</sup>Note that the potential energy  $U_i = -q^2 \int_{\infty}^z \frac{1}{z'+z} dz' = q^2/4z$  of a charge in the field of its image charge is half the potential energy of a charge in the field of another *real* charge  $U_c = -q^2 \int_{\infty}^z \frac{1}{z'+z} dz' = q^2/2z = 2U_i$ .

are the position and orientation of the frozen dipole and

$$\mathbf{r} - \mathbf{r}_i = \begin{pmatrix} 0 \\ 0 \\ 2z \end{pmatrix}, \quad \hat{\boldsymbol{\mu}}_i = \mu_m \begin{pmatrix} \cos(\phi) \sin(\theta) \\ \sin(\phi) \sin(\theta) \\ -\cos(\theta) \end{pmatrix} \quad (4.4)$$

are the position and orientation of the image dipole, respectively, with  $\mathbf{r}$  the position of the magnet and  $\boldsymbol{\theta} = (\theta, \phi)$  its orientation. Note that due to the symmetry of the problem, we can choose the polar angle of the frozen dipole to be zero.

The field produced by a dipole  $\hat{\boldsymbol{\mu}}$  at a distance  $\mathbf{r}'$  is given by

$$\mathbf{B}(\mathbf{r}', \hat{\boldsymbol{\mu}}) = \frac{\mu_0}{4\pi} \left( \frac{3\mathbf{r}'(\hat{\boldsymbol{\mu}} \cdot \mathbf{r}')}{r'^5} - \frac{\hat{\boldsymbol{\mu}}}{r'^3} \right) = \frac{\mu_0 \mu_m}{4\pi h_o^3} f(\bar{\rho}) \mathbf{e}_B \quad (4.5)$$

For further analysis, it is convenient to write this potential in a dimensionless form  $U_0(\mathbf{r}; h_{\text{cool}}, \theta_{\text{cool}}) = U_s u_s(\mathbf{u}_s)$ , where the energies are scaled by some characteristic energy scale  $U_s$  and the lengths are scaled by some characteristic length scale  $l_s$ . Natural choices for this length scale are the critical radius  $a_{\text{crit}} = B_r^2 / (16g_o \rho \mu_0)$ , the levitation height for the Meissner case (i.e. initial condition with magnet at infinity)  $h_I$ , and the particle radius  $a$ . Table 4.1 lists the characteristic energies for the three cases.

$l_s$	$a_{\text{crit}}$	$a$	$h_I$
$U_s$	$mg_o a^3 / a_{\text{crit}}^2$	$mg_o a_{\text{crit}}$	$mg_o h_I$
$\alpha_s$	$\alpha^{-3}$	$\alpha$	1

Table 4.1: Characteristic scales for different normalizations

The dimensionless state vector for the physical coordinates  $\mathbf{r} = [x, y, z, \theta, \phi]$  is given by  $\mathbf{u}_s = \mathbf{A}\mathbf{r} = [x/l_s, y/l_s, z/l_s, \theta, \phi] = [x_s, y_s, z_s, \theta, \phi]$ , where  $\mathbf{A} = \text{diag}(1/l_s, 1/l_s, 1/l_s, 1, 1)$ .

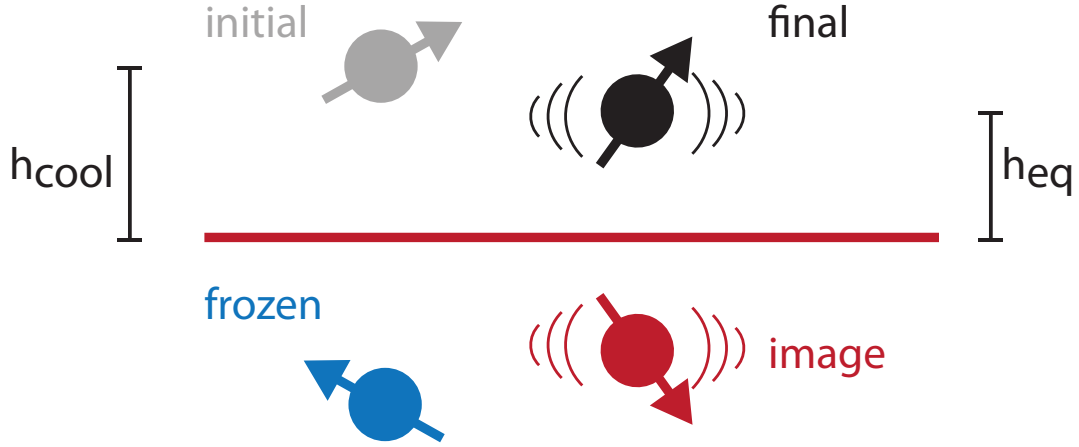


Figure 4.1: Effective model for the magnet and superconductor interaction. The magnetic particle is initially held a height  $h_{cool}$  above the superconductor (red line) above the critical temperature. As the superconductor is cooled past the critical temperature, it traps flux leading to a field identical to that formed by the 'frozen' dipole. There is a second 'image' dipole which follows the motion of the particle, leading to a trap at a height  $h_{eq}$  above the superconductor.

The dimensionless potential is then given by

$$u_s(\mathbf{u}_s; h_{cool}, \theta_{cool}, \alpha_s) = [\alpha_s z_s + g(\mathbf{u}_s; h_{cool}, \theta_{cool})] \quad (4.6)$$

where the prefactor  $\alpha_s$  is given in table 4.1 and  $\alpha = a/a_{crit}$  is the particle radius normalized to the critical radius.

The second term in Eq. (4.6) is given by

$$g(\mathbf{u}; h_{cool}, \theta_{cool}) = \left( \frac{3 + \cos(2\theta)}{6z^3} - \frac{16 [\cos(\theta)g_c(\mathbf{u}; h_{cool}, \theta_{cool}) + \sin(\theta)g_s(\mathbf{u}; h_{cool}, \theta_{cool})]}{3 [(h_{cool} + z)^2 + x^2 + y^2]^{5/2}} \right) \quad (4.7)$$

with

$$g_c(\mathbf{u}; h_{\text{cool}}, \theta_{\text{cool}}) = [2(h_{\text{cool}} + z)^2 - x^2 - y^2] \cos(\theta_{\text{cool}}) - 3x(h_{\text{cool}} + z) \sin(\theta_{\text{cool}}) \quad (4.8a)$$

$$g_s(\mathbf{u}; h_{\text{cool}}, \theta_{\text{cool}}) = 3(h_{\text{cool}} + z) (x \cos(\phi) + y \sin(\phi)) \cos(\theta_{\text{cool}}) \quad (4.8b)$$

$$+ [((h_{\text{cool}} + z)^2 - 2x^2 + y^2) \cos(\phi) - 3xy \sin(\phi)] \sin(\theta_{\text{cool}})$$

From the potential we obtain the force via the gradient<sup>‡</sup>,  $f(\mathbf{r}) = -\partial_{\mathbf{r}}U_0(\mathbf{r}) = -U_s\mathbf{A}\partial_{\mathbf{u}}u_s(\mathbf{u})$ . At equilibrium, the force vanishes  $\mathbf{f}(\mathbf{u}_{\text{eq}}) = 0$  and a Taylor expansion of the force around equilibrium gives  $\mathbf{f}^{\text{eq}}(\mathbf{u}) \approx -U_s\mathbf{A}\mathbf{k}_s\mathbf{u}$ , where the elements of the stiffness matrix  $\mathbf{k}_s$  are given by  $k_{ij} = \partial_{u_i}\partial_{u_j}g(\mathbf{u})|_{\mathbf{u}=\mathbf{u}_{\text{eq}}}$ .

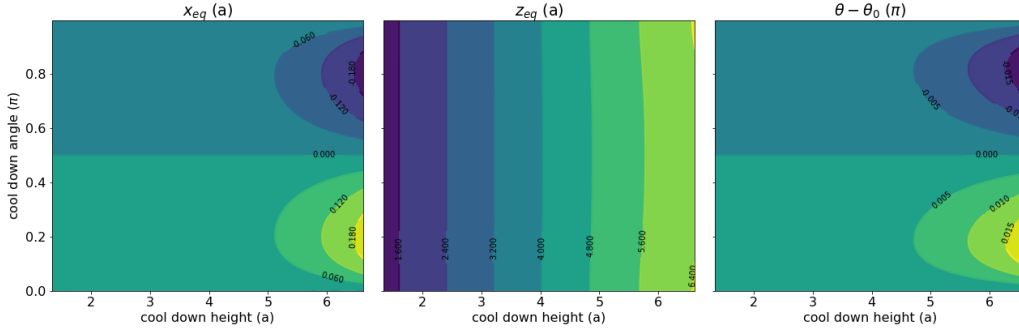


Figure 4.2: Equilibrium position and orientation for a  $a = 22.5\mu\text{m}$  radius magnet. All length scales are normalized to the radius  $a$ .

Finally, the equation of motion around the equilibrium is given by

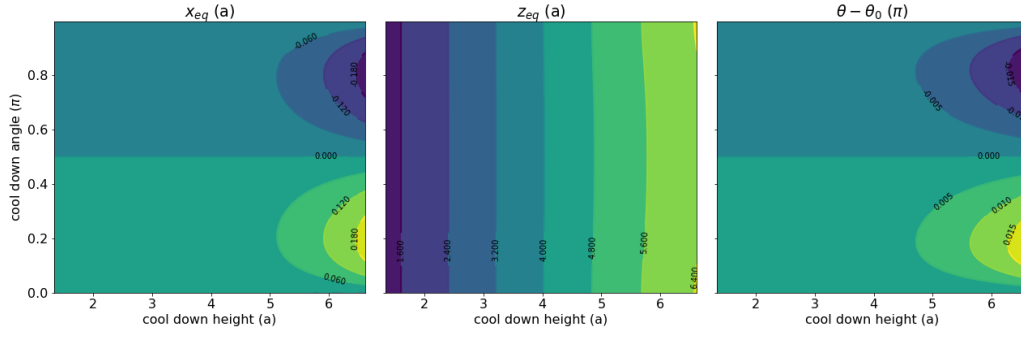
$$\ddot{\mathbf{u}} + \mathbf{W}\mathbf{u} = 0 \quad (4.9)$$

<sup>‡</sup>Here, we drop the arguments for the initial conditions  $(h_{\text{cool}}, \theta_{\text{cool}}, \alpha)$  and the subscript  $s$  for ease of notation.

with  $\S \mathbf{W} = U_s \mathbf{A}^2 \hat{\boldsymbol{\mu}}^{-1} \mathbf{k}_s$  and the mass matrix  $\hat{\boldsymbol{\mu}} = \text{diag}(m, m, m, I_m, I_m)$ , where  $m$  and  $I$  are the mass and the moment of inertia of the particle. For a spherical particle,  $I = 2ma^2/5$  and  $m = 4\pi a^3/3$ . The frequencies are then given by the eigenvalues of  $\mathbf{W} = \omega_0^2 \mathbf{k}$ , where  $\mathbf{k} = \mathbf{I}_{5/2} \mathbf{k}_s$  and  $\mathbf{I}_{5/2} = \text{diag}(1, 1, 1, 5/2, 5/2)$ . Note that  $\mathbf{k}_s = \mathbf{k}_0(h_s, \theta_{\text{cool}}, \alpha)$  depends on the normalized cooldown height  $h_s$  and orientation, and on the size of the particle through the parameter  $\alpha$ . The characteristic frequency is given by

$$\omega_0 = \sqrt{\frac{U_s}{m}} l_s^{-1} \quad (4.10)$$

and the mode frequencies by  $\omega_i = \omega_0 \sqrt{k_i}$ , where  $k_i$  are the eigenvalues of  $\mathbf{k}$ .



#### 4.2.2 SOLUTION IN THE MEISSNER CASE

For the case when we cool the superconductor with the magnet very far away such that there is no flux trapping (Meissner or type I case,  $h_{\text{cool}} \rightarrow \infty$ ), we find

$$g(z_s) = \frac{3 + \cos(2\theta)}{6z^3} \quad (4.11)$$

Thus, the potential minimum is at  $\theta = \pi/2$  and  $z = h_{\text{I}} = (\frac{a^3 B_f^2}{16g\rho\mu_0})^{1/4}$ . The frequencies are  $\omega_i = \omega_0 \sqrt{\kappa_i}$ , with the characteristic frequency

$$\omega_0 = \sqrt{\frac{g}{h_{\text{I}}}} = \frac{g^{1/2}}{a_{\text{crit}}^{1/8}} a^{-3/8} \quad (4.12)$$

and  $\kappa_{1,2,3} = 0$ ,  $\kappa_4 = 4$ ,  $\kappa_5 = (5/3)/(a/h_{\text{I}})^2$ .

Note that without the frozen dipole, this just provides trapping in the vertical direction. The mirror image always follows directly below the magnetic particle, so the problem is completely symmetric about the center of the particle. To get horizontal trapping, we can introduce a defect into the superconductor (by, for example, etching a hole). The resulting trapping potential can be analyzed numerically using finite element methods<sup>9</sup>, and for 10  $\mu\text{m}$  radius hard magnet particles leads to trapping frequencies in the tens of Hz.

#### 4.2.3 APPROXIMATE SOLUTION FOR STRONG FLUX PINNING

Due to its symmetry, the potential (4.6) has a minimum at  $y = \phi = 0$ . From the numerical solution (Fig.4.3) we observe that the equilibrium height depends only very weakly on the cool down angle  $\theta_{\text{cool}}$ . Thus, we may set  $\theta_{\text{cool}} = \pi/2$ . In that case, we

also find that  $\theta_{\text{eq}} = \theta_{\text{cool}}$  and  $x_{\text{eq}} = 0$ . Thus, the only remaining degree of freedom is  $z$  and (4.7) simplifies to

$$g(z_s) = \frac{1}{3z^3} - \frac{16}{3(h_{\text{I}} + z)^3} \quad (4.13)$$

and the equilibrium position  $z = h_{\text{II}}$  is given by the implicit equation

$$h_{\text{cool}}(h_{\text{II}}) = h_{\text{II}} \left[ \frac{2}{(1 - (h_{\text{II}}/h_{\text{I}})^4)^{1/4}} - 1 \right] \quad (4.14)$$

where we used that  $\alpha_s/l_s^4 = h_{\text{I}}^{-4}$  for any normalization.

The resulting frequencies are  $\omega_i = \omega_0 \kappa_i$ , with the characteristic frequency

$$\omega_0 = \frac{B_r}{4\sqrt{\mu_0\rho}} \bar{h}_{\text{cool}}^{-5/2} a^{-1} \quad (4.15)$$

and  $\kappa_1 = 1/2$ ,  $\kappa_2 = 2$ ,  $\kappa_3 = 5\bar{h}_{\text{cool}}^2/3$ ,  $\kappa_{4/5} = \left( [81 + (2\sqrt{5}\bar{h}_{\text{cool}})^4]^{1/2} \pm [9 + (2\sqrt{5}\bar{h}_{\text{cool}})^2] \right) / 12$  and  $\bar{h}_{\text{cool}} = h_{\text{cool}}/a$  is the normalized cooldown height.

Since there are large components of our cryostat's noise spectrum at low frequencies and we want to utilize dynamical decoupling methods when coupling the magnets with NVs, we would like to have frequencies in the kHz even at 10  $\mu\text{m}$  scale particle sizes. Thus, we will experimentally emphasize the strong flux pinning case for this application. Other work done concurrently explores the Meissner case<sup>12</sup>.

### 4.3 EXPERIMENTAL LEVITATION OF MICROMAGNETS

We now experimentally realize the trap described in the previous section. We levitate single hard micro-magnets with a thin film of the type-II superconductor (sc) YBCO (c.f. Fig.4.10). Since we do not apply magnetic fields, the micromagnet is the

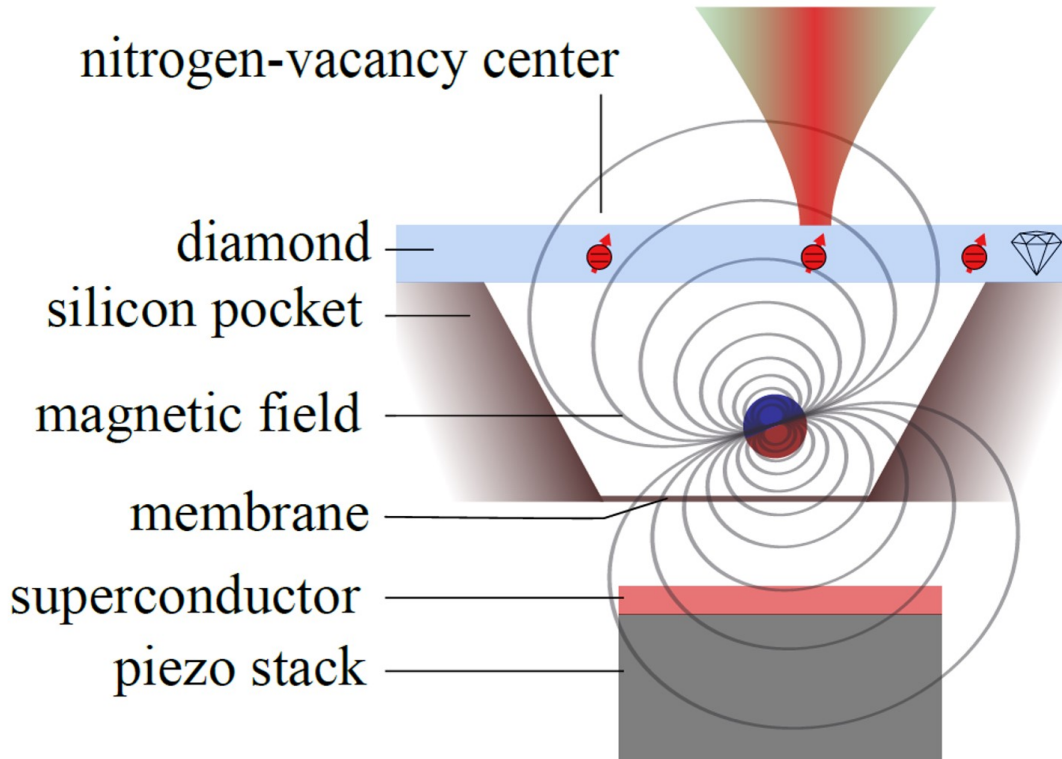


Figure 4.4: This shows the overall concept of the experiment. Individual microscopic hard ferromagnets are isolated in microfabricated pockets and levitated with a type II superconductor, exploiting its flux trapping properties (for details on the pockets and the fabrication procedure, see appendix B). The magnet's stray field allows for efficient coupling between the magnet's motional degrees-of-freedom and bulk nitrogen vacancy centers in the nearby diamond, which generally feature long spin coherence times.

only magnetic field source. Thus, magnetic flux through the YBCO is determined only by the magnet-YBCO distance  $h_{\text{cool}}$  and the magnet orientation  $\theta_{\text{cool}}$ . After cooling YBCO below its critical temperature  $T_c \approx 90\text{K}$ , it becomes superconducting and traps the magnetic flux that penetrates it. Consequently, below  $T_c$ , motion of the

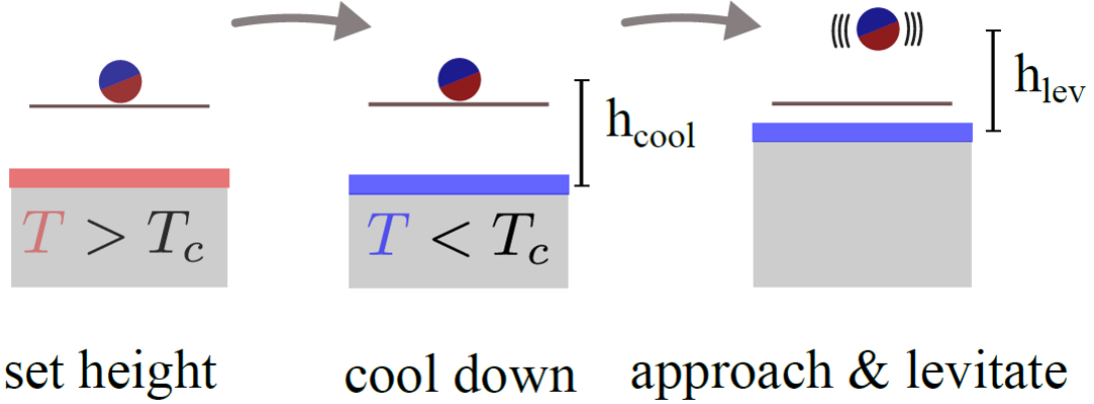


Figure 4.5: The levitation height during cooldown  $h_{cool}$  is set using an attocube piezo stack. Then after cooldown, the piezo stack raises the superconductor towards the particle until the surface forces between the particle and the membrane on which it sits are overcome and levitation is achieved.

magnet induces currents in the superconductor that counteract changes in the magnetic field. This allows for stable 3D trapping using a procedure illustrated in (Fig. 4.5), with levitation height ( $h_{lev}$ ) and trapping frequencies  $\omega_j$  ( $j = x, y, z$ ) depending on the conditions during cooldown.

We observe the levitated magnet through a microscope objective that is positioned outside the vacuum chamber, and record its motion with a fast camera (Fig.4.6).

From the video frames, we extract time-traces of the particle's center-of-mass position in the camera coordinate system  $(x_c(t), y_c(t))$  and calculate their power spectral densities (PSD). The distinct peaks in the PSDs correspond to the three center-of-mass modes  $\omega_j/2\pi$  (Fig.4.7).

Fig.4.9a displays the center-of-mass frequencies as a function of the normalized levitation height  $\bar{h}_{lev} = h_{lev}/a$  for two particles with radius  $a_1 = 23.2 \pm 0.7\mu\text{m}$  and  $a_2 =$

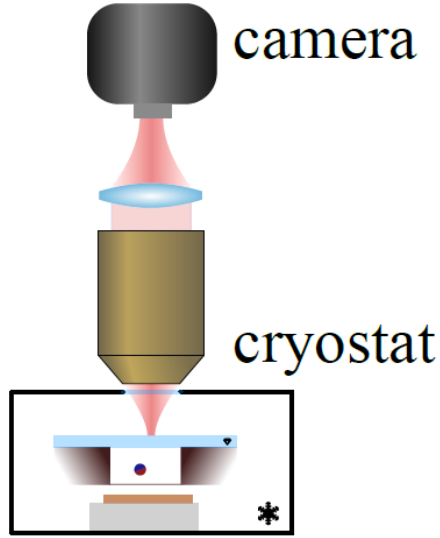


Figure 4.6: We observe the magnet motion through a microscope objective and record its motion with a video camera at up to 12000 fps.

$15.5 \pm 0.3 \mu\text{m}$ , respectively. The lines are a fit to a power law  $f(\bar{h}_{\text{lev}}) = f_{\text{max}} \bar{h}_{\text{lev}}^{-\beta}$ , where  $f_{\text{max}}$  is the frequency in the limit when the gap between the particle and the superconductor vanishes. In our experiment, we find  $f_{\text{max}} = (2.3 \pm 0.4, 2.4 \pm 0.4, 5.6 \pm 1.0) \text{kHz}$  and  $\beta = (1.9 \pm 0.1, 2.1 \pm 0.1, 2.0 \pm 0.1)$  for particle 1 and  $f_{\text{max}} = (8.8 \pm 1.1, 9.5 \pm 1.1, 25.2 \pm 3.3) \text{kHz}$  and  $\beta = (2.1 \pm 0.1, 2.1 \pm 0.1, 2.3 \pm 0.1)$  for particle 2, which is in good agreement with the expected value of  $\beta = 2.5$  from a simple dipole model. The measured center-of-mass frequencies are comparable to those achieved with optical levitation<sup>46,47</sup> and significantly exceed motional frequencies in Paul traps<sup>66</sup> and magneto-gravitational traps<sup>63,64</sup>. However, the observed dependence of the maximum frequency on the particle radius is stronger than the dipole model's prediction of  $f_{\text{max}}^{dp} \propto 1/a$ . We attribute this to the multi-domain nature of our particles and note that spherical particles as large as  $a \sim 1 \mu\text{m}$  can be single domain<sup>67</sup>.

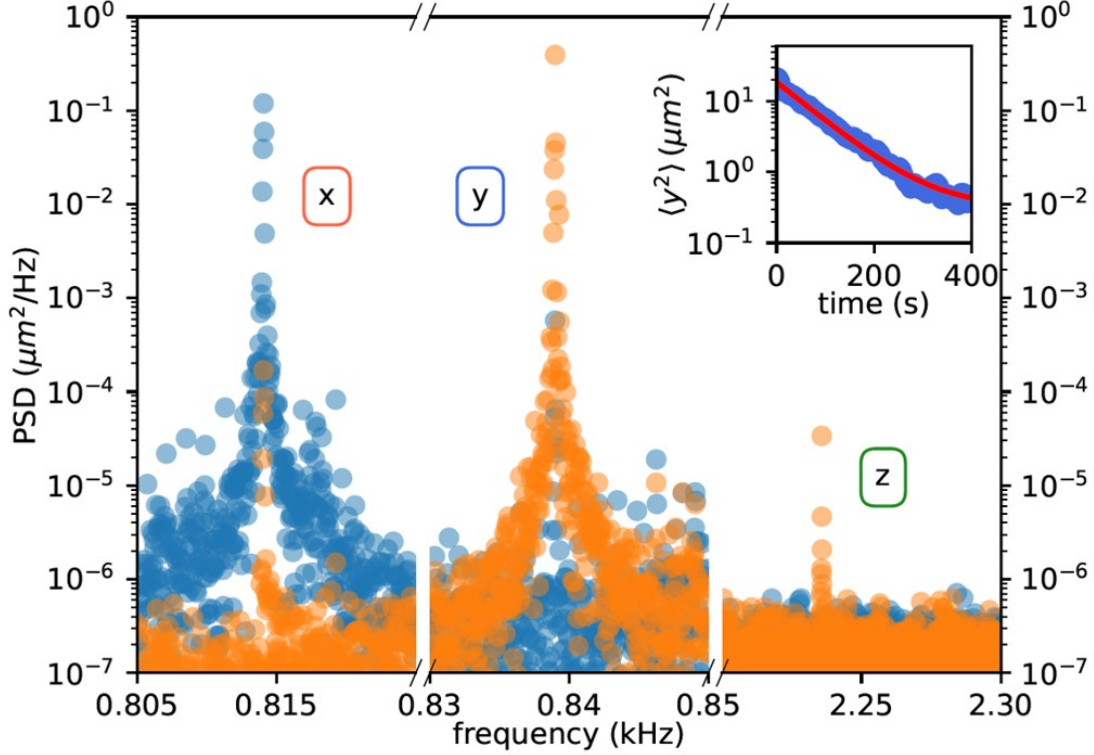


Figure 4.7: Power spectral density extracted from video analysis of the magnet motion in the vertical (orange) and horizontal (blue) direction in the top-down image. The inset shows a typical ringdown measurement of the y-mode ( $\omega_y = 0.839\text{kHz}$ ) from which we extract the Q-factor.

Fig.4.9b shows the Q-factors of magnet 1 for three different levitation heights for all three translational modes. We measure the dissipation with ring down measurements, exciting one mode with an AC magnetic field and observing its energy decay (Fig.4.7 inset). From an exponential fit we extract the decay time  $1/\gamma_j$  and the Q-factor  $Q_j = \omega_j/\gamma_j$  for each mode. The measured Q-factors are around one million and depend only weakly on the trapping frequencies and thus on the levitation height. Air damping can be ruled out at our experimental conditions with pressures below

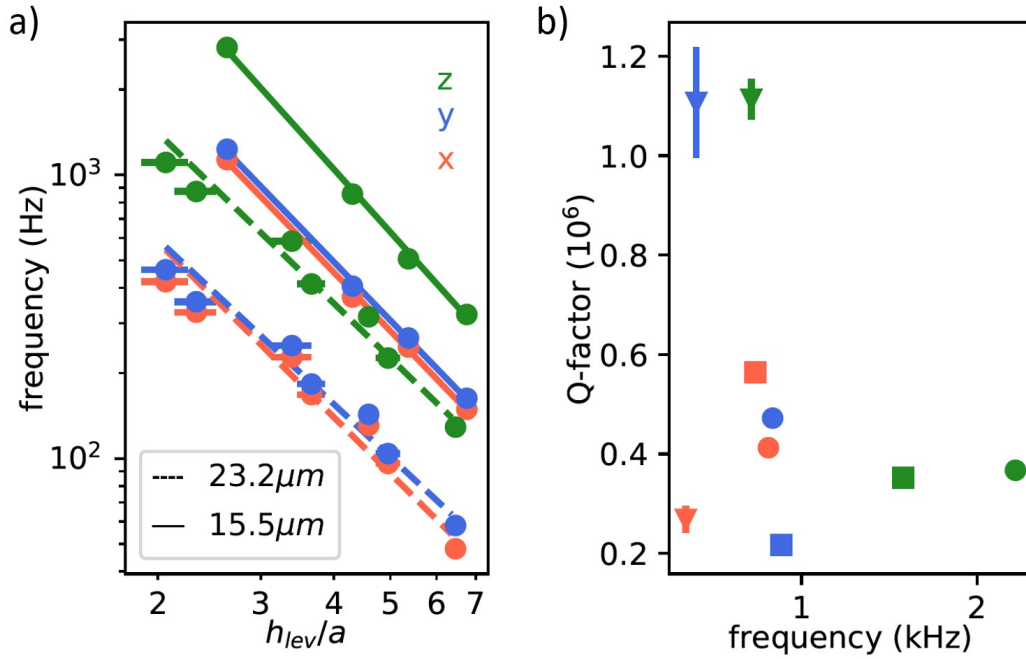


Figure 4.8: (a) Frequencies of center-of-mass motion as a function of the levitation height normalized to the magnet radius. Dashed (solid) lines show the three center-of-mass modes for magnet 1 (2). (b) Q-factor as a function of trap frequency for the magnet 2. Each symbol corresponds to a different levitation experiment and the different colors corresponds to the three different center-of-mass modes

$10^{-5}$  mBar (see the detailed analysis in appendix B), and the most likely source of dissipation is the magnet-superconductor interaction. This dissipation mechanism provides an interesting avenue for further study, and we could potentially be able to reach further improvements by fabrication improvements in the superconductor, such as using heavy ion implantation to provide stronger pinning sites and decrease potential flux flow losses<sup>68,69</sup>. Note that, even though this Q-factor is somewhat lower than what has been demonstrated with non-magnetic optically levitated<sup>48</sup> and nano-

fabricated mechanical resonators<sup>70,71,72,32</sup>, it represents the state of the art for magnetized resonators<sup>73,74</sup> and the ultimate limit, in particular for magnets with  $a < \mu\text{m}$ , is still an open question.

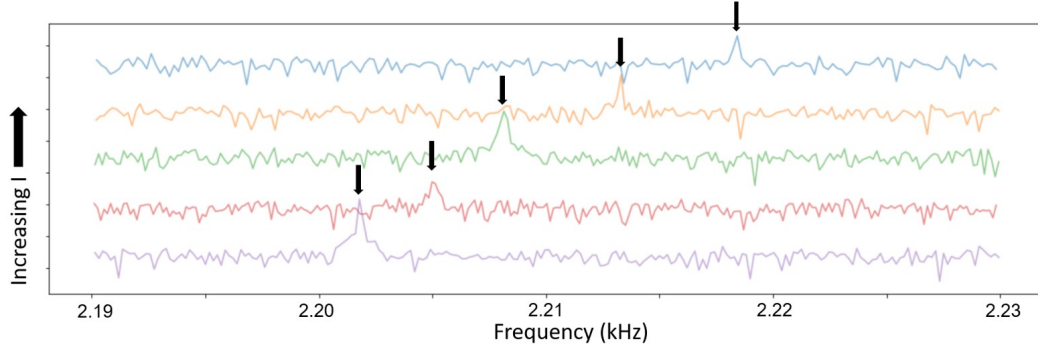


Figure 4.9: The frequencies of the modes can be further tuned by applying an external DC field with a gradient at the location of the particle. The arrows provide a visual guide to the location of the motional peak, which shifts right as the current is increased through the external coil.

The frequencies can be further tuned by applying an external DC field. Here, we placed a copper coil on top of the cryostat and ran current through it, leading to a field gradient inside the chamber and a force on the particle proportional to the applied current. This could be used to, for example, stay resonant with another drifting frequency without having to thermally cycle.

#### 4.3.1 COUPLING BETWEEN THE NV AND A MOVING MAGNETIC DIPOLE

For weak magnetic fields, where the quantization axis of the NV does not change due to the Zeeman term, the transition frequency is  $\omega_s = \omega_0 + \gamma_s B_{\parallel}$ , where  $B_{\parallel} = \mathbf{B} \cdot \mathbf{n}_s$  is the projection onto the NV-axis and  $\gamma_s = g_s \mu_B / \hbar$  is the gyromagnetic ratio of the

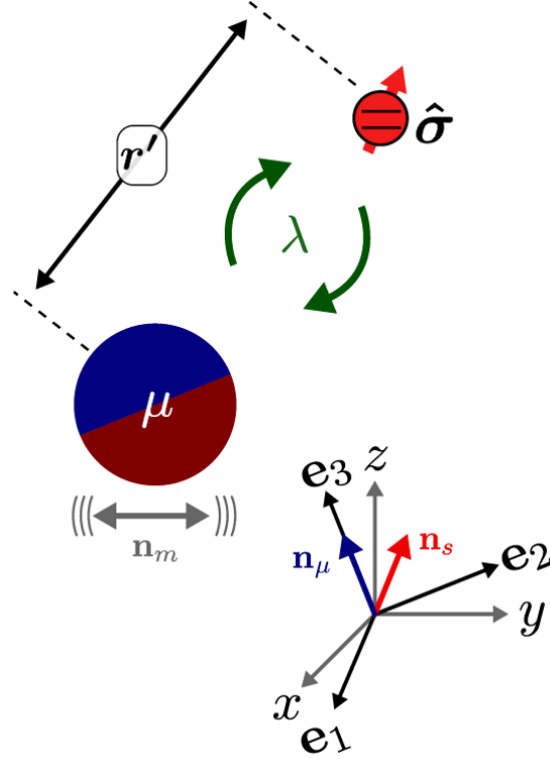


Figure 4.10: The coupling  $\lambda$  depends on the relative orientation of the NV-center,  $\mathbf{n}_s$ , the magnetic moment  $\mathbf{n}_\mu$ , the direction of motion of the magnet  $\mathbf{n}_m$ , the distance between the magnet and the NV-center  $r'$ , the magnet radius  $a$  and the frequencies of the motion.

NV center. Hence, the coupling is

$$\lambda_s = \gamma_s (\nabla B_{\parallel}) \cdot \mathbf{u}_m x_{zp} \quad (4.16)$$

with  $\mathbf{u}_m$  being the direction in which the particle moves and  $x_i$  being the displacement. Assuming that the field from the particle is a dipole with dipole moment  $\boldsymbol{\mu}$ , the

magnetic field from the magnet is

$$\mathbf{B}(\mathbf{r}', \boldsymbol{\mu}) = \frac{\mu_0}{4\pi} \left( \frac{3\mathbf{r}'(\boldsymbol{\mu} \cdot \mathbf{r}')}{r'^5} - \frac{\boldsymbol{\mu}}{r'^3} \right) = \frac{\mu_0}{4\pi} \frac{\mu}{r'^3} \mathbf{e}_B \quad (4.17)$$

where  $\mathbf{e}_B(\theta, \phi) = 3\mathbf{e}_{r'}(\mathbf{e}_{r'} \cdot \mathbf{n}_m) - \mathbf{n}_m$  is the direction of the magnetic field and  $\mathbf{e}_{r'}$ ,  $\mathbf{n}_m$  are unit vectors along directions  $\mathbf{r}'$  and  $\boldsymbol{\mu}$  respectively.

For a spherical particle, the magnetic moment is  $\mu = |\boldsymbol{\mu}| = B_r V / \mu_0$ , where  $V$  is its volume and  $B_r$  is its residual flux density. Thus, its magnetic field gradient is

$$(\nabla B_{\parallel}) \cdot \mathbf{u}_m = \frac{B_r a^3}{r'^4} f(\theta) \quad (4.18)$$

where

$$f(\theta, \phi)_{\text{gr}} = -(\mathbf{e}_r \cdot \mathbf{u}_m)(\mathbf{e}_B \cdot \mathbf{n}_s) + \frac{1}{3}(\mathbf{e}_\theta \cdot \mathbf{u}_m)\partial_\theta(\mathbf{e}_B \cdot \mathbf{n}_s) + \frac{1}{3\sin(\theta)}(\mathbf{e}_\phi \cdot \mathbf{u}_m)\partial_\phi(\mathbf{e}_B \cdot \mathbf{n}_s) \quad (4.19)$$

is a function that takes values of order 1. Using  $\partial_r \mathbf{e}_r = 0$ ,  $\partial_\theta \mathbf{e}_r = \mathbf{e}_\theta$ ,  $\partial_\phi \mathbf{e}_r = \sin(\theta)\mathbf{e}_\phi$ , we find

$$\begin{aligned} \frac{1}{3}\partial_\theta(\mathbf{e}_B \cdot \mathbf{n}_s) &= (\mathbf{e}_\theta \cdot \mathbf{n}_s)(\mathbf{e}_r \cdot \mathbf{u}_m) + (\mathbf{e}_r \cdot \mathbf{n}_s)(\mathbf{e}_\theta \cdot \mathbf{u}_m) \\ \frac{1}{3\sin(\theta)}\partial_\phi(\mathbf{e}_B \cdot \mathbf{n}_s) &= (\mathbf{e}_\phi \cdot \mathbf{n}_s)(\mathbf{e}_r \cdot \mathbf{u}_m) + (\mathbf{e}_r \cdot \mathbf{n}_s)(\mathbf{e}_\phi \cdot \mathbf{u}_m). \end{aligned}$$

Consequently,

$$\begin{aligned} f_{\text{gr}}(\theta, \phi) &= -(\mathbf{e}_r \cdot \mathbf{u}_m) [(3(\mathbf{e}_r \cdot \mathbf{n}_s)(\mathbf{e}_r \cdot \mathbf{n}_m) - (\mathbf{n}_m \cdot \mathbf{n}_s))] \\ &\quad + (\mathbf{e}_\theta \cdot \mathbf{u}_m) [(\mathbf{e}_\theta \cdot \mathbf{n}_s)(\mathbf{e}_r \cdot \mathbf{u}_m) + (\mathbf{e}_r \cdot \mathbf{n}_s)(\mathbf{e}_\theta \cdot \mathbf{u}_m)] \\ &\quad + (\mathbf{e}_\phi \cdot \mathbf{u}_m) [(\mathbf{e}_\phi \cdot \mathbf{n}_s)(\mathbf{e}_r \cdot \mathbf{u}_m) + (\mathbf{e}_r \cdot \mathbf{n}_s)(\mathbf{e}_\phi \cdot \mathbf{u}_m)]. \end{aligned} \quad (4.20)$$

For a dipolar field, the coupling is therefore

$$\lambda_s \sim \gamma_s \frac{B_r a^3}{r^{1/4}} x_{zP} \quad (4.21)$$

We define the function  $f_{dp}(\theta, \phi)$  for the dipolar coupling similarly to  $f_{gr}$ . Both functions are shown in figure 4.11.

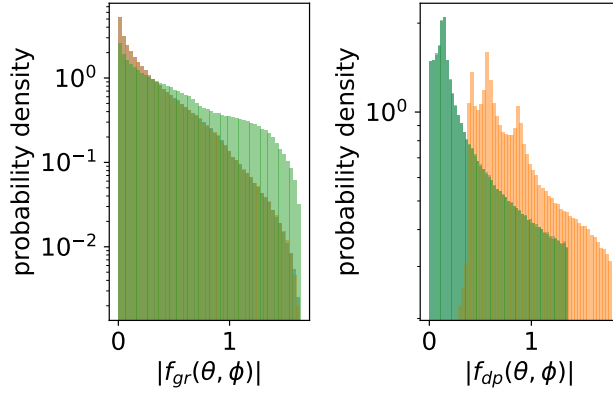


Figure 4.11: The angular functions  $f_{gr}(\theta, \phi)$  and  $f_{dp}(\theta, \phi)$  for uniform random angles of defining the directions  $\mathbf{e}_r$  and  $\mathbf{e}_m$ , while keeping  $\mathbf{e}_s$  fixed

## EXPERIMENTAL DEMONSTRATION OF PARTICLE-NV COUPLING

Next, we demonstrate coupling the motion of a levitated micromagnet to the electronic spin associated with an individual negatively charged NV-center. In our sample, NV-centers are hosted inside a diamond slab and implanted  $d_{impl} \sim 15$  nm below the diamond surface. The diamond replaces the glass slide of the previous experiment and is placed across the pocket that contains the magnet. The pocket is  $\sim 80\mu\text{m}$  deep and the magnet radius is  $a_3 = 15.1 \pm 0.1\mu\text{m}$ . We levitate the magnet  $z_{md} = 44 \pm 5\mu\text{m}$  below the diamond using the same method as before. The NV-center is located at

$(x_d, y_d) = (83, 29) \pm 5\mu\text{m}$  with respect to the magnet center such that the magnet-NV distance is  $|\mathbf{r}'| = \sqrt{(z_{md} + a_3)^2 + x_d^2 + y_d^2} = 99 \pm 5\mu\text{m}$ . The NV-center's electronic ground state has spin  $S = 1$  with the lower-energy  $|m_s = 0\rangle$  level separated from the  $|m_s = \pm 1\rangle$  levels by a zero-field splitting  $D_{zf}/(2\pi) \approx 2.87\text{ GHz}$  and its symmetry axes  $\mathbf{n}_s$  aligned along one of four crystallographic orientations set by the tetrahedral symmetry of the diamond lattice. A microwave (MW) signal at the transition frequency  $\omega_{\text{MW}}$ , drives the transition  $|m_s = 0\rangle \rightarrow |m_s = \pm 1\rangle$  which results in a decrease of the photoluminescence (PL) signal. The spin-dependent PL of the NV defect is due to a non-radiative intersystem crossing decay pathway, which also allows for efficient spin-polarization in the  $|m_s = 0\rangle$  spin sublevel through optical pumping<sup>75</sup>. The magnetic field dependent PL can therefore be used to optically detect magnetic fields<sup>76</sup>, which is used to sense the motion of the magnet (Fig. 4.13).

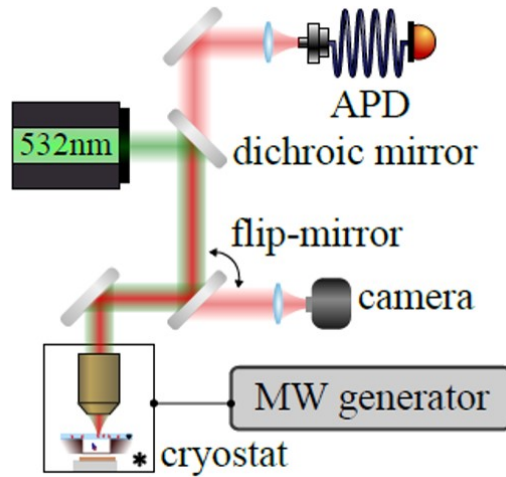


Figure 4.12: Schematic of the experiment for NV measurements.

Fig. 4.13b shows the optically detected magnetic resonance (ODMR) spectrum

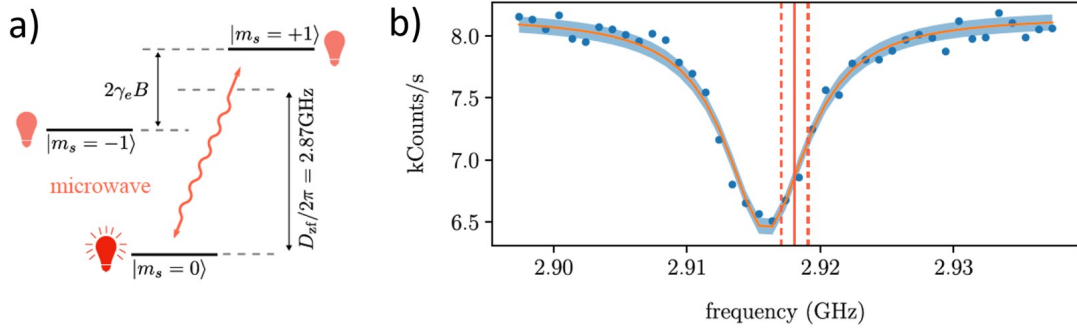


Figure 4.13: (a) Nitrogen-vacancy ground state spin levels. Resonant microwaves drive transitions between the  $m_s = 0$  and  $m_s = \pm 1$  states. The transition frequency depends on the magnetic field, which depends on the magnet-NV distance. The  $m_s = 0$  is brighter than the  $m_s = \pm 1$  states. Hence, for near-resonant MW driving, the fluorescence intensity depends on the magnet position. (b) ODMR spectrum. The magnet motion is measured by recording a timetrace of the fluorescence photons while applying a MW tone at the steepest slope of the transition (2.918 GHz) (solid red line). We measure the slope by frequency modulating the MW tone (red dashed lines).

of the NV-center with a fit to a Lorentzian corresponding to the  $|+1\rangle$  transition. The spectrum is measured with a home-built fluorescence microscope that we integrated with the cryostat (Fig. 4.12). In the presence of a microwave tone, the spin-mechanical coupling  $\lambda_g$  causes a variation in PL, since a displacement  $x$  of the magnet shifts the electron spin resonance by  $\delta\omega_{\text{NV}} = (\lambda_g/x_{\text{zpt}})x$ , where  $x_{\text{zpt}} = \sqrt{\hbar/2m\omega_x}$  is the zero point motion. To measure the magnet's motion with the NV, we excite one of its modes with a broadband fluctuating magnetic field, driving it into a quasi-thermal state and allowing us to observe it as a peak in the PSD of the NV PL counts (Fig.4.14c). We confirm that the peak is due to the moving magnet with the camera (Fig.4.14a). The camera and NV measurements are taken sequentially. Notably, we observe a small systematic frequency shift of  $\approx 1$  Hz between the NV and camera

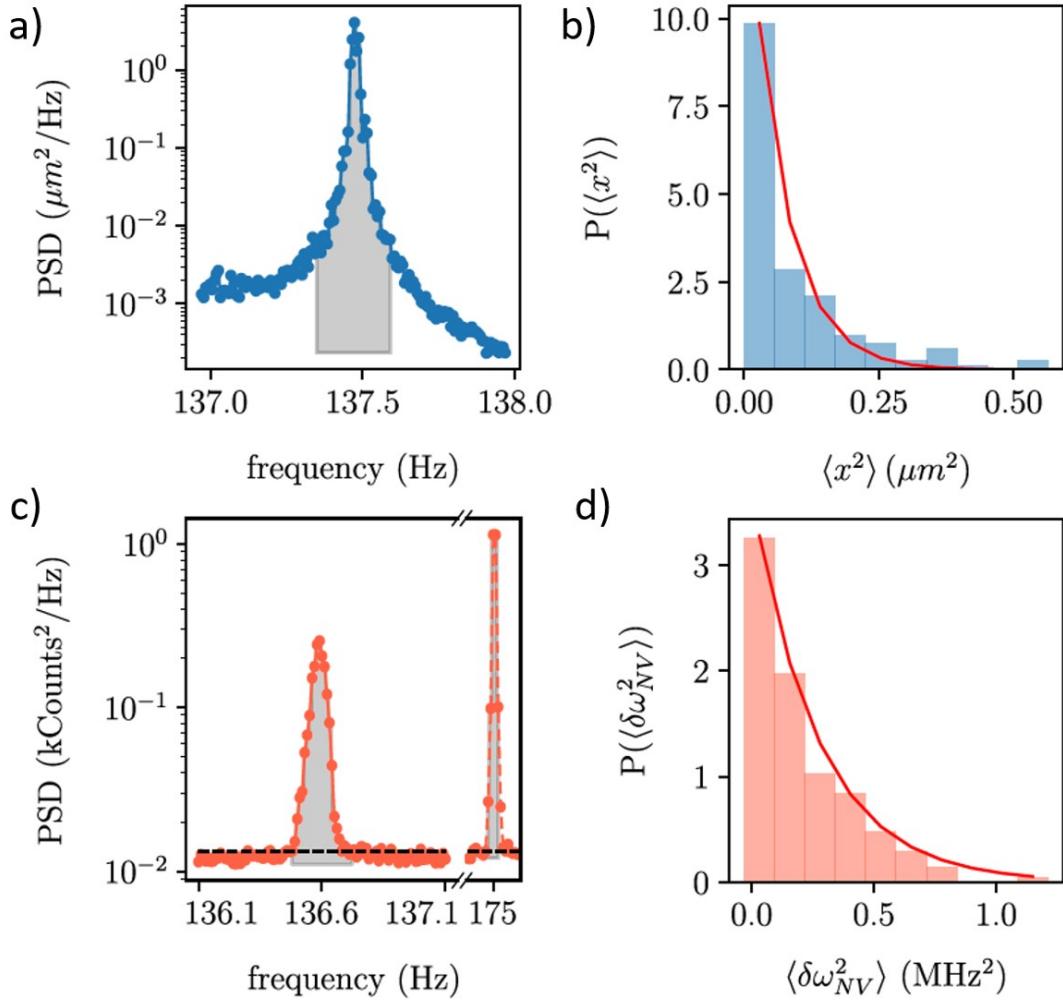


Figure 4.14: (a) Power spectral density of the video timetrace and (c) fluorescence timetrace. The gray area corresponds to the numerical integration of the variance  $\langle x^2 \rangle$ ,  $\langle c_{\text{NV}}^2 \rangle$  and  $\langle c_{\text{cal}}^2 \rangle$ . The second sharp peak is the calibration peak due to the MW frequency modulation. The black dashed line represents the photon shot noise. Histograms of the variances reveal the thermal character of the motional state during both the (b) camera and (d) NV measurement which we fit (red line) to extract the variances  $\langle x^2 \rangle$  and  $\langle \delta\omega_{\text{NV}}^2 \rangle$ , respectively.

measurements, which is likely due to the laser turned on during the NV measurement.

The mean spectral power in the NV peak is  $\langle c_{\text{NV}}^2 \rangle = s^2 \langle \delta\omega_{\text{NV}}^2 \rangle$ , where  $s$  is the slope of the ODMR signal at the microwave frequency, which we measure by applying a calibration tone to the microwave signal. The mean spectral power in the camera measurement,  $\langle x^2 \rangle$ , allows us then to extract the spin-mechanical coupling as  $\lambda_g = x_{\text{zP}} \sqrt{\langle \delta\omega_{\text{NV}}^2 \rangle / \langle x^2 \rangle}$ . To measure the coupling and confirm the thermal character of the driven mode, we consider the area under the PSD integrated over a time interval much shorter than  $1/\gamma$ , and construct its distribution over repeated measurements. For both the camera and the NV measurements, the distribution agrees with an exponential distribution  $P(E) = \beta_E \exp(-\beta_E E)$ , where  $\beta_E$  is the inverse of the variances  $\langle x^2 \rangle$  and  $\langle \delta\omega_{\text{NV}} \rangle$  (Fig. 4.14b,d). The resulting coupling strength is  $48 \pm 2\text{mHz}$ , in satisfactory agreement with the theoretical value for the gradient coupling to a dipole  $\lambda_g = \gamma_e \frac{\mu_0 \rho_\mu a^3}{r'^4} x_{\text{zP}} f_g(\theta) = 2\pi \times (18 \pm 3)\text{mHz} f_g(\theta)$  (Fig. 4.15b). Here  $f_g(\theta) \sim 1$  depends on the relative position and orientation of the NV-center and the magnet.

## DISCUSSION

We now discuss the prospects of using this system to achieve strong coupling. The minimal NV-magnet separation  $d_q^{\text{min}} = |\mathbf{r}'| - a$  is given by the NV implantation depth and the onset of strong attractive surface forces that will make the magnet stick to the diamond surface. Assuming that the frequency scales as  $\omega_j / 2\pi = c_f a^{-n}$ , the radius  $a = (n + 3)/(5 - n) d_q^{\text{min}}$  yields the maximum gradient coupling for a dipolar particle. A conservative gap  $d_q^{\text{min}} = 0.25\mu\text{m}$ ,  $c_f = 15\text{kHz } \mu\text{m}$ , corresponding to our observations in Fig.4.9, and  $n = 1$  for the dipole model, results in  $a = 0.25\mu\text{m}$  and

$\lambda_g/2\pi \sim 2.6\text{kHz}$  (Fig.4.15). Since the motional frequency can be reduced by adjusting the levitation height, one can even reach the elusive ultra-strong coupling regime  $\lambda_g > \omega_j$ <sup>77</sup>.

The cooperativity  $C = \lambda^2 Q \tilde{T}_2 \hbar / (2\pi k_B T) > 1$  marks the onset of coherent quantum effects in a coupled spin-phonon system. With a mechanical Q-factor of  $10^8$ , which has been demonstrated in levitated systems<sup>78</sup>, the coupling exceeds the thermal decoherence rate  $\Gamma_{\text{th}}/2\pi = k_B T / (2\pi \hbar Q) = 0.8\text{kHz}$  at  $T = 4\text{K}$ . NV-centers in bulk diamond, such as the sample used in our experiment, can have up to second long extended coherence times  $\tilde{T}_2$  at these temperatures using spin manipulation such as multi-pulse dynamical decoupling sequences limited only by pulse errors<sup>79,29</sup>. The minimum spin manipulation frequency in such sequences is typically a few kHz for bulk diamond NV-centers, which is within reach for the mechanical frequencies in our current geometry. Hence, this system can reach the high cooperativity ( $C > 1$ ) and even the strong coupling regime ( $\lambda > 2\pi/\tilde{T}_2, \Gamma_{\text{th}}$ ). Such a strong coupling enables ground-state cooling, quantum-by-quantum generation of arbitrary states of motion<sup>14</sup>, and spin-spin entanglement<sup>35</sup>.

Besides the translational degrees-of-freedom, levitated particles are free to rotate. For the hard magnets used in our experiment, the anisotropy energy strongly couples the particle orientation to the magnetization axis. The coupling leads to hybrid magneto-rotational modes, which correspond to a librational mode at frequency  $\omega_l = \sqrt{\omega_L \omega_I}$  that precesses around the local magnetic field  $\mathbf{B}_0$  at the Einstein-deHaas frequency  $\omega_I = \rho_\mu V_{\text{mag}} / (I_0 \gamma_0)$  due to the intrinsic spin angular momentum of the polarized electrons in the magnet. Here,  $\mathbf{B}_0$  is the sum of the field due to the sc and additional external fields and  $I_0 = 2\rho_m V_{\text{mag}} a^2 / 5$  is the moment of inertia,  $V_{\text{mag}}$  being the volume of the magnet and  $\rho_m$  ( $\rho_\mu$ ) its mass (spin) density. Since the Larmor fre-

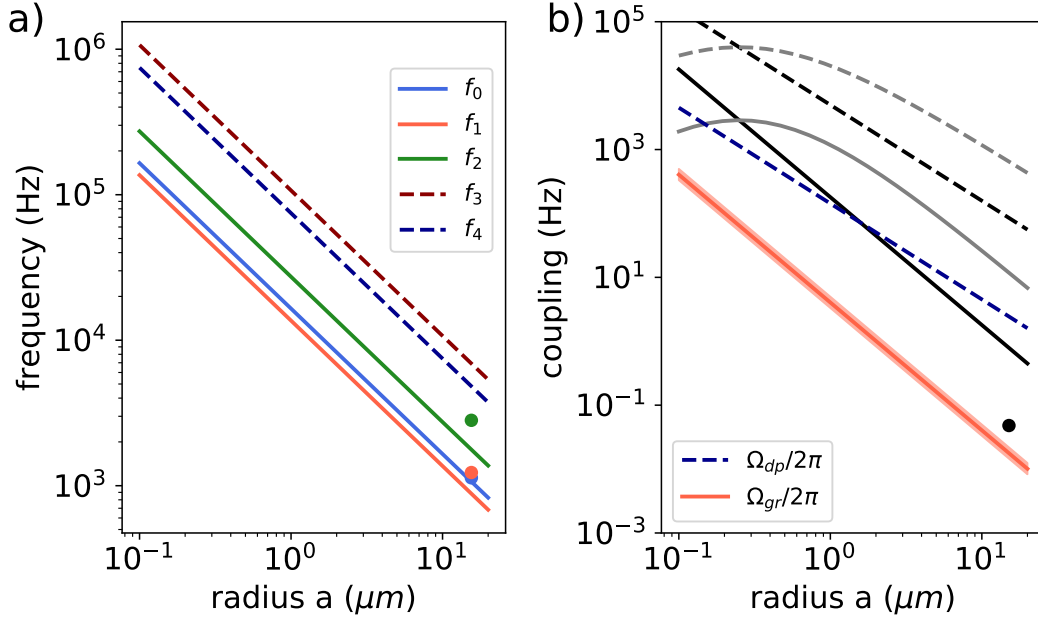


Figure 4.15: Future prospects for frequencies and couplings. (a) Mode frequency following dipole model<sup>65</sup> for  $h_{\text{lev}}/a = 3$ . The lowest (solid) lying modes correspond to the center-of-mass and the highest (dashed) lying modes to rotational motion. Data points are the experimental frequencies for particle 1 Fig.4.9d. MHz frequencies are predicted for sub- $\mu\text{m}$  particles. (b) Gradient (solid) and dipole-dipole (dashed) couplings, respectively. Straight lines show couplings for constant gap-particle size ratio  $\bar{d} = d/a = 5.5$  (color) and  $\bar{d} = 1$  (black). Curved lines (gray) show coupling for constant gap  $d = 250\text{nm}$  with a maximum coupling at  $a = d$ . The black data point is the experimental gradient coupling for particle 3.

quency  $\omega_L = \gamma_0 B_0$ ,  $\omega_l$  is higher than the translational mode frequencies even without additional fields and can be tuned with moderate magnetic fields  $\sim 10\text{mT}$  to MHz frequencies. The high frequencies of the librational modes make them inaccessible to our current detection based on video analysis and DC magnetometry. Future work will explore these modes using optical interferometry and SQUID<sup>9</sup> or NV-AC magnetom-

etry<sup>13,66</sup>. The rotational modes couple to the NV-center with a dipole-dipole coupling  $\lambda_{dp} = \gamma_e \mu_0 m_{zp} \frac{a^3}{r^3} f_{dp}(\theta)$ , where  $f_{dp}(\theta) \sim 1$  depends on the relative position and orientation of the NV-center and the magnet, and  $m_{zp} = \sqrt{\hbar \gamma_e \rho_\mu / 2V_{\text{mag}}}$  is the zero point magnetization of the Kittel magnon<sup>80</sup>. The weaker distance dependence yields  $\lambda_{dp} = 0.4\text{kHz}$  for a  $a = 5\mu\text{m}$  magnet at  $5\mu\text{m}$  distance from the NV-center (Fig.4.15b). This parameter regime is readily accessible with the experimental approach presented here, and it is sufficient to probabilistically cool the librational mode near its ground state<sup>81</sup>.

## OUTLOOK

These considerations indicate that our approach is a promising platform for quantum nanomechanics. Our experimental technique also allows us to achieve levitation with the superconductor in the Meissner state, and thus presents a path forward to observe precession due to the intrinsic spin angular momentum of the magnet with applications in highly sensitive magnetometry<sup>10</sup>. Since our mechanical resonator is all magnetic, we maximize the spin-to-mass ratio  $\rho_\mu / \sqrt{\rho_m}$  for a given magnetic material, which maximizes the spin-mechanical coupling. This leads to strong spin-mechanical coupling even for moderate experimental parameters. In addition, this system features libration modes, which are expected to reach an unprecedented spin-mechanical parameter regime even for magnets with  $a \sim 5\mu\text{m}$ . Magnets of this size can be levitated with the experimental technique introduced here.

Levitating submicron-particle still poses an experimental challenge. This is mainly due to surface forces, such as van-der-Waals and meniscus forces, which can make the particle stick to the nearby surface. While these issues will need to be carefully

investigated, a number of approaches can be used to address this challenge:

- surface treatments to reduce the surface forces, which extends the range of trappable particles
- exploiting the magnetic nature of the particles and using magnetic forces to pull the particle off the surface.
- pre-load the particle in another trap, e.g. a Paul trap, and transfer it to the superconducting trap

Even without these additional techniques, we recently levitated a magnet with radius  $a = 6\mu\text{m}$ . Hence, our current approach already allows us to carry out many exciting experiments. To achieve coupling larger than the motional frequency, one can engineer a low motional frequency by using a large levitation height while keeping the distance to the NV center small. This could be accomplished with an appropriate design of the levitation pocket or by designing the experiment such that the diamond (and thus the NV) can be moved independently.

Furthermore, the combination of high mechanical Q-factor, strong spin-mechanical coupling, and long spin-coherence is key for a range of applications such as magnetometers, accelerometers and gyroscopes<sup>9</sup>, where the magnet is the sensor which is read out through the NV-center<sup>13</sup>. It may enable the exploration of new phenomena, including dynamics between a levitated nanomagnet and a single flux vortex<sup>82,83,84</sup>, precession of a non-rotating magnet due to its intrinsic spin angular momentum<sup>85</sup>, preparation of non-Gaussian quantum states<sup>14</sup>, mechanically mediated quantum networks<sup>26,27</sup>, detection of dark matter<sup>10</sup>, and measuring the magnets internal degrees-of-freedom<sup>80</sup>.

# 5

## Conclusion and Outlook

Spin-mechanics hybrid systems represent an exciting class of platforms for metrology and quantum information. Successful creation of a high-cooperativity system could open the door to ultrasensitive magnetic field measurements, preparation of non-classical states of macroscopic objects, and a quantum bus for long-range spin-spin interactions. In this thesis, we demonstrated two platforms in which NV centers are coupled to different mechanical systems. These both represent promising steps

towards realizing such a system.

## 5.1 MAGNETICALLY FUNCTIONALIZED RESONATORS FOR STRONG NV-MECHANICS INTERACTIONS

In chapter 3, we demonstrated progress towards a high-cooperativity spin-mechanics hybrid system with an NV center coupled to a doubly clamped, magnetically functionalized silicon nitride resonator. We detailed three different fabrication methods for this system: evaporation of Cobalt magnets through low stress silicon nitride masks, manual placement of Nd-Pr-Fe-Co-Ti-Zr-B magnetic microparticles, and iron liftoff magnets with a  $\text{XeF}_2$  resonator release. Each of these systems were characterized (1) using a Mach-Zehnder interferometer to determine the mechanical quality factor and (2) using magnetic force microscopy and NV metrology to determine the resonator magnetization and expected gradient. It was found that the stencil-deposited samples had state-of-the-art quality factors at cryogenic temperatures ( $Q > 10^6$ ), but extremely poor magnetic field gradients. The microparticle samples correct this flaw, but are fragile and are not a scalable design. Finally, the iron liftoff samples have similar mechanical quality factors but also demonstrate the required magnetic fields. We lay out a path towards measuring the relevant gradient using an AC magnetometry sequence. With the current parameters and a high NV density diamond sample, we hope to cool the mechanical mode close to its ground state. Furthermore, by incorporating recent improvements in silicon nitride resonator design<sup>32</sup>, we anticipate improvements of up to three orders of magnitude in mechanical quality factor. Coupled with optimization of the gradient, this could enable the long term goal of two-qubit gates between NV centers and represent an exciting platform for quantum informa-

tion.

## 5.2 SINGLE-SPIN MAGNETOMECHANICS WITH LEVITATED MICROMAGNETS

In chapter 4, we proposed and demonstrated a new platform for strong coupling between an NV center and a micromagnet levitated above a YBCO superconductor. We detail the physics behind field-cooled superconductor magnetic levitation. We experimentally implement the system and measure quality factors  $Q > 10^6$  for KHz translational modes. The frequency can be tuned by varying the particle-superconductor distance as the superconductor passes the transition temperature, applying external DC magnetic fields, and changing the particle size. We then place an NV center nearby and detect the motion of the particle by measuring the change in magnetic field at the NV location, confirming the NV results match video results. From this, we extract a coupling of  $48 \pm 2\text{mHz}$ . This represents a critical step towards a high cooperativity spin-mechanics hybrid system. We expect that by reducing the particle diameter to  $.5 \mu\text{m}$ , we can achieve couplings of 2.6 kHz. Along with feasible increases in the mechanical quality factor to  $> 10^8$ , this platform has the potential to reach the cooperativity  $> 1$  regime, or even the strong or ultrastrong coupling regimes. This enables a wide range of exciting applications, such as sensitive magnetometers, preparation of non-Gaussian quantum states, and mechanically mediated quantum networks.



## Fabrication Procedures

In this appendix, I describe the fabrication of the devices discussed in the rest of the thesis. All fabrication was performed at the Harvard Center for Nanoscale Systems.

## A.1 DOUBLY CLAMPED RESONATOR DEVICE FABRICATION

Two different recipes are combined here, one for samples with stencils deposited magnets and a KOH release, and the second for liftoff magnets and a  $\text{XeF}_2$  release. In both, the cleaning, CPW fabrication, resonator definition, and sample packaging steps are identical.

The process uses a 4 inch, 525  $\mu\text{m}$  thick, high resistivity ( $> 10,000$  ohm-cm)  $\langle 100 \rangle$  silicon wafer obtained from Silicon Valley Microelectronics (SVMI). They perform LPCVD to deposit 150nm of high stress ( $\sim 1$  GPa) silicon nitride on one side. They also score the backside of the wafer in a 1cm square grid roughly 200 nm into the wafer, which keeps the integrity of the wafer during processing but allows easy cleaving and separation of individual devices at the end.

### A.1.1 CLEANING

We first clean the wafer before starting processing. This is done by sonicating the wafer for five minutes each in Acetone, Methanol, and IPA, then blow drying.

### A.1.2 COPLANAR WAVEGUIDE (CPW) FABRICATION

We fabricate a coplanar waveguide on the sample using liftoff to enable microwave delivery to the NV centers. This can be done for the full, unbroken wafer.

1. *Dehydration Bake* Bake the wafer at 180C for five minutes to remove any residual water and promote resist adhesion.
2. *Dynamic Clean* Place the wafer on the resist spinner and start a two step recipe (first step 500 rpm, second step  $\geq 3000$  rpm). During the first step, spray

acetone at the center of the wafer for a few seconds, then spray IPA until the spinner starts to ramp for the second step. Allow the second step to complete and dry the wafer.

3. *LOR Spin* LOR20B (MicroChem) resist at a speed of 4000 rpm for 45 seconds, then bake the wafer at 180°C for 4 minutes.
4. *S1805 Spin* S1805 (Microposit) resist at a speed of 4000 rpm for 45 seconds, then bake the wafer at 115°C for 1 minute.
5. *Exposure* The wafer is exposed on a maskless optical lithography tool (Heidelberg MLA 150), with a dose of 65 mJ/cm<sup>2</sup> at 405 nm. Note that this is an aligned write, as the pattern should be aligned to the pre-diced backside
6. *Development* The wafer is developed for 90 seconds in CD-26 (Microposit), then rinsed in water.
7. *Evaporation* We evaporate 7 nm titanium and 200 nm gold on the device using an e-beam evaporator (Denton).
8. *Liftoff* The wafer is placed in remover PG (MicroChem) heated to 80°C, and left overnight. If the liftoff does not complete, use a pipette to force liquid over the wafer and blow off any remaining metal.
9. *Final Cleaning* The wafer is sonicated in acetone, then IPA for 5 minutes each

### A.1.3 RESONATOR DEFINITION

In this step, we define the doubly clamped resonators in the silicon nitride. We now break the wafer into smaller groups of 1 cm x 1 cm chips, usually 2x2 for ease of

handling. Future steps are done using these smaller samples.

1. *Dehydration Bake* Bake the wafer at 180C for five minutes to remove any residual water and promote resist adhesion.
2. *Dynamic Clean* Place the wafer on the resist spinner and start a two step recipe (first step 500 rpm, second step  $\geq 3000$  rpm). During the first step, spray acetone at the center of the wafer for a few seconds, then spray IPA until the spinner starts to ramp for the second step. Allow the second step to complete and dry the wafer.
3. *ZEP Spin* ZEP520A (Zeon) resist at a speed of 3000 rpm for 45 seconds, then bake the wafer at 180° for 2 minutes. The resist should look uniform near the center of the chip.
4. *Exposure* The resonator pattern (each resonator is two 145  $\mu\text{m}$  x 4  $\mu\text{m}$  boxes separated by the resonator width of 1  $\mu\text{m}$ ) is exposed on a Raith 150 electron beam lithography system with a dose of 80  $\mu\text{C}/\text{cm}^2$
5. *Development* The wafer is developed in O-Xylene (Sigma-Aldrich, >99% pure) for 90 seconds, then rinsed in IPA for 30 seconds.
6. *Pattern Transfer* The pattern is transferred to the silicon nitride using an inductively coupled reactive ion etcher with a  $\text{C}_4\text{H}_8/\text{SF}_6$  chemistry. The etch runs for 2 minutes and 15 seconds, and etches through the nitride layer and 1  $\mu\text{m}$  into the silicon to maximize surface area for the later isotropic etch. Note that the ZEP layer is quite thin and the selectivity not incredibly high, so etching for any longer risks etching through the resist layer.

7. *Resist Stripping* Resist is removed by sonicating in acetone for 10 minutes, followed by 5 minutes in methanol then IPA.

The stencil/KOH procedure continues in A.1.4. The liftoff/XeF<sub>2</sub> procedure continues in A.1.6.

#### A.1.4 KOH RELEASE

The defined resonators are released using a KOH anisotropic silicon etch to remove the sacrificial layer underneath the resonators.

1. *Setup* Fill a large crystallization dish about 1/5 full of water. Place a medium crystallization dish inside this, also filled 1/5 full of water. Place a glass slide in the center of this dish, then place two small crystallization dishes with deionized water (DI) so they are tipped outwards.
2. *KOH Mixing* Fill a small mm crystallization dish with 20 mL DI, 4g KOH, and 400  $\mu$ L IPA. Place this into the 125 mm dish so it is also tipped outwards. Place a magnetic stirrer inside, then cover all five dishes with watch glasses.
3. *Heating* Place the dish assembly onto a hot plate and heat to 80C.
4. *Etching* Place the samples in the KOH dish and etch for 35 minutes.
5. *Cooling* Move the samples to one of the DI dishes for 5 minutes, and turn the hot plate off to allow the entire assembly to start to cool. Then move the samples to the other DI dish for 5 minutes.
6. *Drying* Dry the samples with nitrogen.

7. *Cleaning* Clean the released samples with a piranha clean (2:1 sulfuric acid:hydrogen peroxide).

#### A.1.5 STENCIL PLACEMENT AND EVAPORATION

The stencils can be fabricated using standard optical lithography and the KOH etch described above. The stencils then need to be aligned so the slit lines up with the center of the resonators, so that the magnet will be deposited in the proper location. This is accomplished using a commercial mask aligner (Suss MJB4).

1. *Setup* Attach the stencil in the 'mask' location using a vacuum chuck, and place the sample in the usual sample location
2. *Initial Alignment* Roughly align the stencil to the sample.
3. *Gluing* Carefully remove the stencil and use a stick to place a very small amount of UV curing glue on each of the four corners.
4. *Final Alignment* Place the stencil back into the aligner and perform a final alignment. Since we already performed an initial alignment, this should require only minimal movement of the sample and the glue shouldn't spread too much.
5. *Exposure* Perform a 600s flood exposure to cure the glue.
6. *Evaporation* Evaporate 3 nm Ti, 90 nm Co, and 7 nm Pt through the stencil onto the sample. item *Stencil Removal* Slide a tweezer between the sample and the stencil, and push upwards to 'flip' the stencil off.

All that remains is the packaging step, described in A.1.8.

### A.1.6 LIFTOFF MAGNET DEPOSITION

The liftoff fabrication procedure restarts here (from A.1.3). We fabricate chromium/iron/chromium trilayer magnets onto the center of the doubly clamped resonator using a liftoff process.

1. *Dehydration Bake* Bake the wafer at 180C for five minutes to remove any residual water and promote resist adhesion.
2. *Dynamic Clean* Place the wafer on the resist spinner and start a two step recipe (first step 500 rpm, second step  $\geq 3000$  rpm). During the first step, spray acetone at the center of the wafer for a few seconds, then spray IPA until the spinner starts to ramp for the second step. Allow the second step to complete and dry the wafer.
3. *MMA Spin* MMA EL-11 copolymer resist (MicroChem) at a speed of 5000 rpm for 45 seconds, then bake the wafer at 180° for 5 minutes. The resist should look uniform near the center of the chip.
4. *PMMA Spin* PMMA C-4 resist (MicroChem) at a speed of 5000 rpm for 45 seconds, then bake the wafer at 180° for 5 minutes.
5. *Exposure* The magnet pattern is exposed on a Raith 150 electron beam lithography system with a dose of 640  $\mu\text{C}/\text{cm}^2$
6. *Development* The wafer is developed in 1:3 MIBK-IPA for 90 seconds, then rinsed in IPA for 30 seconds.
7. *Separate Chips* The chips are separated into individual 1x1 cm samples by lightly pressing a tweezer on the top side above the cleave. Note that since

there is done while there is resist on the chips to avoid scratching the surface.

8. *Evaporation* We evaporate 8 nm Ti, 276 nm Cr, then 10 nm Ti, each at 1 Å/s, on the device using an e-beam evaporator (Sharon) with a pressure of  $<5 \times 10^7$  Torr. During the evaporation, the chips are placed next to a large permanent magnet to assist with sample magnetization. A thermometer can also be optionally placed next to the sample to ensure that the sample stays cool, which may lead to higher quality films.
9. *Liftoff* The wafer is placed in acetone and left overnight. If the liftoff does not complete, use a pipette to force liquid over the wafer and blow off any remaining metal.

#### A.1.7 RESONATOR RELEASE WITH XeF<sub>2</sub>

The resonators, now with magnets on them, undergo a release by etching the underlying sacrificial silicon layer using a Xactix e2™ system.

1. *Gas Settings* Set the gas mix to 2 Torr XeF<sub>2</sub> and 10 Torr N<sub>2</sub>. A high N<sub>2</sub> to XeF<sub>2</sub> ratio is used to keep the silicon nitride:silicon selectivity high.
2. *Pre-conditioning* Perform a pre-conditioning etch of 4 cycles.
3. *Sample Loading* Load the sample into the center of the etcher, using a drop of oil to secure it
4. *Etch* Etch for 4 cycles
5. *Completion Check* Check the result using an optical microscope or SEM. If the resonators look released, stop otherwise, repeatedly etch 1-2 additional cycles,

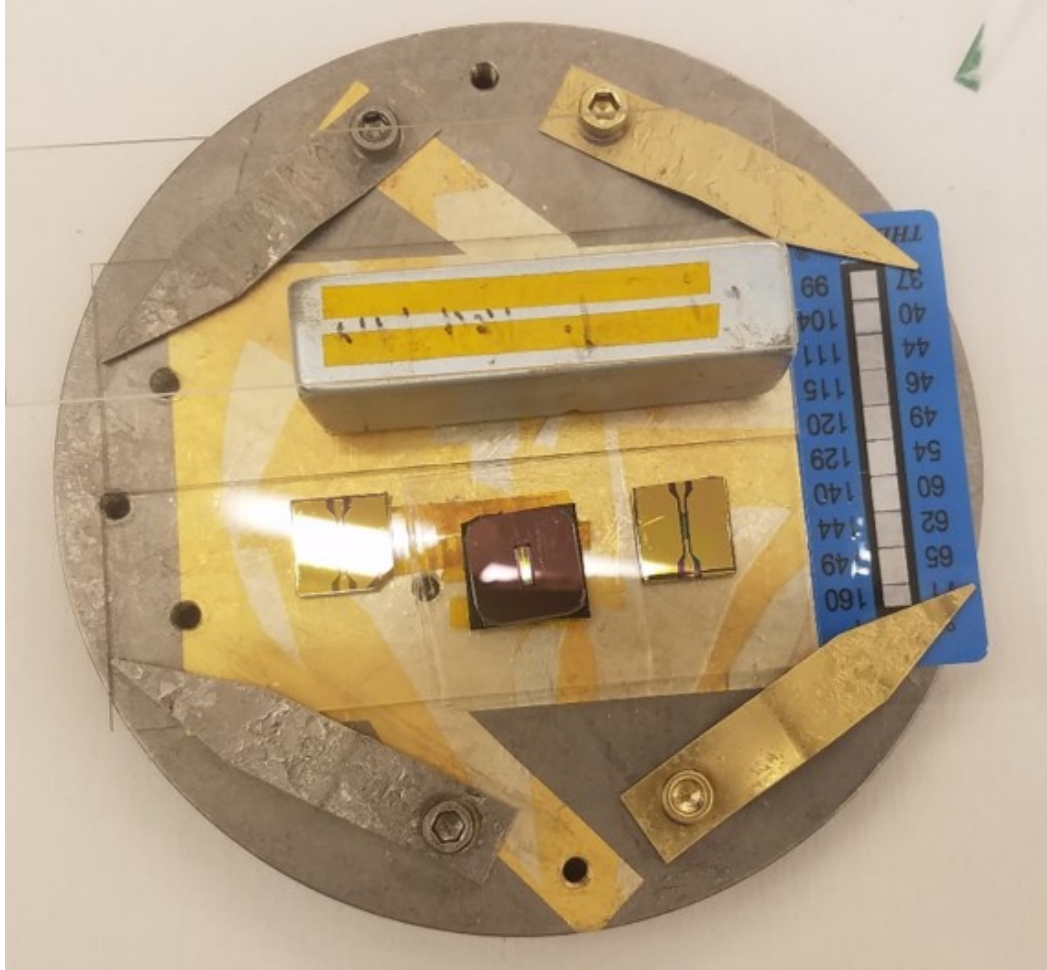


Figure A.1: Setup for e-beam evaporation of the magnetic layer. A magnet is placed near to the samples, with a glass slide affixed to the top to prevent deposition onto it. The samples are aligned so that the easy axis of the deposited magnets is aligned to the applied magnetic field. Optionally, a thermometer can be used to confirm that the temperature during evaporation stays low.

checking for completion each time. If any metal extended over the edge of the resonators and is attached to the silicon, it can be washed away by rinsing in IPA after a few cycles.

#### A.1.8 SAMPLE PACKAGING

The samples created using both procedures now finalized.

1. *Carrier* A 1x1cm fabricated sample is placed inside a carrier and secured with N-type vacuum grease
2. *Diamond Placement* A diamond is placed in top of the resonators in the center of the sample, NV side down, using a vacuum tweezer and secured with a small piece of crystal bond
3. *Wirebonding* The fabricated sample is wirebonded to the carrier. Use at least 3 bonds for each connection.

### A.2 MAGNETIC LEVITATION DEVICE FABRICATION

The process uses a 4 inch, 400  $\mu\text{m}$  thick, high resistivity ( $> 10,000$  ohm-cm)  $\langle 100 \rangle$  silicon wafer obtained from Silicon Valley Microelectronics (SVMI).

#### A.2.1 CLEANING

We first clean the wafer before starting processing. This is done by sonicating the wafer for five minutes each in Acetone, Methanol, and IPA, then blow drying.

### A.2.2 BACKSIDE THINNING

We now need to thin each pocket down from the backside, so that we can have small cooldown heights and magnetic particle can be still be brought very close (few  $\mu\text{m}$ ) from the diamond. We do this using a deep reactive ion etch.

1. *Dehydration Bake* Bake the wafer at 180C for five minutes to remove any residual water and promote resist adhesion.
2. *Dynamic Clean* Place the wafer on the resist spinner and start a two step recipe (first step 500 rpm, second step  $\geq 3000$  rpm). During the first step, spray acetone at the center of the wafer for a few seconds, then spray IPA until the spinner starts to ramp for the second step. Allow the second step to complete and dry the wafer.
3. *HMDS* Spin HMDS at 3000 rpm for 45 seconds, then bake at 115C for 1 minute
4. *SPR* Spin SPR-220-7.0 at 2000 rpm (without a 500 rpm first step) , then bake at 115C for 90 seconds.
5. *Exposure* The wafer is exposed on a maskless optical lithography tool (Heidelberg MLA 150), with a dose of  $950 \text{ mJ/cm}^2$  at 375 nm.
6. *Post-exposure hold and bake* Wait 90 minutes after exposure, then bake at 115C for 90 seconds
7. *Development* The wafer is developed for at least 100 seconds in CD-26 (Microposit), then rinsed in water. The boxes written are large should look clear by eye, if the resist has not yet been removed then develop for longer.

8. *Hard Bake* Hard bake the wafer at 115C for 7 minutes
9. *Wafer Mounting* Mount the wafer to an SiO<sub>2</sub> carrier using oil
10. *Deep Etch* Using a standard Bosch process recipe (12 second etch loops), etch 75 loops into the wafer. The etch rate can vary between 3-3.6  $\mu\text{m}$  per loop, so this should etch through approximately 250  $\mu\text{m}$ . Measure the average per pulse etch rate using an optical microscope and focusing on the top and bottom of the etched areas, then use this to calibrate the number of additional pulses necessary to etch to 360  $\mu\text{m}$  into the wafer.
11. *Cleaning* Submerge the carrier with attached wafer in Microposit 1165 overnight to dissolve the oil and detach the sample. Use subsequent baths of 1165, acetone, and IPA to remove all of the resist, then dry

### A.2.3 SILICON NITRIDE LAYER DEPOSITION

We now deposit a thin layer of nitride on the backside to form the bottom membrane of the pocket.

1. *Silicon nitride deposition* Deposit 600 nm of low temperature, low stress silicon nitride on the just-etched side of the wafer using an Oxford Plasmapro 100 ICP-CVD

### A.2.4 COPLANAR WAVEGUIDE (CPW) FABRICATION

The wafer is flipped, and a coplanar waveguide is fabricated on the top side for each thinned area using the same recipe as in A.1.2.

### A.2.5 POCKET FABRICATION

We now etch the pockets for the magnetic particles from the top side down to the silicon nitride layer. The fabrication is identical to the process described above in A.2.2, with the exception that the etch is done for just 11-14 loops to etch down the last 40  $\mu\text{m}$ . The last few loops should be done in 1-2 loops at a time to prevent etching through the nitride layer in each pocket, as the nitride etches slowly but at a non-zero rate. The wafer will break apart into individual samples when the topside etch is completed. The carrier can be placed on a hotplate, then each sample can be removed individually from the carrier using tweezers before performing the same clean as described above.

### A.2.6 ANGLED WALLS

The above section describes the pockets created with vertical sidewalls, used in experiments with an integrated diamond. For the initial mechanics experiments, we instead fabricated devices with angled walls. In this case, we start with with a 525 m thick  $\langle 100 \rangle$  silicon wafer, with 400 nm of super low ( $< 100$  MPa tensile) stress silicon nitride on both sides from SVMIL. The procedure is then:

1. *Dehydration Bake* Bake the wafer at 180C for five minutes to remove any residual water and promote resist adhesion.
2. *Dynamic Clean* Place the wafer on the resist spinner and start a two step recipe (first step 500 rpm, second step  $\geq 3000$  rpm). During the first step, spray acetone at the center of the wafer for a few seconds, then spray IPA until the spinner starts to ramp for the second step. Allow the second step to complete

and dry the wafer.

3. *HDMS Spin* HMDS at 4000 rpm for 45 seconds, then bake at 115C for 1 minute
4. *S1813 Spin* S1813 at 4000 rpm for 45 seconds, then bake at 115C for 1 minute.
5. *Repeat* Repeat this procedure on the other side of the wafer. The resist on the backside is just for protection, only the frontside will be used for processing.
6. *Exposure* The wafer is exposed on a maskless optical lithography tool (Heidelberg MLA 150), with a dose of 100 mJ/cm<sup>2</sup> at 405 nm. This writes the pocket pattern to the wafer.
7. *Development* The wafer is developed for at 60 seconds in CD-26 (Microposit), then rinsed in water.
8. *Pattern Transfer* The pattern is transferred to the silicon nitride using an inductively coupled reactive ion etcher with a C<sub>4</sub>H<sub>8</sub>/SF<sub>6</sub> chemistry. The etch runs for 4 minutes and 30 seconds, and etches through the nitride layer.
9. *Resist Stripping* Resist is removed by placing the wafer in heated Remover PG for >1 hour, followed by 5 minutes in acetone, then methanol, then IPA.
10. *Pocket Etching* The pockets are etched by using the KOH release recipe described in A.1.4. For a full wafer, we used 30 mL DI, 6g KOH, and 600  $\mu$ L IPA, then etched for 4 hours or until the etch looks complete by eye (the membranes at the bottom will be translucent).

The individual chips should be easily separated after the etch and are ready to use.

# B

## Additional Details of Levitation

### Experiment

#### B.1 EXPERIMENTAL DETAILS

In this section we provide additional information that helps to reproduce the experiment.

### B.1.1 SAMPLE FABRICATION

The sample fabrication consists of three main steps: Fabrication of the micro-pockets, loading the magnet and adding the cover and magnetizing the magnet.

#### FABRICATION OF POCKETS

The pocket fabrication is detailed in A.2.

#### LOADING MAGNETS AND ADDING COVER

Magnets are loaded using a home built microscope setup. The empty pocket device is mounted on an iron (and slightly magnetized) mount. A small quantity of unmagnetized particles are placed on a clean surface, and the microscope is used to identify one of the required size. A sharp tungsten tip (Omniprobe) mounted to a piezo stage is then touched to the particle to pick it up, and to place it into the bottom of the pocket. This is repeated to place multiple particles. Once the process is complete, either a thin glass slide (mechanics measurements) or a diamond (NV measurements) is placed over the pockets and secured with Crystalbond 555 (EMS) to keep the particles contained.

#### WIREBONDING AND MAGNETIZATION

Once the particles have been loaded, we wirebond (Dicing Systems model 4523) the chip to a custom printed circuit board (PCB). Finally, we magnetize the sample. We first place the entire sample in a strong superconducting magnet while the magnet is off. We then increase the magnetic field to 4 Tesla at a rate of .27 Tesla/min, and ramp down to zero Tesla at the same rate.

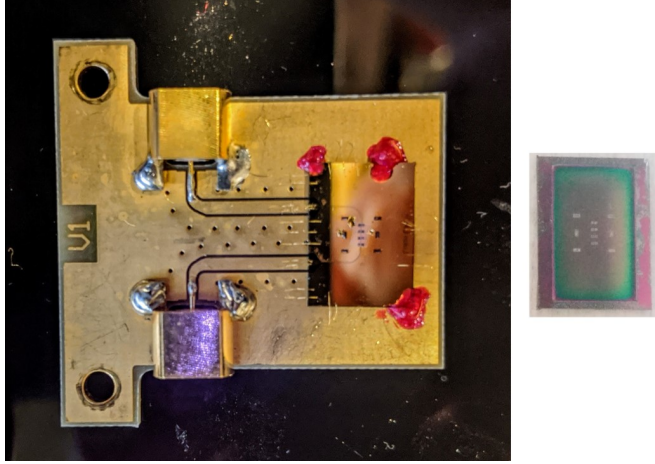


Figure B.1: Device after full preparation. The microfabricated sample is affixed to the PCB with nail polish (Maybelline, Crushed Candy) before wirebonding. Diamond is affixed over pockets using crystal bond. The image at right shows the backside of the completed fabricated device, with the center inset etched down to reduce the pocket depth and the unetched area forming an outer frame to allow easy handling.

### B.1.2 LEVITATION PROCEDURE

To load the magnet into the trap, we start with individual magnets that have been placed in silicon pockets. The bottom of the pockets consists of a thin silicon-nitride membrane and the top holds a thin and transparent glass slide or a diamond. At the beginning of the experiment the magnet rests on the membrane at a distance  $h_{\text{cool}}$  above the superconductor (SC). The SC is mounted on a piezo stepper and is thermally linked to the cold-finger of the cryostat. When the temperature of the SC is well below  $T_c$ , we approach the magnet with the SC. As the magnet comes closer, the induced currents in the superconductor increase to preserve the magnetic field configuration that is present during cooldown. Once the magnetic forces from the induced currents overcome the surface forces between the magnet and the membrane,

the magnet lifts off the membrane and levitates at  $\mathbf{r}_{\text{mag}} = (0, 0, h_{\text{lev}})$  where the levitation height  $h_{\text{lev}} \approx h_{\text{cool}}$ . For small displacements from the equilibrium position  $\mathbf{r}_{\text{mag}}$ , the magnet undergoes harmonic motion at frequencies  $\omega_i$  ( $i = x, y, z$ ).

### B.1.3 CAMERA ACQUISITION

For the mechanical property measurements, we use a long working distance objective (10X Mitutoyo Plan Apo Infinity Corrected Long WD Objective with a depth of focus of  $3.5 \mu\text{m}$ ) that is mounted outside the cryostat. We illuminate the sample with  $\sim 68 \mu\text{W}$  red LED light at the back of the objective and the entire particle is imaged onto a fast camera (Phantom Miro C110 camera) at frame rates up to 4600 FPS. For each frame, we fit the shape of the particle to an ellipse with opencv (<https://opencv.org/>). The center of the ellipse in each frame gives us the particle position timetrace  $x_c(t)$ ,  $y_c(t)$ . Alternatively, we track the center position of the bright spot at the center of the bead. This allows us to reduce the image size and increase the frame rate up to 12000 FPS. In practice, the two methods give the same result.

For the NV-measurement, we perform measurements with a high NA objective (100x Nikon CFI60 TU Plan Epi ELWD Infinity Corrected objective with a depth of focus of  $0.43 \mu\text{m}$ ). The particle is illuminated with a red LED at  $\sim 2.2 \mu\text{W}$ . With the high NA, the reduced field of view and depth of field don't allow observation of the entire particle. However, we still clearly see the central bright reflection, which for the measurements shown in Fig. 3 of the main text are recorded at 300 FPS. The frames are then thresholded by pixel intensity to distinguish between the reflection and the dark background. By taking the center-of-mass of the pixels above threshold for each of these frames, we extract the position of the bead  $(x_c(t), y_c(t))$  over time.

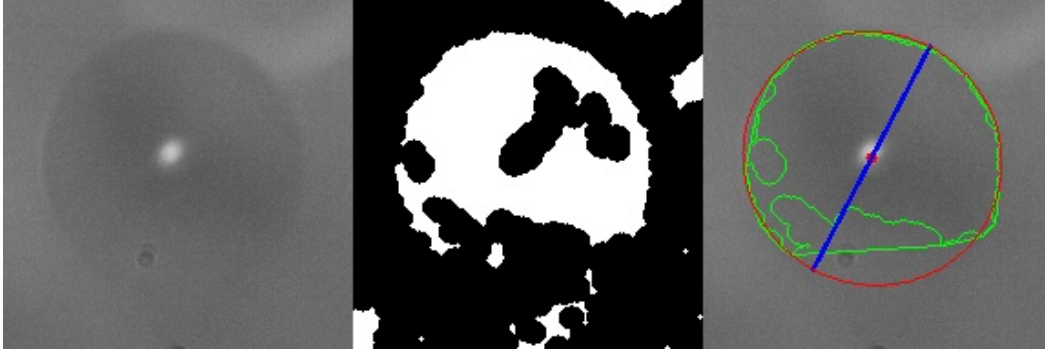


Figure B.2: Left: a single frame from a video of the particle. The white shape in the center is the reflection of the red LED off of the particle. Middle: the same frame after applying thresholding. Right: the particle fit to an ellipse after thresholding. The red dot in the center is the calculated position, and the blue bar denotes particle orientation.

#### B.1.4 DETERMINATION OF THE LEVITATION HEIGHT

The levitation height is determined optically using the microscope setup.

The objective is mounted on a translation stage, and it is moved to focus in turn on the superconductor and the top of the particle. The distance between these two objective positions denotes the levitation height plus the radius of the magnet, the latter of which is independently determined from calibrated microscope images.

#### B.1.5 CALIBRATION OF PARTICLE SIZE

We determine the particle radius from optical images that we acquire with the camera that is integrated into our setup. The optical image is calibrated with the width of the microwave stripline, which is fabricated to be  $40 \mu\text{m}$  and imaged with the same camera.

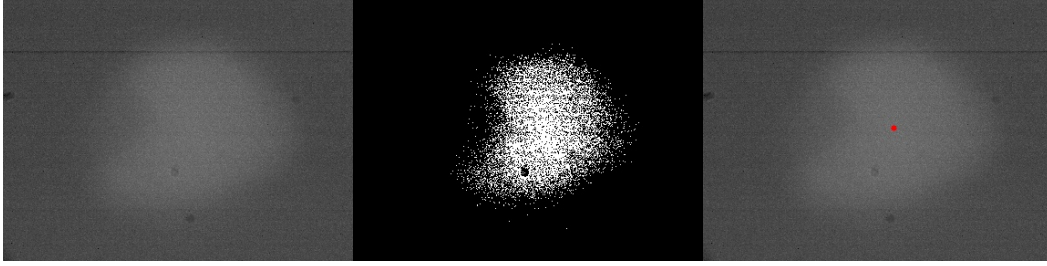


Figure B.3: Left: a single frame from a video of the particle. The white shape is the reflection of the red LED off of the particle. Middle: the same frame after thresholding. Right: the red dot is the average position weighted by pixel intensity after thresholding.

### B.1.6 GAS DAMPING

Gas damping due to residual molecules is a main source of decoherence. Therefore, the experiment has to be performed at high vacuum conditions to eliminate gas damping. Following Beresnev, the viscous damping from a dilute gas is given by<sup>86</sup>

$$\frac{\gamma_{\text{gas}}}{2\pi} = 3\eta \frac{a}{m} \frac{0.619}{0.619 + \text{Kn}} (1 + c_K), \quad (\text{B.1})$$

where  $c_K = 0.31\text{Kn} / (0.785 + 1.152\text{Kn} + \text{Kn}^2)$ ,  $\text{Kn} = \bar{l}/a$  is the Knudsen number for the free mean path  $\bar{l} = k_{\text{B}}T_{\text{gas}} / (\sqrt{2}\sigma_{\text{gas}}P_{\text{gas}})$ , and  $\sigma_{\text{gas}} = \pi d_{\text{m}}^2$ ,  $d_{\text{m}} = 0.372 \text{ nm}$  is the size of the air molecules and  $m_{\text{gas}}$  the mass. In high vacuum the damping depends linearly on the gas pressure and one finds the linearized expression

$$\frac{\gamma_{\text{gas}}}{2\pi} = 0.354 \sqrt{\frac{m_{\text{gas}}}{k_{\text{B}}T_{\text{gas}}}} \frac{P_{\text{gas}}}{a\rho} \quad (\text{B.2})$$

Figure B.5 shows the damping and Q-factors for a spherical magnetic particle with radius  $15\mu\text{m}$ . As indicated by the vertical grey area, the expected Q-factor from pure

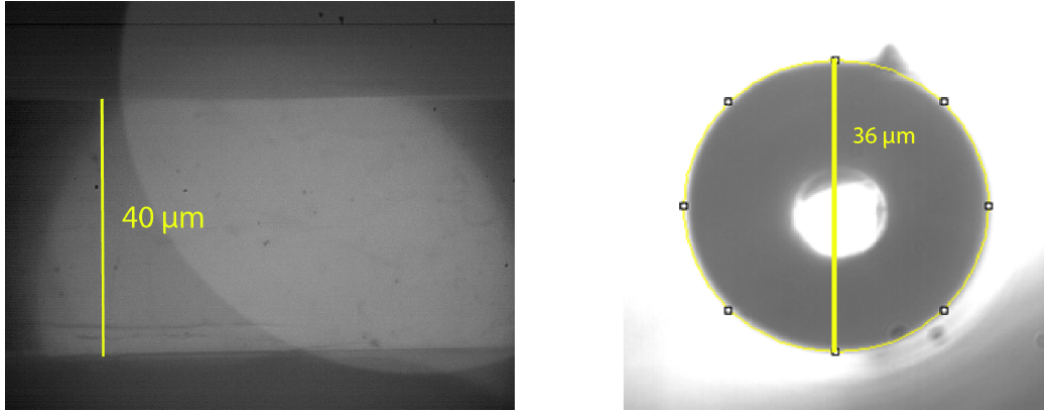


Figure B.4: Left: An image of the microwave stripline, used to calibrate the images of the particle. Right: An example image of a particle. The yellow outline of the bead is fit to a circle to determine the radius. The software used was ImageJ.

gas damping would be much larger than  $10^6$  for the pressures in the experiment, which we estimate to be at most  $10^{-5}$  mBar.

## B.2 MATERIAL PROPERTIES

### B.2.1 YBCO

For the frequency and Q-factor measurements we use 200nm thick YBCO films on  $\text{Al}_2\text{O}_3$  from Star electronics ([www.starcryo.com](http://www.starcryo.com)). Due to their strong fluorescence, for the NV-measurements we changed the sc sample to a 500nm thick YBCO films on  $\text{Al}_2\text{O}_3$  from MTI ([www.mtixtl.com](http://www.mtixtl.com)) with specified  $J_c = 2 - 3 \text{ MA/cm}^2$  at (77K, 0T) and  $T_c = 90\text{K}$ .

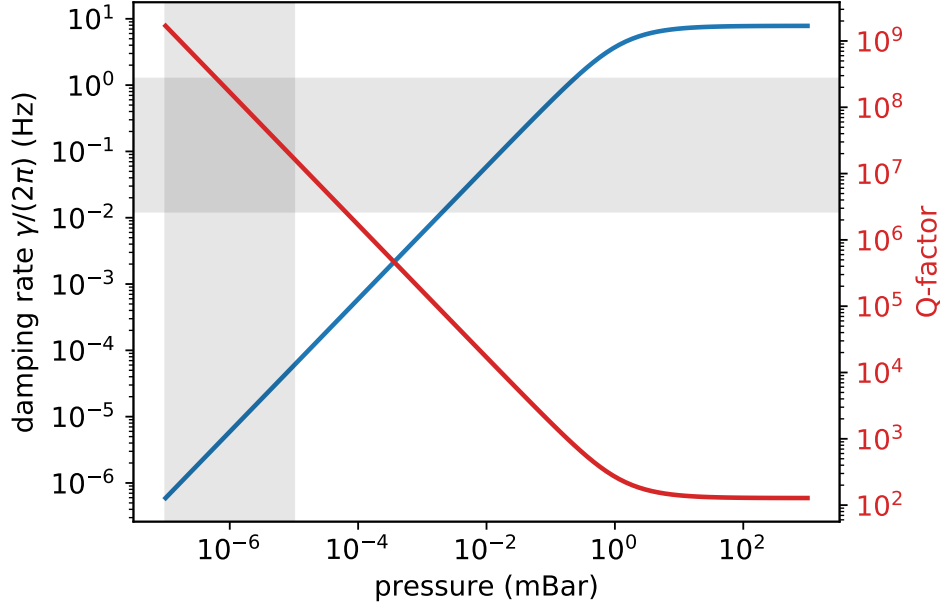


Figure B.5: Gas damping for a  $a = 15\mu\text{m}$  magnet at  $T_{\text{gas}} = 10\text{K}$ . The vertical shaded grey area shows the experimental range of pressures, with the most conservative estimate  $10^{-5}\text{mBar}$  and the vertical shaded grey area shows the corresponding damping rates and Q-factors.

## B.2.2 MAGNET

The magnetic particles are picked from *MQP-S-11-9-20001-070 Isotropic Powder* from [www.magnequench.com](http://www.magnequench.com), which is based on a Nd-Pr-Fe-Co-Ti-Zr-B alloy. The manufacturer specified residual induction is  $B_r = 730 - 760\text{ mT}$ , the energy product  $(BH)_{\text{max}} = 80 - 92\text{ kJ/m}^3$ , the intrinsic coercivity  $H_{ci} = 670 - 750\text{ kA/m}$ , the Curie temperature  $T_{\text{Curie}} = 320^\circ\text{C}$ , and density  $= 7430\text{ kg/m}^3$ .

### B.2.3 DIAMOND

The experiments were performed using electronic grade diamonds grown by Element Six with a natural isotopic abundance of carbon. The diamonds were then cut and polished to a thickness of 40 $\mu\text{m}$ . NV centers are generated by irradiating the sample with Nitrogen 15 ions at 6 KeV energy with a dose of  $2 \times 10^9 / \text{cm}^2$ , which is done at the Innovion commercial foundry (<https://www.innovioncorp.com/>). This is followed by an anneal at  $800^\circ\text{C}$ . Previous results have shown that these implantation energies result in an approximate NV depth of  $15 \pm 10 \text{ nm}$ <sup>87</sup>.



# pylabcontrol: a platform for scientific experiment control

## C.1 INTRODUCTION

A core component of modern physics experiments is laboratory control software, which controls and coordinates experimental equipment, collects data, and performs

initial analysis. However, it is usually considered a low priority that takes time away from the core scientific objectives of the lab, and thus has minimal resources dedicated to it. This is exacerbated in academic settings by the high turnover of students. Many experiments will be run on Labview or Matlab code created by long-graduated students, then added to by subsequent ones in ad-hoc ways as new requirements arise. The result is often a Frankenstein’s monster of poorly planned, poorly documented, fragile, and buggy code that slowly sucks additional resources to remain in a usable state. In addition, there tends to be minimal code reuse in or between labs, even when researchers are using the same equipment to perform similar experiments.

pylabcontrol seeks to solve these issues by providing a powerful, generic platform for laboratory control for any field. It defines an interface for controlling experimental *instruments*, and combining them together into complex *scripts*, which can be further combined to run complex experiments. A PyQT5<sup>88,89</sup> GUI allows real time visualization and manipulation of results. Data acquisition, storage, and retrieval are standardized. It utilizes git for version control, is well documented, and has been distributed under the GPLv3 license. This core code has been used in labs throughout Harvard, and a robust version of the code has been released on the python package index (pypi) for easy installation.

On top of this generic framework, users can create pluggable *toolkits*, which provide the specific instruments and scripts that they need to carry out experiments in their field of choice. Since the elements of every toolkit implement the same interface, individual instruments and scripts, or even full toolkits, can be easily shared between labs to maximize efficiency. Here, we’ll specifically discuss the *b26\_toolkit* developed for quantum optics experiments and used for those reported in this thesis.

### C.1.1 CHOOSING PYTHON

pylabcontrol is implemented in Python 3, which has become an extremely popular choice for scientific programming. A high level language, python has a low barrier to entry, is human readable, and is concise, making it a great fit for a platform intended for researchers who may not have deep programming or computer science expertise. pylabcontrol also can leverage the wide variety of scientific packages already available via Anaconda<sup>90</sup> and the python package index<sup>91</sup>, such as SciPy<sup>92</sup> and NumPy<sup>93</sup>, to maximize researcher productivity. Since python use is becoming widespread, most hardware vendors are providing python code. And for those that don't, packages such as ctypes<sup>94</sup>, Python for .NET<sup>95</sup>, and pyserial<sup>96</sup> allow interfacing with instruments via C dlls, .NET dlls from C# and other languages, and serial connections respectively, among many other connection available connection protocols. The same code can be used for real time analysis during the experiment, and then called afterwards in a Jupyter notebook for a more detailed look at the data. The main disadvantage of choosing python would be the slow code execution of a scripting language, but in the author's experience most experiments are hardware timed to be precise down to tens of nanoseconds or otherwise limited by communication times rather than code execution times. If necessary, any critical codepaths can be written and optimized in C/C++ then called from pylabcontrol.

### C.2 MODERN QUANTUM OPTICS LABORATORY CONTROL SOFTWARE

Several other generic laboratory control platforms used mostly for quantum optics experiments have been developed either just before or concurrently with pylabcontrol. The most popular ones known to the author are labRAD<sup>97</sup> and Qudi<sup>98</sup>. LabRAD

uses a client-server architecture, while Qudi has a central manager to handle separate experimental modules. Both have advantages and support some features currently lacking in pylabcontrol, such as running a single experiment across multiple computers. However, they also have higher complexity, both in terms of initial setup and learning curve, and the overhead and burden of knowledge required to implement new features or experiments. pylabcontrol is extremely simple to use, has a simple and well documented core module, and can be installed and running in just a few minutes. There are also a large number of bespoke systems, such as pi3diamond<sup>99</sup>, created and optimized for a single lab's experiments. pylabcontrol's fully generic core package can be shared across labs and fields, vastly reducing overhead, driving code sharing, and allowing researchers to concentrate on the science rather than maintaining their own software package.

### C.3 PYLABCONTROL CORE

pylabcontrol is split into a 'core' package, which provides the core framework and structure, and toolkits that plug into this core package to implement the experiments for a specific application. This section will describe the structure and main components of this core package.

#### C.3.1 STRUCTURE

pylabcontrol consists of three main hierarchical components:

1. *Instruments* Instruments are software objects, each of which corresponds to a single physical piece of hardware. They include logic to initialize and commu-

nicate with the hardware, and maintain an internal state with settings for that instrument.

2. *Scripts* Scripts are software objects that bundle together zero or more instruments into a modular chunk of an experiment. They include the logic for which instruments should receive what commands at what time, and process, save, and perform initial analysis on the data. Scripts can also be *nested* so that they contain other scripts, building up progressively more complicated experiments from these chunks.
3. *GUI* Scripts can be loaded into a fully functional and customizable GUI, which allows researchers to set the experimental parameters and see the results in real time.

### C.3.2 INSTRUMENTS

All instruments inherit directly from the *Instrument* class, logically an abstract class which provides an interface and basic functionality for hardware devices. The interface for *Instrument* is displayed in figure 1. Each of these fields or functions are described below and must be implemented by the user.

#### INTERFACE

1. *settings* Each instrument contains a settings dictionary. This stores the state of the instrument as *Parameters*, mapping a property of the instrument to its value. *Parameter* inherits from python's *dict* and acts as a key value pair with three additional fields, *valid\_values*, *info*, and *visible*. The first defines valid values for the value, which can either be a list (such as a list of valid ports) or

```

class Instrument(object):
    _DEFAULT_SETTINGS = ...
    # Dictionary containing the state of the instrument
    _PROBES = ...
    # List of values that can be read off of the hardware
    def __init__(self, name=None, settings=None):
        # Initialize the instrument, including connecting to the
        # device
    def update(self, settings):
        # Define how changes to settings should be propagated to
        # the hardware
    def read_probes(self, key = None):
        # Define how values should be read out from the hardware

```

Listing 1: Interface for the Instrument Class

a python type. If a Parameter value is set to a non-allowed value, an error is thrown. This prevents, for example, a voltage being set to a string, which might then be sent on to the physical instrument and either cause it to enter an error state or, worse, cause dangerous undefined behavior. The second is a text field that gives additional information on the key-value pair, allowing users a better explanation of the purpose for a given Parameter. The third is an internal flag on whether a Parameter should be user editable or fixed, and thus whether to display it in a GUI. Standard parameters can be accessed via the dot operator, for example `instrument.param`. Parameters can also be nested, so for example a point parameter might contain two sub-parameters, x and y coordinates. This allows Parameters to be a powerful, flexible tool.

2. *update* The instrument defines an update function, which allows the hardware dictionary to be updated. The default implementation will update all internal

settings. However, this can be extended by the user to update settings on the physical device. If an setting on a device is updated in software, this function can ensure the change is automatically propagated to the hardware.

3. `__connect()` and `__init__(name=None, settings=None)` The instrument contains a connection function `__connect` and an initialization function `__init__`. `__connect` defines how the computer can use the desired communication protocol to connect to the hardware, and it will be called by `__init__` to initialize the hardware to the state given by either the input or the default *settings* dictionary.
4. *Probes* An instrument contains a (possibly empty) set of Probes, which is a list of values that can be read off from the hardware, as well as an accompanying function to perform that read.

## BUILT-IN FUNCTIONALITY

Though most behavior is specific to the requirements of a given device, some functionality is provided by default. Instrument contains a loading function, which handles instrument instantiation, loading, error handling, and integration into Scripts. All Instruments can also be saved to disk, allowing documentation and the instrument with a snapshot of the current settings for lab notes or reloading for future experiments, as well as a dictionary representation of the instrument to assist with debugging.

```

class Script(QObject):
    _DEFAULT_SETTINGS = ...
    _INSTRUMENTS = {...}
    _SCRIPTS = {...}
    def __init__(name=None, settings=None, instruments=None,
scripts=None, log_function=None, data_path=None):
        # Initialize the script as necessary.
    def _function():
        # The core of the Script. This is executed when the script
        # is run.
    def _plot(axes_list, data = None):
        # Plot a script for the first time, preparing the figure,
        # axes labels, etc as necessary
    def _update_plot(axes_list):
        # Update the data in a plot first created with _plot

```

Listing 2: Interface for the Script Class

### C.3.3 SCRIPTS

All scripts inherit either directly from the *Script* class, logically an abstract class which provides an interface and basic functionality for the scripts, or from another *Script* class. The interface for Script is displayed in figure 2. Each of these fields or functions are described below and must be implemented by the user.

#### INTERFACE

1. *settings* Like Instruments, Scripts contain a *settings* dictionary of Parameters that stores the state of the script and the settings that it will use when it is run. This contains at minimum a path to where data should be saved and a descriptive tag to use when saving that data.

2. *Instruments* and *Scripts* A list of instruments and subscripts the Script will use during execution. Because instruments and subscripts are fully abstracted, those that expose the same API can be easily switched out if, for example, a device is upgraded to a different model.
3. *function()* This is the function defining the experimental logic for the script that will be executed when the script is run.
4. *\_\_plot(axes)* and *\_\_update\_plot(axes)* Optional functions that defines how data should be plotted when the script is run. *\_\_plot* defines how the data is plotted the first time, and is thus responsible for setting up the figure and axes, while *\_\_update\_plot* handles subsequent plot updates and therefore can reduce rendering overheads if necessary for fast visualization. It assumes a canvas is available, such as is provided in the GUI.

## BUILT-IN FUNCTIONALITY

Scripts provide a wide array of default behaviors, so that a new fully functioning script can be written with a minimum of required coding.

1. *Loading* Loading and initialization of Scripts is taken care of so they can be effortlessly integrated into other scripts or a GUI without any additional coding beyond the interface shown above.
2. *Data Handling* Every Script has a dictionary *data*. All data stored in this dictionary will be automatically saved and timestamped with a separate file for each key, along with images of any associated plots. This data can be easily reloaded into other python code or Jupyter notebooks using the supplied

*load(path)* function, which takes in a path to the data and will recreate the dictionary.

3. *Logging* Scripts include a *log(message)* function, with any text logged automatically written to file during execution. This can be used to easily have a human readable record of the execution flow, to update the user on the current status, or to assist with debugging.
4. *Timing* The time elapsed and estimated time remaining are automatically calculated for each script.

## SCRIPTITERATORS

Researchers will often run numerous experiments that are only slight variations of each other. For example, one may want to run a set of subscripts in a slightly different order, or loop over one subscript, or repeat an experiment while sweeping one parameter. With the architecture described above, one needs to write a new script to perform each of these minor modifications. This can add significant development time and opens the door to bugs.

Our solution to this problem is *ScriptIterators*, dynamically generated scripts that follow preset templates. By default, users can chain any number of scripts in arbitrary order, create *loops*, where a set of scripts are repeated N times, or create *parameter sweeps*, where the scripts are repeated with one variable changed for each run. *ScriptIterators* can also be nested, allowing multi-dimensional sweeps over multiple variables or loops over sweeps to build up statistics. Toolkits can also define their own types of iterators if other functionality is desired.

Internally, *ScriptIterators* are dynamically defined at runtime using python's *type*

function. Since python is interpreted rather than compiled, new objects can be defined during code execution rather than having to be known at compile time. Each `ScriptIterator` can then be a fully defined class that inherits from `Script`. Thus, they appear identical to manually coded scripts to the rest of the codebase, and no additional overhead is needed to support them.

### C.3.4 GUI

`pylabcontrol` provides a convenient and customizable GUI to use as the default way to run experiments in the lab. The provided GUI has two blank figures, a metadata box, and four tabs: Scripts, Probes, Instruments, and Datasets. The Scripts tab allows Scripts to be imported into the GUI. It then displays the settings, allowing users to input the parameters and run each loaded experiment. When a script is run, the data will be displayed on one or both of plots based on the plotting behavior defined in the script. Plots from different completed scripts can be toggled between by clicking on them in the table. Probes allows real time monitoring of hardware values from instruments. Instruments can be imported and their settings controlled in the instrument tab, or they will be automatically imported into this tab if required for an imported script. After a script is run, the plots and data can be moved to and accessed from the Datasets tab, allowing viewing or saving of previous data. Global information, such as the path that all scripts should use for saved data, is set in the metadata box at the bottom.

Because of the abstraction provided by the `Script` and `Instrument` interfaces, all `Script` and `Instruments` written by users will be compatible with and can be immediately used in the GUI with no additional overhead. However, this configuration of plots and windows may not be ideal for all users. The layout can be easily edited us-

ing QtDesigner, which provides its own intuitive UI, or another similar program to better fit any individual user’s needs.

## C.4 TOOLKITS

Specific Scripts and Instruments written for a given application are contained in Toolkits. There is a strong abstraction boundary between Toolkits and the core code, so the core will not be aware of the contents of individual Toolkits, allowing it to remain fully generic. Unlike the core, which needs to remain highly stable, Toolkits are intended to be constantly expanding and under development as new experiments are proposed and may contain many files under active development at any time. They should be shared between labs, to maximize researcher efficiency and prevent users from rewriting code that already exists elsewhere.

### C.4.1 B26\_TOOLKIT

We provide B26\_toolkit as an example toolkit which provides the necessary instruments and scripts to run quantum optics experiments. The toolkit is split into a series of different modules:

1. *Instruments* Instruments includes implementations of common lab equipment, such as a National Instruments DAQ, Stanford Research System microwave generator, and Spincore pulseblaster.
2. *Scripts* Scripts includes standard experiments and experiment components, such as Galvanometer Scan, ESR, and a set of pulsed AC magnetometry experiments.

3. *ScriptIteratorB26* The core package contains a toolkit-specific `ScriptIterator`. This incorporates Scripts from the toolkit to allow the user to select a series of NVs from a galvanometer scan, optionally center the laser on the NV point spread function, then run a chosen experiment on each. The core code automatically incorporates these specialized `ScriptIterators` as an option in the GUI.
4. *Plotting* Plotting includes a series of 1D and 2D plotting functions, many of which are generic and can be used in newly created Scripts
5. *data\_plotting and data\_analysis* `data_plotting` and `data_analysis` contain a series of data plotting, fitting, and analysis functions to assist in performing a variety of NV experiments.

The toolkit thus provides a fully featured set of tools for the experiments presented in this thesis and that can be used by anyone in the community performing similar experiments.

## C.5 FUTURE WORK

`pylabcontrol` is currently a fully featured platform in use daily in multiple labs. However, there are additional features we would like to add to future versions.

1. *Plot Settings* Currently, the settings used for the GUI's plots are determined at the beginning of the Script's execution, and only `matplotlib`'s limited interactive controls are available. However, a user may want to make changes during the execution as they see the initial data coming in, for example changing a colorbar range or the number of runs averaged. Plot settings would expand the GUI functionality to allow user-configurable settings for each plot that would

remain active during execution, and whose changes would be immediately reflected in the plots.

2. *Configuration Files for Instruments* Currently, the default settings for each instrument are hardcoded in the instrument file. This can cause issues when using version control, as different computers using the same type of instruments will likely want them to have different default values such as connection ports. The default settings will thus be offloaded into external JSON configuration files.
3. *Improved Error Handling* Currently, error handling must be implemented in a bespoke way by the user for each Instrument and Script. We would like to add some basic error handling to the included features, as well as a specification of how this handling should be implemented to the interface.
4. *Feed Forward ScriptIterators* Currently, ScriptIterators can only include Scripts that can function independently. However, there are many occasions where a user may want to take the results of a previous script and use them as a setting for a subsequent one. By adding a feed forward method, so that an arbitrary Script setting can be set to the data value of a previous Script, we drastically expand the set of use cases for these iterators.
5. *Multi-Computer Architecture* Some experiments require coordination between multiple computers, each of which are connected to their own set of devices. While this is not the primary intended mode for pyrabcontrol, it is something that would be useful to support for some use cases. This can be implemented with a RPC interface, where one machine acts as a coordinator and calls func-

tions on the others. This has been prototyped but not yet integrated into the current code, and when doing so would be built around the existing core code-base to make sure that code's complexity is kept to a minimum.

The current state of the project and further improvements can be seen on the project's github page<sup>100</sup>.

# References

- [1] Gershon Kurizki, Patrice Bertet, Yuimaru Kubo, Klaus Mølmer, David Petrosyan, Peter Rabl, and Jörg Schmiedmayer. Quantum technologies with hybrid systems. *Proceedings of the National Academy of Sciences*, 112(13):3847–3848, Mar 2015.
- [2] Donghun Lee, Kenneth W Lee, Jeffrey V Cady, Preeti Ovartchaiyapong, and Ania C Bleszynski Jayich. Topical review: spins and mechanics in diamond. *Journal of Optics*, 19(3):033001, Feb 2017.
- [3] G Binnig, C F Quate, and Ch Gerber. Atomic force microscope. *Physical Review Letters*, 56(9):930, Mar 1986.
- [4] D Rugar, R Budakian, H J Mamin, and B W Chui. Single spin detection by magnetic resonance force microscopy. *Nature*, 430(6997):329–332, Mar 1986.
- [5] Y T Yang, C Callegari, X L Feng, K L Ekinici, and M L Roukes. Zeptogram-scale nanomechanical mass sensing. *Nano Letters*, 6(4):583–586, Mar 2006.
- [6] B Lassagne, D Garcia-Sanchez, A Aguasca, and A Bachtold. Ultrasensitive mass sensing with a nanotube electromechanical resonator. *Nano Letters*, 8(11):3735–3738, Oct 2008.
- [7] Y Martin and H K Wickramasinghe. Magnetic imaging by "force microscopy" with 1000 Å resolution. *Applied Physics Letters*, 50(20):1455, Mar 1987.
- [8] J J Sáenz and N García. Observation of magnetic forces by the atomic force microscope. *Journal of Applied Physics*, 62:4293, Jul 1987.
- [9] J Prat-Camps, C Teo, C C Rusconi, W Wiczorek, and O Romero-Isart. Ultrasensitive inertial and force sensors with diamagnetically levitated magnets. *Physical Review Applied*, 8(3):034002, September 2017.
- [10] Derek F Jackson Kimball, Alexander O Sushkov, and Dmitry Budker. Precessing ferromagnetic needle magnetometer. *Physical Review Letters*, 116(19):190801, May 2016.

- [11] Tao Wang, Sean Lourette, Sean R O’Kelley, Metin Kayci, Y B Band, Derek F Jackson Kimball, Alexander O Sushkov, and Dmitry Budker. Dynamics of a ferromagnetic particle levitated over a superconductor. *Physical Review Applied*, 11(4):044041, April 2019.
- [12] A. Vinante, P. Falferi, G. Gasbarri, A. Setter, C. Timberlake, and H. Ulbricht. Ultralow mechanical damping with meissner-levitated ferromagnetic microparticles. *arXiv:1912.12252*, January 2020.
- [13] S Kolkowitz, A C Bleszynski Jayich, Q P Unterreithmeier, S D Bennett, P Rabl, J G E Harris, and Mikhail D Lukin. Coherent sensing of a mechanical resonator with a single-spin qubit. *Science*, 335(6076):1603–1606, March 2012.
- [14] P Rabl, P Cappellaro, M Dutt, L Jiang, J Maze, and Mikhail D Lukin. Strong magnetic coupling between an electronic spin qubit and a mechanical resonator. *Physical Review B*, 79(4):041302, January 2009.
- [15] P. Rabl. Cooling of mechanical motion with a two-level system: The high-temperature regime. *Physical Review B*, 82(16):165320, October 2010.
- [16] A D Armour, M P Blencowe, and K C Schwab. Entanglement and decoherence of a micromechanical resonator via coupling to a cooper-pair box. *Physical Review Letters*, 88(14):148301, Apr 2002.
- [17] D Vitali, S Gigan, A Ferreira, H R Bohm, P Tombesi, A Guerreiro, V Vedral, A Zeilinger, and M Aspelmeyer. Optomechanical entanglement between a movable mirror and a cavity field. *Physical Review Letters*, 98(3):030405, Jan 2007.
- [18] P W Shor. Polynomial-time algorithms for prime factorization and discrete logarithms on a quantum computer. *SIAM journal on computing*, 26(5):1484–1509, Oct 1997.
- [19] L K Grover. Quantum mechanics helps in searching for a needle in a haystack. *Physical Review Letters*, 79(2):325, Jul 1997.
- [20] Matt Langione, Corban Tillemann-Dick, Amit Kumar, and Vikas Taneja. Where will quantum computers create value—and when? *Boston Consulting Group*, May 2019. <https://www.bcg.com/publications/2019/quantum-computers-create-value-when.aspx>.
- [21] Frank Arute, Kunal Arya, Ryan Babbush, Dave Bacon, Joseph C. Bardin, Rami Barends, Rupak Biswas, Sergio Boixo, Fernando G S L Brandao, David A Buell, Brian Burkett, Yu Chen, Zijun Chen, Ben Chiaro, Roberto Collins, William

- Courtney, Andrew Dunsworth, Edward Farhi, Brooks Foxen, Austin Fowler, Craig Gidney, Marissa Giustina, Rob Graff, Keith Guerin, Steve Habegger, Matthew P. Harrigan, Michael J Hartmann, Alan Ho, Markus Hoffmann, Trent Huang, Travis S. Humble, Sergei V. Isakov, Evan Jeffrey, Zhang Jiang, Dvir Kafri, Kostyantyn Kechedzhi, Julian Kelly, Paul V. Klimov, Sergey Knysh, Alexander Korotkov, Fedor Kostritsa, David Landhuis, Mike Lindmark, Erik Lucero, Dmitry Lyakh, Salvatore Mandrà, Jarrod R. McClean, Matthew McEwen, Anthony Megrant, Xiao Mi, Kristel Michielsen, Masoud Mohseni, Josh Mutus, Ofer Naaman, Matthew Neeley, Charles Neill, Murphy Yuezhen Niu, Eric Ostby, Andre Petukhov, John C. Platt, Chris Quintana, Eleanor G. Rieffel, Pedram Roushan, Nicholas C. Rubin, Daniel Sank, Kevin J Satzinger, Vadim Smelyanskiy, Kevin J Sung, Matthew D Trevithick, Amit Vainsencher, Benjamin Villalonga, Theodore White, Z. Jamie Yao, Ping Yeh, Adam Zalcman, Hartmut Neven, and John M. Martinis. Quantum supremacy using a programmable superconducting processor. *Nature*, 574(7779):505–510, Oct 2019.
- [22] F Dolde, I Jakobi, B Naydenov, N Zhao, S Pezzagna, C Trautmann, J Meijer, P Neumann, F Jelezko, and J Wrachtrup. Room-temperature entanglement between single defect spins in diamond. *Nature*, 9(3):139–143, Feb 2013.
- [23] H Bernien, B Hensen, W Pfaff, G Koolstra, M S Blok, L Robledo, T H Taminiau, M Markham, D J Twitchen, L Childress, and R Hanson. Heralded entanglement between solid-state qubits separated by three metres. *Nature*, 497(7447):86–90, Apr 2013.
- [24] B Hensen, H Bernien, A E Dréau, A Reiserer, N Kalb, M S Blok, J Ruitenberg, R F L Vermeulen, R N Schouten, C Abellán, W Amaya, V Pruneri, M W Mitchell, M Markham, D J Twitchen, D Elkouss, S Wehner, T H Taminiau, and R Hanson. Loophole-free bell inequality violation using electron spins separated by 1.3 kilometres. *Nature*, 526(7575):682–686, October 2015.
- [25] N Kalb, A A Reiserer, P C Humphreys, J J W Bakermans, S J Kamerling, N H Nickerson, S C Benjamin, D J Twitchen, M Markham, and R Hanson. Entanglement distillation between solid-state quantum network nodes. *Science*, 356(6341):928–932, Jun 2017.
- [26] P Rabl, S J Kolkowitz, F H L Koppens, J G E Harris, P Zoller, and Mikhail D Lukin. A quantum spin transducer based on nanoelectromechanical resonator arrays. *Nature Physics*, 6(8):602–608, May 2010.
- [27] C C Rusconi, M J A Schuetz, Jan Gieseler, M D Lukin, and O Romero-Isart. Hybrid architecture for engineering magnonic quantum networks. *Physical Review A*, 100(2):022343, August 2019.

- [28] Marcus W Doherty, Neil B Manson, Paul Delaney, Fedor Jelezko, Jörg Wrachtrup, and Lloyd C L Hollenberg. The nitrogen-vacancy colour centre in diamond. *Physics Reports*, 528(1):1–45, July 2013.
- [29] N Bar-Gill, L M Pham, A Jarmola, D Budker, and R L Walsworth. Solid-state electronic spin coherence time approaching one second. *Nature Communications*, 4:1743–6, April 2013.
- [30] D Farfurnik, A Jarmola, L M Pham, Z H Wang, V V Dobrovitski, R L Walsworth, D Budker, and N Bar-Gill. Optimizing a dynamical decoupling protocol for solid-state electronic spin ensembles in diamond. *Physical Review B*, 92(6):060301, Aug 2015.
- [31] Quirin P Unterreithmeier, Thomas Faust, and Jorg P Kotthaus. Damping of nanomechanical resonators. *Physical Review Letters*, 105(2):027205, July 2010.
- [32] A H Ghadimi, S A Fedorov, N J Engelsen, M J Breyhi, R Schilling, D J Wilson, and Tobias J Kippenberg. Elastic strain engineering for ultralow mechanical dissipation. *Science*, 360(6390):764–768, May 2018.
- [33] M J Donahue and D G Porter. OOMMF user’s guide, version 1.0. *Interagency Report NISTIR 6376*, Sept 1999.
- [34] Martial Defoort, Kunal Lulla, Christophe Blanc, Hossein Ftouni, Olivier Bourgeois, and Eddy Collin. Stressed silicon nitride nanomechanical resonators at helium temperatures. *Journal of Low Temperature Physics*, 171(5-6):731–736, Dec 2013.
- [35] M J A Schuetz, G Giedke, L M K Vandersypen, and J I Cirac. High-fidelity hot gates for generic spin-resonator systems. *Physical Review A*, 95(5):052335–26, May 2017.
- [36] S D Bennett, N Y Yao, J Otterbach, P Zoller, P Rabl, and Mikhail D Lukin. Phonon-induced spin-spin interactions in diamond nanostructures: Application to spin squeezing. *Physical Review Letters*, 110(15):156402, April 2013.
- [37] Michael S J Barson, Phani Peddibhotla, Preeti Ovartchaiyapong, Kumaravelu Ganesan, Richard L Taylor, Matthew Gebert, Zoe Mielens, Berndt Koslowski, David A Simpson, Liam P McGuinness, Jeffrey McCallum, Steven Prawer, Shinobu Onoda, Takeshi Ohshima, Ania C Bleszynski Jayich, Fedor Jelezko, Neil B Manson, , and Marcus W Doherty. Nanomechanical sensing using spins in diamond. *Nano Letters*, 17(3):1496–1503, March 2017.

- [38] J van Wezel and T H Oosterkamp. A nanoscale experiment measuring gravity's role in breaking the unitarity of quantum dynamics. *Proceedings of the Royal Society A: Mathematical, Physical and Engineering Sciences*, 468(2137):35–56, November 2011.
- [39] William Marshall, Christoph Simon, Roger Penrose, and Dik Bouwmeester. Towards quantum superpositions of a mirror. *Physical Review Letters*, 91(13):130401, September 2003.
- [40] O Arcizet, V Jacques, A Siria, P Poncharal, P Vincent, and S Seidelin. A single nitrogen-vacancy defect coupled to a nanomechanical oscillator. *Nature Physics*, 7(11):879–883, September 2011.
- [41] B Pigeau, S Rohr, L Mercier de L eacute pinay, A Gloppe, V Jacques, and O Arcizet. Observation of a phononic mollow triplet in a multimode hybrid spin-nanomechanical system. *Nature Communications*, 6:8603, October 2015.
- [42] Florian Mintert and Christof Wunderlich. Ion-trap quantum logic using long-wavelength radiation. *Nature Communications*, 87(25):257904–5, November 2001.
- [43] Sungkun Hong, Michael S Grinolds, Patrick Maletinsky, Ronald L Walsworth, Mikhail D Lukin, and Amir Yacoby. Coherent, mechanical control of a single electronic spin. *Nano Letters*, 12(8):3920–3924, August 2012.
- [44] Oriol Romero-Isart, Mathieu L Juan, Romain Quidant, and J Ignacio Cirac. Toward quantum superposition of living organisms. *New Journal of Physics*, 12(3):033015, March 2010.
- [45] Darrick E Chang, C A Regal, S B Papp, D J Wilson, J Ye, O Painter, H Jeff Kimble, and P Zoller. Cavity opto-mechanics using an optically levitated nanosphere. *Proceedings of the National Academy of Sciences*, 107(3):1005–1010, January 2010.
- [46] Tongcang Li, Simon Kheifets, and Mark Raizen. Millikelvin cooling of an optically trapped microsphere in vacuum. *Nature Physics*, 7(7):527–530, March 2011.
- [47] Jan Gieseler, B Deutsch, Romain Quidant, and Lukas Novotny. Subkelvin parametric feedback cooling of a laser-trapped nanoparticle. *Physical Review Letters*, 109(10):103603, September 2012.
- [48] Vijay Jain, Jan Gieseler, Clemens Moritz, Christoph Dellago, Romain Quidant, and Lukas Novotny. Direct measurement of photon recoil from a levitated nanoparticle. *Physical Review Letters*, 116(24):243601, June 2016.

- [49] O Romero-Isart, L Clemente, C Navau, A Sanchez, and J I Cirac. Quantum magnetomechanics with levitating superconducting microspheres. *Physical Review Letters*, 109(14):147205, October 2012.
- [50] M Cirio, G K Brennen, and J Twamley. Quantum magnetomechanics: Ultrahigh-q-levitated mechanical oscillators. *Physical Review Letters*, 109(14):147206, October 2012.
- [51] J M Taylor, P Cappellaro, L Childress, L Jiang, D Budker, P R Hemmer, A Yacoby, R Walsworth, and M D Lukin. High-sensitivity diamond magnetometer with nanoscale resolution. *Nature Physics*, 4(10):810–816, September 2008.
- [52] J R Maze, P L Stanwix, J S Hodges, S Hong, J M Taylor, P Cappellaro, L Jiang, M V Gurudev Dutt, E Togan, A S Zibrov, A Yacoby, R L Walsworth, and M D Lukin. Nanoscale magnetic sensing with an individual electronic spin in diamond. *Nature*, 455(7213):644–647, October 2008.
- [53] S Kolkowitz, A Safira, A A High, R C Devlin, S Choi, Q P Unterreithmeier, D Patterson, A S Zibrov, V E Manucharyan, H Park, and M D Lukin. Probing johnson noise and ballistic transport in normal metals with a single-spin qubit. *Science*, 347:1129–1132, March 2015.
- [54] J Druge, C Jean, O Laurent, M-A Méasson, and I Favero. Damping and non-linearity of a levitating magnet in rotation above a superconductor. *New Journal of Physics*, 16:075011, July 2014.
- [55] H Barowski, K M Sattler, and W Schoepe. Static and dynamic forces on a permanent magnet levitating between superconducting surfaces. *Journal of Low Temperature Physics*, 93(1):85–100, October 1993.
- [56] V V Nemoshkalenko, E H Brandt, A A Kordyuk, and B G Nikitin. Dynamics of a permanent magnet levitating above a high-*t<sub>c</sub>* superconductor. *Physica C: Superconductivity*, 170(5-6):481–485, October 1990.
- [57] John R Hull and Ahmet Cansiz. Vertical and lateral forces between a permanent magnet and a high-temperature superconductor. *Journal of Applied Physics*, 86(11):6396–6404, December 1999.
- [58] Levi P Neukirch, Jan Gieseler, Romain Quidant, Lukas Novotny, and A Nick Vamivakas. Observation of nitrogen vacancy photoluminescence from an optically levitated nanodiamond. *Optics letters*, 38(16):2976–2979, January 2013.
- [59] Thai M Hoang, Jonghoon Ahn, Jaehoon Bang, and Tongcang Li. Electron spin control of optically levitated nanodiamonds in vacuum. *Nature Communications*, 7:1–8, July 2016.

- [60] Alexander Kuhlicke, Andreas W Schell, Joachim Zoll, and Oliver Benson. Nitrogen vacancy center fluorescence from a submicron diamond cluster levitated in a linear quadrupole ion trap. *Nature Communications*, 105(7):073101, August 2014.
- [61] T Delord, L Nicolas, L Schwab, and G Hétet. Electron spin resonance from nv centers in diamonds levitating in an ion trap. *New Journal of Physics*, 19(3):033031–11, March 2017.
- [62] I Alda, J Berthelot, R A Rica, and Romain Quidant. Trapping and manipulation of individual nanoparticles in a planar paul trap. *Applied Physics Letters*, 109(16):163105–5, October 2016.
- [63] Jen-Feng Hsu, Peng Ji, Charles W Lewandowski, and Brian D’Urso. Cooling the motion of diamond nanocrystals in a magneto-gravitational trap in high vacuum. *Scientific Reports*, 6:30125, July 2016.
- [64] M C O’Brien, S Dunn, J E Downes, and J Twamley. Magneto-mechanical trapping of micro-diamonds at low pressures. *Applied Physics Letters*, 114(5):053103–6, February 2019.
- [65] Alexander A Korczyk. Magnetic levitation for hard superconductors. *Journal of Applied Physics*, 83(1):610–612, June 1998.
- [66] P Huillery, T Delord, L Nicolas, M Van Den Bossche, M Perdriat, and G. Hetet. Spin-mechanics with levitating ferromagnetic particles. *Physical Review Letters*, 101(13):134415, April 2020.
- [67] R Skomski. Nanomagnetism. *Journal of Physics: Condensed Matter*, 15(20):R841–R896, May 2003.
- [68] R B van Dover, E M Gyorgy, A E White, L F Schneemeyer, R J Felder, and J V Waszczak. Critical currents in proton-irradiated single crystal  $\text{Ba}_2\text{YCu}_3\text{O}_{7-\delta}$ . *Applied Physics Letters*, 56(26):2681, April 1990.
- [69] L Civale, A D Marwick, T K Worthington, M A Kirk, J R Thompson, L Krusin-Elbaum, Y Sun, J R Clem, and F Holtzberg. Vortex confinement by columnar defects in  $\text{YBa}_2\text{Cu}_3\text{O}_7$  crystals: Enhanced pinning at high fields and temperatures. *Physical Review Letters*, 67(5):648, July 1991.
- [70] R A Norte, J P Moura, and S Gröblacher. Mechanical resonators for quantum optomechanics experiments at room temperature. *Physical Review Letters*, 116(14):021001–6, April 2016.

- [71] Christoph Reinhardt, Alexandre Bourassa Tina Müller, and Jack C Sankey. Ultralow-noise sin trampoline resonators for sensing and optomechanics. *Physical Review X*, 6(2):021001–8, April 2016.
- [72] Y Tsaturyan, A Barg, E S Polzik, and A Schliesser. Ultracoherent nanomechanical resonators via soft clamping and dissipation dilution. *Physical Review X*, 12(8):776–783, June 2017.
- [73] Jonilyn G Longenecker, H J Mamin, Alexander W Senko, Lei Chen, Charles T Rettner, Daniel Rugar, and John A Marohn. High-gradient nanomagnets on cantilevers for sensitive detection of nuclear magnetic resonance. *ACS Nano*, 6(11):9637–9645, November 2012.
- [74] R Fischer, D P McNally, C Reetz, G G T Assumpção, T Knief, Y Lin, and C A Regal. Spin detection with a micromechanical trampoline: towards magnetic resonance microscopy harnessing cavity optomechanics. *New Journal of Physics*, 21(4):043049–14, April 2019.
- [75] J-P Tetienne, L Rondin, P Spinicelli, M Chipaux, T Debuisschert, J-F Roch, and V Jacques. Magnetic-field-dependent photodynamics of single nv defects in diamond: an application to qualitative all-optical magnetic imaging. *New Journal of Physics*, 14(10):103033–16, October 2012.
- [76] L Rondin, J-P Tetienne, T Hingant, J-F Roch, P Maletinsky, and V Jacques. Magnetometry with nitrogen-vacancy defects in diamond. *Reports on Progress in Physics*, 77(5):056503, May 2014.
- [77] P Forn-Díaz, L Lamata, E Rico, J Kono, and E Solano. Ultrastrong coupling regimes of light-matter interaction. *Reviews of Modern Physics*, 91(2):025005, June 2019.
- [78] Jan Gieseler, Lukas Novotny, and Romain Quidant. Thermal nonlinearities in a nanomechanical oscillator. *Nature Physics*, 9(12):806–810, November 2013.
- [79] M H Abobeih, J Cramer, M A Bakker, N Kalb, M Markham, D J Twitchen, and T H Taminiau. One-second coherence for a single electron spin coupled to a multi-qubit nuclear-spin environment. *Nature Communications*, 9:2552, June 2018.
- [80] Carlos Gonzalez-Ballester, Jan Gieseler, and Oriol Romero-Isart. Quantum acoustomechanics with a micromagnet. *Physical Review Letters*, 124(9):093602, March 2020.

- [81] D D Bhaktavatsala Rao, S Ali Momenzadeh, and Jörg Wrachtrup. Heralded control of mechanical motion by single spins. *Physical Review Letters*, 117(7):077203–8, August 2016.
- [82] L Thiel, D Rohner, M Ganzhorn, P Appel, E Neu, B Müller, R Kleiner, D Koelle, and P Maletinsky. Quantitative nanoscale vortex imaging using a cryogenic quantum magnetometer. *Nature Nanotechnology*, 11(8):677–681, May 2016.
- [83] Matthew Pelliccione, Alec Jenkins, Preeti Ovartchaiyapong, Christopher Reetz, Eve Emmanouilidou, Ni Ni, and Ania C Bleszynski Jayich. Scanned probe imaging of nanoscale magnetism at cryogenic temperatures with a single-spin quantum sensor. *Nature Nanotechnology*, 11(8):700–705, May 2016.
- [84] Schlüssel Yechezkel, Lenz Till, Rohner Dominik, Bar-Haim Yaniv, Bougas Lykourgos, Kieschnick Michael, Rozenberg Evgeny, Thiel Lucas, Waxman Amir, Maletinsky Patrick, Budker Dmitry, and Folman Ron. Wide-field imaging of superconductor vortices with electron spins in diamond. *Physical Review Applied*, 10(1):1, September 2018.
- [85] C C Rusconi, V Pöchlhacker, K Kustura, J I Cirac, and O Romero-Isart. Quantum spin stabilized magnetic levitation. *Physical Review Letters*, 119(16):167202, October 2017.
- [86] S A Beresnev, V G Chernyak, and G A Fomyagin. Motion of a spherical particle in a rarefied gas. part 2. drag and thermal polarization. *Journal of Fluid Mechanics*, 219(1):405–421, Oct 1990.
- [87] S Kolkowitz, A Safira, A A High, R C Devlin, S Choi, Q P Unterreithmeier, D Patterson, A S Zibrov, V E Manucharyan, H Park, and M D Lukin. Probing johnson noise and ballistic transport in normal metals with a single-spin qubit. *Science*, 347(6226):1129–1132, Mar 2015.
- [88] The Qt Company. Qt. 2020. <https://www.qt.io/>.
- [89] Riverbank Computing Limited. PyQt5. 2020. <https://www.riverbankcomputing.com/software/pyqt/intro>.
- [90] Anaconda software distribution. *Computer Software*, 2020. <https://anaconda.com>.
- [91] Warehouse Project. Python package index (pypi). 2020. <https://pypi.org/>.
- [92] Pauli Virtanen, Ralf Gommers, Travis E. Oliphant, Matt Haberland, Tyler Reddy, David Cournapeau, Evgeni Burovski, Pearu Peterson, Warren

- Weckesser, Jonathan Bright, Stéfan J. van der Walt, Matthew Brett, Joshua Wilson, K. Jarrod Millman, Nikolay Mayorov, Andrew R. J. Nelson, Eric Jones, Robert Kern, Eric Larson, CJ Carey, İlhan Polat, Yu Feng, Eric W. Moore, Jake VanderPlas, Denis Laxalde, Josef Perktold, Robert Cimrman, Ian Henriksen, E. A. Quintero, Charles R Harris, Anne M. Archibald, Antônio H. Ribeiro, Fabian Pedregosa, Paul van Mulbregt, and SciPy 1.0 Contributors. SciPy 1.0: Fundamental Algorithms for Scientific Computing in Python. *Nature Methods*, 17:261–272, 2020.
- [93] Travis E. Oliphant. A guide to numpy. *Trelgol Publishing*, 2006.
- [94] Python Software Foundation. ctypes – a foreign function library for python. 2020. <https://docs.python.org/3/library/ctypes.html>.
- [95] Python for .NET Project. Python for .net. 2020. <http://pythonnet.github.io/>.
- [96] Chris Liechti. pyserial. 2017. <https://pythonhosted.org/pyserial/>.
- [97] labrad - asynchronous client/server rpc system designed for use in scientific laboratories. 2020. <https://github.com/labrad>.
- [98] Jan M. Binder, Alexander Starka, Nikolas Tomeka, Jochen Scheuer, Florian Franka, Kay D. Jahnke, Christoph Müller, Simon Schmitt, Mathias H. Metscha, Thomas Undena, Tobias Gehring, Alexander Huck, Ulrik L. Andersen, Lachlan J. Rogers, and Fedor Jelezko. Qudi: A modular python suite for experiment control and data processing. *SoftwareX*, 6:85–90, Feb 2017.
- [99] pi3diamond. 2016. <https://github.com/HelmutFedder/pi3diamond>.
- [100] Aaron Kabcenell, Jan Gieseler, and Arthur Safira. pylabcontrol – laboratory equipment control for scientific experiments. 2020. <https://github.com/LISE-B26/pylabcontrol>.